Doctoral Dissertation

Effective FE Simulation Methods for Thermal Mechanics of Welding and Post-welding Processes

GUAN XIAOYU

June 2025

Department of Civil Engineering

Division of Global Architecture

Graduate School of Engineering

The University of Osaka

Abstract

To markedly enhance simulation efficiency of welding models, this study systematically investigates numerical methods for single-layer fillet welding and multi-pass butt welding. It then proposes and validates an FEA framework that balances accuracy and computational speed. In the single-layer fillet welding process simulation, a combined experimental and finite-element simulation approach was employed to systematically evaluate the effects of the Continuous Distributed (CD) heat input method and an improved shell–solid elements hybrid strategy on the simulation efficiency. Subsequently, these methods were extended to simulate the three-pass butt-welding process, validating their broad applicability; moreover, by adjusting the heat input model, the efficiency of the CD method during three-pass welding was enhanced, thereby underscoring the critical influence of heat-source selection on computational performance. In addition, to predict the out-of-plane deformation and residual stress of the component of heating correction after welding, a simplified heat input model was developed by analyzing flame thermal–fluid characteristics and partitioning the heat flux distribution area. The optimal heating time and line heating speed were determined, providing guidance for practical process optimization. In summary, the proposed welding simulation framework achieves an optimal balance between predictive accuracy and computational efficiency, offering an effective and scalable numerical platform for large-scale structures and a wide range of welding applications with strong prospects for engineering deployment. Moreover, the simplified heat input model for flame heating correction provides an efficient modeling method for numerical simulation of welding deformation control, promoting more efficient and automated implementation of heating correction procedures.

Table of contents

1. Introduction

1.1 Background and challenges in welding research

1.1.1 Historical development of welding processes

Welding, as a critical manufacturing process for joining metals, has a rich history from ancient craftsmanship to modern high-technology applications. During the Bronze Age (circa 3000 BCE), primitive forge welding emerged as a thermomechanical bonding technique, utilizing localized heating and plastic deformation to achieve metallic coalescence [1.1]. Archaeological investigations of Egyptian pyramid construction reveal systematic implementation of brazing processes, where lead-based filler metals were strategically employed for assembling structural metallic components, indicating early mastery of liquid-phase interfacial metallurgy [1.2]. A pinnacle of medieval metallurgical sophistication was exemplified by Damascus steel fabrication (10th–15th century CE), which harnessed solid-state diffusion bonding to create carbon gradient interfaces through precisely controlled thermal cycling [1.3]. These ancient practices not only addressed practical joining requirements but also conceptually anticipated modern principles of interfacial design, thereby establishing foundational paradigms for contemporary welding metallurgy through their empirical understanding of thermal processing-structure-property interrelationships.

The 19th-century Industrial Revolution brought about enormous changes in manufacturing processes. In the early 19th century, Humphry Davy elucidated the thermodynamic principles of the electric arc [1.4], thereby initiating research into the direct conversion of electrical energy. In 1895, oxy-acetylene welding broke through the limitations of localized heat input control through precise temperature regulation [1.5]; and by 1904, Oscar Kjellberg innovated the metallurgical mechanism of coated welding

electrodes [1.6]. This period laid the theoretical foundation for modern multi-physical-field welding.

In the early 20th century, further innovations propelled the development of gas tungsten arc welding (GTAW) and gas metal arc welding (GMAW). GTAW is renowned for its precise control over heat input, which minimizes oxidation and weld distortion [1.7-1.9]. In GMAW, a shielding gas—commonly CO_2 or an argon-based mixture—protects the molten weld pool from oxidation, while an efficient droplet transfer mechanism enables rapid deposition rates and consistent weld penetration [1.10-1.12]. These process improvements refined the original electric arc welding techniques, enhancing heat input control and weld quality, thereby rendering the technology indispensable for industries such as automotive manufacturing and shipbuilding.

In the early to mid-20th century, the advent of plasma arc welding (PAW) marked a significant advancement in high-energy-density welding techniques. This method harnesses the high temperature and energy density of plasma to achieve precise control over the welding process [1.13,1.14]. During the 1960s, electron beam welding (EBW) emerged, utilizing a high-energy electron beam in a vacuum environment to weld metals with high melting points and thick cross-sections, offering exceptionally high power density [1.15,1.16]. Concurrently, laser beam welding (LBW) employed a focused laser beam as a heat source, characterized by high precision, speed, and minimal deformation [1.17,1.18]. Both EBW and LBW transcended the limitations of traditional heat conduction methods, ushering in a new era of high-energy beam welding. With the interdisciplinary integration of computer technology and materials science, intelligent welding technologies began to rise. In 1985,the technique known as friction stir welding (FSW) was first introduced by the Welding Institute in the UK, enabling low-temperature

solid-state joining of aluminum alloys [1.19,1.20]. Entering the 21st century, robotic welding systems have integrated visual sensing and path planning algorithms, facilitating online monitoring and closed-loop control of multi-physics fields [1.21]. These technological advancements have rendered the welding process more intelligent and precise, meeting the modern manufacturing industry's demand for high-quality welding. Figure 1-1 delineates several commonly employed welding techniques.

1.1.2 Key issues in welding thermal mechanics

Welding processes inherently involve rapid and localized heating followed by steep cooling gradients, which induce significant thermal and mechanical challenges in the fabricated structures. Consequently, the welding process inherently induces structural distortions and the accumulation of residual stresses. Out-of-plane deformations significantly compromise the assembly accuracy, visual appearance, and structural integrity of welded components. These distortions degrade the dimensional precision and structural integrity of the components, potentially leading to misalignment and premature failure under operational loads. Furthermore, corrective measures to rectify such deformations invariably incur additional costs and schedule delays, thereby affecting overall production efficiency [1.22,1.23]. Residual stresses in the weld zone may precipitate brittle cracking, fatigue processes, or corrosion-assisted failure. Moreover, residual stresses within the base metal may compromise the buckling strength of structural components. When these stresses interact with complex geometries, they create stress concentration points that significantly elevate the risk of crack initiation and subsequent propagation under operational loads [1.24,1.25].

(a) Arc welding

(https://highways.dot.gov/public-roads/winter-2021/evaluating-ultrasonic-techniques-detect-bridge-weld-flaws)

(b) Laser welding

(https://www.ilt.fraunhofer.de/en/media-center/brochures/b-laser-beam-welding.html)

(c) Friction stir welding

(https://www.ilt.fraunhofer.de/en/media-center/brochures/b-laser-beam-welding.html)

Figure 1-1 Several commonly employed welding techniques

1.2 Advancements and applications of welding thermal-mechanics simulation

1.2.1 Overview of thermal-mechanics simulation techniques

Since the 1970s, numerical simulation techniques have advanced rapidly, providing a powerful means to address the transient thermal cycles, evolving residual stress distributions, and complex deformation patterns inherent in welding processes. In particular, the finite element method (FEM) enables detailed simulations that accurately predict temperature distributions, stress evolution, and resultant deformations across welded structures [1.26-1.29]. As a result, FEM has become indispensable for optimizing welding parameters and ensuring structural safety.

1.2.2 Effective method for welding simulation

Welding involves a complex interaction of thermal and mechanical processes, during which material properties evolve continuously with temperature. These characteristics render the numerical calculations inherently unstable and more challenging to converge than in purely mechanical problems, resulting in a simulation process that is notably time-consuming [1.30,1.31]. Consequently, reducing modeling and computational time is critical.

To address this issue, extensive investigations have been conducted to enhance the computational efficiency of welding simulations and have developed various methods [1.32-1.39], such as the iterative substructure method, the idealized explicit finite element method, and the hybrid finite element method.

Inherent strain method:

The theory of inherent strain, initially proposed by Ueda [1.32], has been widely utilized

in welding deformation analysis. In this approach, the nodal natural deformations are mapped into their respective inherent strain components. These components are then applied as initial conditions in the vicinity of the welded joint, enabling the use of elastic finite element analysis to estimate the resulting structural deformation. [1.32,1.33]. If the distribution of effective inherent strains is represented by an equation with q parameters $\{\varepsilon^*\}$, the resulting residual elastic strain $\{\varepsilon\}$ at any point of the body produced by the inherent strains are obtained in the following form.

$$\{\varepsilon\} = [\bar{H}^*]\{\varepsilon^*\} \ , \ [\bar{H}^*] = (n \times q) \tag{1.1}$$

Where n is the total number of components of elastic strains. q is the total number of components of inherent strains. In Equation (1.1), the components of the jth row of elastic response matrix $[\bar{H}^*]$ correspond to elastic strains produced in the body when only jth parameter ε^*_j of the inherent strain distribution being unit is imposed.

If m number of elastic strains can be observed, m equations can be taken out of Equation (1.1) and the observation equation is constituted as follows.

$$\{m^\varepsilon\} - [H^*]\{\hat{\varepsilon}^*\} = \{v\}, \ [H^*] = (m \times q) \tag{1.2}$$

Where $\{m^\varepsilon\}$ is the observed strains. $\{v\}$ is the residuals. In the case of rank $[H^*] = q$, the most probable values $\{\hat{\varepsilon}^*\}$ of parameters of the inherent strain are determined by minimizing the residual sum of squares.

$$\{\hat{\varepsilon}^*\} = [A][H^*]^T\{m^\varepsilon\} \equiv [G^*]\{m^\varepsilon\} \tag{1.3}$$

$$[A] \equiv \left(a_{ij}\right) = ([H^*]^T[H^*])^{-1} = (q \times q) \tag{1.4}$$

$$[G^*] \equiv \left(g_{ij}\right) = [A][H^*]^T = (q \times q) \tag{1.5}$$

Where $[A]$ is the variance matrix. $[G^*]$ is the generalized inverse of matrix $[H^*]$.

Then the elastic strain distribution in the whole object can be calculated by substituting Equation (1.3) into Equation (1.1) [1.32].

Iterative substructure method:

The iterative substructure method (ISM) is introduced to overcome the computational inefficiencies of conventional finite element simulations in welding. In welding processes, a highly nonlinear thermo–elastic–plastic region is confined near the heat source, while the remainder of the domain exhibits elastic or weakly nonlinear behavior. Moreover, this nonlinear region moves with the heat source. Traditional FEM requires solving a fully nonlinear problem over the entire domain, resulting in an excessively large computational cost. The iterative substructure method works by dividing the area near the heat source of the welded component into a strongly nonlinear region (B) while the remainder is considered a weakly nonlinear region (A), as illustrated in Figure 1-2. During each iteration, the stiffness of the weakly nonlinear region is kept constant, and an iterative procedure is employed to solve for displacements and reaction forces at the interface between regions. The region (B) is dynamically updated based on criteria such as temperature differences and plastic loading conditions [1.34,1.35].

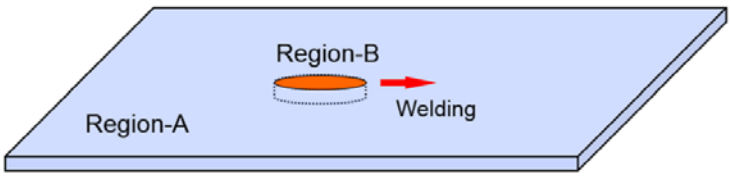

Region	Stiffness	Stress
A	K_A^e No Updating	(A-B)
B	K_B^n Updating every step	B

Figure 1-2 Computation of stiffness and stress in iterative substructure method [1.35]

Idealized explicit finite element method:

The Idealized Explicit Finite Element Method (IEFEM) is a computational technique designed for simulating the transient and nonlinear phenomena in welding processes. While traditional explicit FEM avoids solving simultaneous equations at every time step, it requires very small time increments for stability, making large-scale welding simulations computationally expensive. IEFEM overcomes this by idealizing the complex thermo-mechanical behavior—capturing key effects such as rapid heating, phase transformations, and plastic deformation—thus allowing for larger time steps and fewer iterations. Recent GPU acceleration further enhances its efficiency, enabling effective analysis of extensive multi-pass welded structures [1.36].

Hybrid finite element method

The hybrid finite element method leverages both algorithmic and element-type integration—combining explicit and implicit solvers alongside solid and shell elements. This dual hybrid strategy enables efficient and accurate simulation of welding-induced thermal and mechanical behaviors. Explicit methods handle rapid thermal changes, while implicit schemes ensure stable mechanical computation. Meanwhile, solid-shell element coupling captures local through-thickness effects with reduced computational cost [1.37-1.39].

1.3 **Background of post-welding treatments**

1.3.1 Importance of post-welding treatments

Welding, as a core process in manufacturing, relies on both the welding process and post-weld deformation control and subsequent treatment techniques. Localized high temperatures during welding cause materials to expand, followed by contraction during

cooling, which can result in defects such as angular distortion, and longitudinal or transverse shrinkage of components, as shown in Figure 1-3. If these deformations are not effectively controlled, they directly compromise assembly accuracy, load-bearing capacity, and the service life of the structure. Therefore, post-weld treatment technologies are indispensable elements within the welding process chain [1.40-1.45].

In the early days, post-weld treatment relied predominantly on empirical methods, where manual inspection and operator-driven corrective actions were the norm. As research increasingly revealed the detrimental effects of rapid thermal cycles—such as residual stresses and various forms of distortion, including transverse and longitudinal shrinkage—the need for systematic approaches became apparent [1.46-1.47].

By the mid-20th century, more structured methods emerged. Stress relief heat treatments were developed to reduce residual stresses by reheating the welded structures in a controlled manner [1.48]. Concurrently, mechanical correction techniques, such as hammering and vibratory treatments, were introduced to counteract welding-induced deformations [1.49]. With further technological progress, particularly the integration of modern analytical tools and automated control systems, advanced post-weld treatment strategies were established. Among these, heating correction has become prominent due to their precision, cost-effectiveness, and ease of application [1.50-1.52].

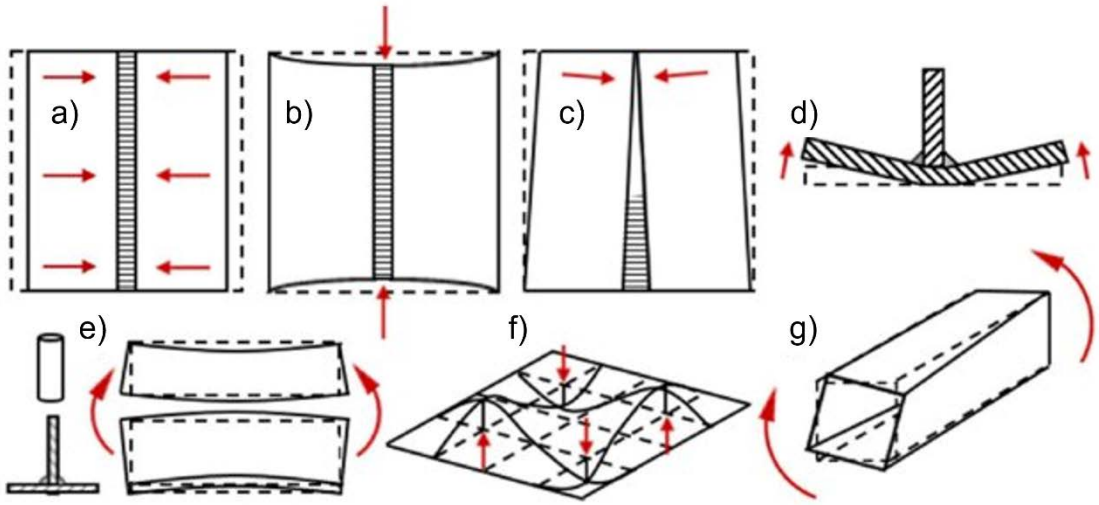

Figure 1-3 Deformation modes: a) transverse shrinkage, b) longitudinal shrinkage, c) rotational distortion, d) angular distortion, e) longitudinal distortion, f) buckling, and g) twisting distortion. [1.42]

Recent advancements in integrating finite element analysis (FEA) with real-time sensor feedback have driven the development of intelligent adaptive post-weld treatment processes. By incorporating temperature, strain, and acoustic sensors into closed-loop control systems and coupling them with FEA models to predict the evolution patterns of residual stresses and deformation trends in welded components, the system dynamically adjusts heat treatment parameters (e.g., localized induction heating and targeted flame rectification) to optimize stress relief efficiency and geometric accuracy. This multisensor-data and model-coordinated approach enables customized treatment strategies based on the thermomechanical state of individual welds, transforming empirically driven post-weld operations into precision-controlled processes. Consequently, it not only enhances structural performance and service life of welded structures but also reduces rework rates and lifecycle maintenance costs through physics-informed parameter optimization [1.53-1.54].

1.3.2 Classification of post-welding treatment processes

Post-welding treatments can be broadly classified into quality assessment, surface finishing, heat treatments, and deformation correction techniques.

Quality assessment: Includes non-destructive testing and inspection to evaluate weld integrity and identify defects [1.55-1.56].

Surface finishing: Involves cleaning, grinding, and coating processes aimed at improving surface quality and preparing the weld for subsequent treatments [1.57].

Heat treatments: Encompasses post-weld heat treatments such as stress relief, tempering, and annealing, which are designed to reduce residual stresses and enhance material properties [1.48].

Deformation correction: Covers both mechanical correction (e.g., hammering, pressing) and thermal correction (e.g., flame heating, induction heating) methods used to rectify distortions and restore dimensional accuracy [1.49-1.54].

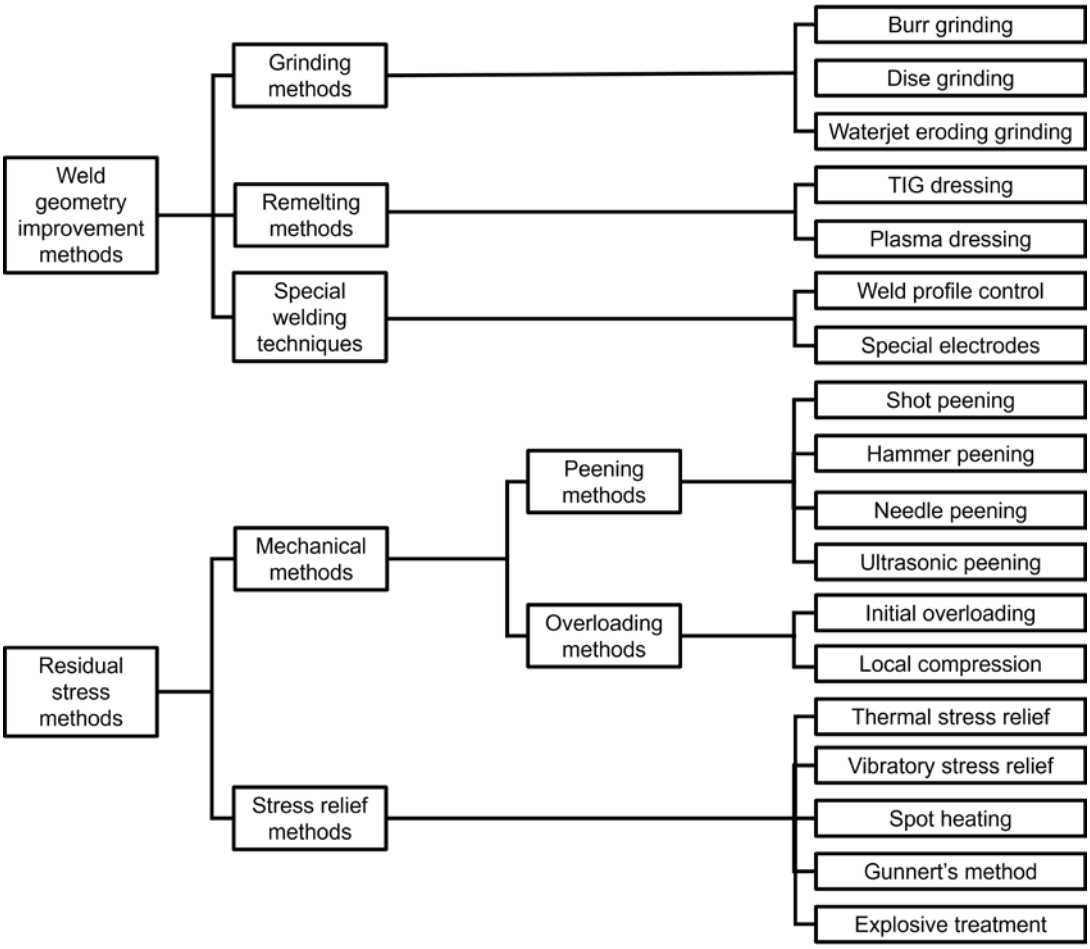

Figure 1-4 Classification of post-weld treatment methods [1.58]

1.3.3 Importance of heating correction

Deformation correction is especially crucial as it directly addresses issues of dimensional inaccuracy and misalignment, which can adversely affect assembly precision and structural reliability. Within the realm of deformation correction, methods are further categorized into mechanical correction and heating correction techniques. Mechanical correction involves the application of controlled external forces to realign distorted components, whereas heating correction employs localized thermal inputs to correct deformations. Heating correction can reduce welding-induced deformation by exploiting the temperature gradient between the upper and lower faces of a steel plate, illustrated in

Figure 1-5. Among the various heating correction methods, flame heating correction offers several distinct advantages over other post-weld correction techniques. First, its flexibility allows for selective and localized application of heat, enabling engineers to precisely target areas exhibiting significant residual stresses or distortions. Second, the method is highly cost-effective, as it typically requires relatively simple equipment compared to more advanced systems such as induction or laser-based methods. Moreover, flame heating is easy to implement on-site, making it an attractive option for industrial environments where rapid corrective actions are essential. Additionally, the precise control of the flame enables consistent and uniform heating, which minimizes the risk of overcorrection and additional thermal distortion. These advantages collectively render flame heating correction a highly practical and efficient solution for restoring dimensional accuracy and structural integrity in welded components [1.50, 1.58].

https://www.safsteelstructure.com/news/flame-correction-method-of-steel-structure/

Figure 1-5 The heating correction process

1.4 **Objective of this study**

Although the welding simulation methods [1.32-1.39] mentioned in Section 1.2 are both effective and efficient, their inherent theoretical complexity often hinders rapid adoption by engineers. This challenge underscores the need to reduce the learning curve and enhance the efficiency of welding simulations in industrial practice. Accordingly, this research aims to develop an approach that is both accessible to engineers and capable of significantly improving simulation efficiency. In addition, for the post-weld phase, a simplified and efficient heating correction simulation model will be proposed. The specific research objectives are as follows:

1) Development of a user-friendly FEM welding simulation method:

For T-shaped welded components, develop an improved finite element welding simulation approach by refining the heat input technique and the method of element coupling. The goal is to create a method that is straightforward for engineers to learn and apply.

2) Evaluation of the method's applicability:

Investigate the suitability of the proposed simulation method by extending its application from single-pass fillet welding to multi-pass butt welding scenarios, thereby demonstrating its versatility and robustness in addressing complex welding processes.

3) Development of a heating correction simulation model:

Analyze the flame heat flow during the post-weld phase and develop a simple yet effective simulation model for heating correction of T-shaped welded components. This model aims to accurately predict post-weld deformations and residual stresses while maintaining ease of use. The simulation results will help identify an optimal heating time, providing practical guidance for improving the efficiency in actual welding correction processes.

By achieving these objectives, the research seeks to bridge the gap between advanced simulation techniques and practical engineering applications, ultimately contributing to improved process control, reduced computational costs, and enhanced structural safety in industrial settings.

1.5 **Contents of the dissertation**

This dissertation consists of five chapters, as shown in Figure 1-6, including an Introduction in Chapter 1 and Conclusions in Chapter 5. In Chapter 2, a series of single-pass fillet welding experiments was conducted. Experimental results served to verify the accuracy of the welding simulation model.This study investigated how various heat input strategies and element configurations—including solid elements and shell-solid hybrids—affect the computational efficiency of welding simulations in T-joint components. In the simulation process, both the Continuous Distributed heat input method (CD method) and the improved shell-solid combination method were employed. Additionally, models developed using the Discontinuous Uniform heat input method (DU method) were compared with those based on the CD method. The results indicate that the use of the CD method combined with shell-solid elements can significantly enhance computational efficiency while maintaining accuracy. In the simulation process of single-pass fillet welding, the use of the shell-solid element combination method resulted in a significant improvement in computational efficiency, whereas the enhancement provided by the Continuous Distributed (CD) method was relatively modest. To further investigate the applicability of the method introduced in Chapter 2 and to refine the CD method for better computational performance, Chapter 3 primarily focuses on simulating the multi-pass butt-welding process. In Chapter 3, a series of three-pass butt-welding experiments

was conducted. The experimental data were used to validate the welding numerical model. In the welding simulations, a shell-solid element combination model was adopted to improve the computational efficiency. In particular, the heat input strategy of the Continuous Distributed (CD) method was modified to improve its combination with the shell-solid formulation. This new model was then rigorously compared with a model that utilized the Discontinuous Uniform (DU) heat input method. The results demonstrated that the revised CD method significantly enhances computational efficiency. This enhancement not only reduces overall computational costs while preserving model accuracy but also yields a model that is accessible and straightforward for engineers to adopt. In Chapter 4, the components produced through welding as discussed in Chapter 2. By analyzing the heat flux distribution associated with the flame during this process, the general pattern was identified, and subsequently, the heat source model for application in numerical simulations was simplified. This approach enables a more precise characterization of the thermal behavior during the correction process, enhancing the reliability of the simulation results. Based on the simulation, the most cost-effective heating condition was determined.

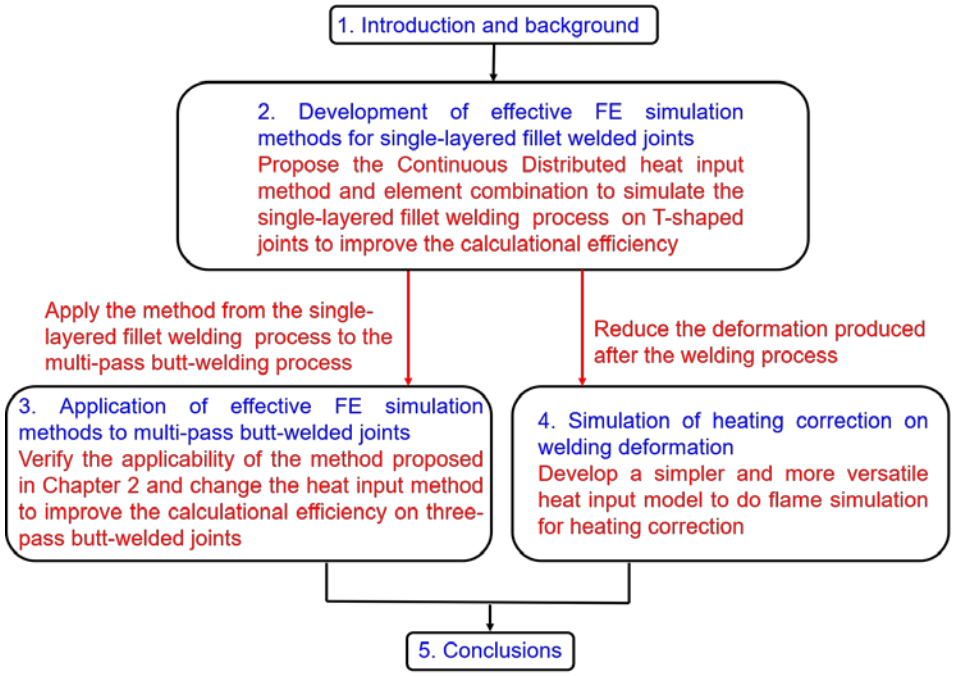

Figure 1-6 Workflow of research chapters and their connections

References

1.1 Lancaster, J. F. (1986). *Welding metallurgy and weldability of metals*. Pergamon Press.

1.2 Scott, D. A. (1991). *Metallography and microstructure of ancient and historic metals*. Getty Conservation Institute.

1.3 Verhoeven, J. D., Pendray, A. H., & Dauksch, W. E. (1998). The key role of impurities in ancient damascus steel blades. *JOM*, *50*(9), 58–64. https://doi.org/10.1007/s11837-998-0409-0.

1.4 Davy, H. (1802). *Elements of Chemical Philosophy*. J. Johnson.

1.5 Fouché, E., & Picard, A. (1903). *Les applications de l'acétylène*. Gauthier-Villars.

1.6 Kjellberg, O. (1907). Electric welding electrode with coating. *Transactions of the ASME*, *29*, 1127-1135.

1.7 Niles, R. W., & Jackson, C. E. (1975). Weld thermal efficiency of the GTAW process. *Welding journal*, *54*(1), 25.

1.8 Thakur, P. P., & Chapgaon, A. N. (2016). A review on effects of GTAW process parameters on weld. *IJRASET*, *4*(1), 136-140.

1.9 Kutelu, B. J., Seidu, S. O., Eghabor, G. I., & Ibitoye, A. I. (2018). Review of GTAW welding parameters. *Journal of Minerals and Materials Characterization and Engineering*, *6*(05), 541.

1.10 Eickhoff, S. T., & Eagar, T. W. (1990). Characterization of spatter in low-current GMAW of titanium alloy plate. *Welding journal*, *69*(10), 382.

1.11 Cho, D. W., Na, S. J., Cho, M. H., & Lee, J. S. (2013). A study on V-groove GMAW for various welding positions. *Journal of Materials Processing Technology*, *213*(9), 1640-1652.

1.12 Mvola, B., & Kah, P. (2017). Effects of shielding gas control: welded joint properties in GMAW process optimization. *The International Journal of Advanced Manufacturing Technology*, 88, 2369-2387.

1.13 Sahoo, A., & Tripathy, S. (2021). Development in plasma arc welding process: a review. *Materials today: proceedings*, *41*, 363-368.

1.14 Wu, C. S., Wang, L., Ren, W. J., & Zhang, X. Y. (2014). Plasma arc welding: Process, sensing, control and modeling. *Journal of manufacturing processes*, *16*(1), 74-85.

1.15 Węglowski, M. S., Błacha, S., & Phillips, A. (2016). *Electron beam welding–Techniques and trends–Review. Vacuum*, *130*, 72-92.

1.16 Siddharth, P. N., & Narayanan, C. S. (2020, December). A review on Electron Beam Welding process. *In Journal of Physics: Conference Series* (Vol. 1706, No. 1, p. 012208). IOP Publishing.

1.17 Auwal, S. T., Ramesh, S., Yusof, F., & Manladan, S. M. (2018). A review on laser beam welding of titanium alloys. *The international Journal of advanced manufacturing technology*, *97*, 1071-1098.

1.18 Xiao, R., & Zhang, X. (2014). Problems and issues in laser beam welding of aluminum–lithium alloys. *Journal of Manufacturing Processes*, *16*(2), 166-175.

1.19 Mishra, R. S., & Ma, D. Z. (2005). *Friction stir welding and processing. Materials science and engineering: R: reports*, *50*(1-2), 1-78.

1.20 Zhang, Y. N., Cao, X., Larose, S., & Wanjara, P. (2012). Review of tools for friction stir welding and processing. *Canadian Metallurgical Quarterly*, *51*(3), 250-261.

1.21 Rout, A., Deepak, B. B. V. L., & Biswal, B. B. (2019). Advances in weld seam tracking techniques for robotic welding: A review. *robotics and computer-integrated manufacturing*, *56*, 12-37.

1.22 Deng, D., Liang, W., & Murakawa, H. (2007). Determination of welding deformation in fillet-welded joint by means of numerical simulation and comparison with experimental measurements. *Journal of Materials Processing Technology*, *183*(2-3), 219-225.

1.23 Chen, Z., Chen, Z., & Shenoi, R. A. (2015). Influence of welding sequence on welding deformation and residual stress of a stiffened plate structure. *Ocean Engineering*, *106*, 271-280. Chen, Z., Chen, Z., & Shenoi, R. A. (2015).

Influence of welding sequence on welding deformation and residual stress of a stiffened plate structure. *Ocean Engineering*, *106*, 271-280.

1.24 Teng, T. L., Chang, P. H., & Tseng, W. C. (2003). Effect of welding sequences on residual stresses. *Computers & structures*, *81*(5), 273-286.

1.25 Jin, D., Hou, C., & Shen, L. (2021). Effect of welding residual stress on the performance of CFST tubular joints. *Journal of Constructional Steel Research*, *184*, 106827.

1.26 Ueda, Y., & Yamakawa, T. (1971). Analysis of thermal elastic-plastic stress and strain during welding by finite element method. *Japan Welding Society Transactions*, *2*(2).

1.27 Wikander, L., Karlsson, L., Nasstrom, M., & Webster, P. (1994). Finite element simulation and measurement of welding residual stresses. *Modelling and Simulation in Materials Science and Engineering*, *2*(4), 845.

1.28 Takechi, S., Aoyama, K., & Nomoto, T. (1998). Basic studies on accuracy management systems based on estimating welding deformations. *Journal of marine science and technology*, *3*, 194-200.

1.29 Deng, D., Murakawa, H., & Liang, W. (2007). Numerical simulation of welding distortion in large structures. *Computer methods in applied mechanics and engineering*, *196*(45-48), 4613-4627.

1.30 Romanin, L., Ferro, P., & Berto, F. (2021). A simplified non-linear numerical method for the assessment of welding induced deformations. *Marine Structures*, *78*, 102982.

1.31 Farias, R. M., Teixeira, P. R. F., & Vilarinho, L. O. (2021). An efficient computational approach for heat source optimization in numerical simulations

of arc welding processes. *Journal of Constructional Steel Research*, *176*, 106382.

1.32 Ueda, Y., Fukuda, K., & Tanigawa, M. (1979). New measuring method of 3-dimensional residual stresses based on theory of inherent strain. *Journal of the Society of Naval Architects of Japan*, *1979*(145), 203-211.

1.33 Murakawa, H., Deng, D., Ma, N., & Wang, J. (2012). Applications of inherent strain and interface element to simulation of welding deformation in thin plate structures. *Computational Materials Science*, *51*(1), 43-52.

1.34 Nishikawa, H., Serizawa, H., & Murakawa, H. (2007). Actual application of FEM to analysis of large scale mechanical problems in welding. *Science and Technology of Welding and Joining*, *12*(2), 147-152.

1.35 Murakawa, H., Ma, N., & Huang, H. (2015). Iterative substructure method employing concept of inherent strain for large-scale welding problems. *Welding in the World*, *59*, 53-63.

1.36 Ikushima, K., & Shibahara, M. (2014). Prediction of residual stresses in multi-pass welded joint using idealized explicit FEM accelerated by a GPU. *Computational materials science*, *93*, 62-67.

1.37 Liu, Y., Wang, P., Fang, H., & Ma, N. (2021). Characteristics of welding distortion and residual stresses in thin-walled pipes by solid-shell hybrid modelling and experimental verification. *Journal of Manufacturing Processes*, *69*, 532-544.

1.38 Ma, N. (2016). An accelerated explicit method with GPU parallel computing for thermal stress and welding deformation of large structure models. *The International Journal of Advanced Manufacturing Technology*, *87*, 2195-2211.

1.39 Feng, Z., Ma, N., Li, W., Narasaki, K., & Lu, F. (2020). Efficient analysis of welding thermal conduction using the Newton–Raphson method, implicit method, and their combination. *The International Journal of Advanced Manufacturing Technology*, *111*, 1929-1940.

1.40 Adamczuk, P. C., Machado, I. G., & Mazzaferro, J. A. E. (2017). Methodology for predicting the angular distortion in multi-pass butt-joint welding. *Journal of Materials Processing Technology*, *240*, 305-313.

1.41 Zhu, J., Khurshid, M., & Barsoum, Z. (2019). Accuracy of computational welding mechanics methods for estimation of angular distortion and residual stresses. *Welding in the World*, *63*, 1391-1405.

1.42 Kollár, D. (2020). *Welding Simulation in Advanced Manufacturing and Design of Steel Structures* (Doctoral dissertation, Budapest University of Technology and Economics (Hungary)).

1.43 Murakawa, H., Sano, M., & Wang, J. (2012). Influence of root gap and tack weld on transverse shrinkage during welding. *Trans. JWRI*, *41*(1), 65-70.

1.44 Urbański, T., & Taczała, M. (2020). Prediction of a transverse shrinkage of butt welded joints in shipyard conditions using the design of experimental approach. *International Journal of Naval Architecture and Ocean Engineering*, *12*, 784-798.

1.45 Rathod, C. H. A. N. D. A. R., & Reddy, G. K. (2016). Experimental investigation of angular distortion and transverse shrinkage in CO2 arc welding process. *International Journal of Mechanical Engineering*, *5*(4), 21.

1.46 De, A., & DebRoy, T. (2011). A perspective on residual stresses in welding. *Science and Technology of Welding and Joining*, *16*(3), 204-208.

1.47 Dong, P. (2005). Residual stresses and distortions in welded structures: a perspective for engineering applications. *Science and Technology of Welding and Joining*, *10*(4), 389-398.

1.48 Raghunathan, V. S., Seetharaman, V., Venkadesan, S., & Rodriguez, P. (1979). The influence of post weld heat treatments on the structure, composition and the amount of ferrite in type 316 stainless steel welds. *Metallurgical Transactions A*, *10*, 1683-1689.

1.49 Lefebvre, F., Revilla-Gomez, C., Buffière, J. Y., Verdu, C., & Peyrac, C. (2014). Understanding the mechanisms responsible for the beneficial effect of hammer peening in welded structure under fatigue loading. *Advanced Materials Research*, *996*, 761-768.

1.50 Seong, W. J., & Na, S. J. (2022). Systematization of heat straightening process of stiffened plate by surface flattening. *Journal of Materials Processing Technology*, *299*, 117333.

1.51 Cho, H., Park, J. S., Han, Y. S., Xu, G., & Sohn, D. (2024). Electromagnetic–thermal–mechanical coupling analysis of bent rotor straightening via electromagnetic induction heating. *Journal of Computational Design and Engineering*, *11*(6), 283-299.

1.52 Kowalkowski, K., & Varma, A. H. (2007). Effects of multiple damage-heat straightening repairs on steel beams. *Transportation research record*, *2028*(1), 67-77.

1.53 Wang, B., Hu, S. J., Sun, L., & Freiheit, T. (2020). Intelligent welding system technologies: State-of-the-art review and perspectives. *Journal of Manufacturing Systems*, *56*, 373-391.

1.54 Foronda, E., Ramírez, N., Arboleda, J. A., Toro, A., & Giraldo-Barrada, J. E. (2023). Finite element analysis of the localized post-weld heat treatment of a Pelton runner. *Materials Today Communications*, *36*, 106795.

1.55 Gupta, M., Khan, M. A., Butola, R., & Singari, R. M. (2022). Advances in applications of Non-Destructive Testing (NDT): A review. *Advances in Materials and Processing Technologies*, *8*(2), 2286-2307.

1.56 Lihavainen, V. M., Marquis, G., & Statnikov, E. S. (2004). Fatigue strength of a longitudinal attachment improved by ultrasonic impact treatment. *Welding in the World*, *48*, 67-73.

1.57 Braun, M., & Wang, X. (2021). A review of fatigue test data on weld toe grinding and weld profiling. *International journal of fatigue*, *145*, 106073.

1.58 Lacalle, R., Álvarez, J. A., Ferreño, D., Portilla, J., Ruiz, E., Arroyo, B., & Gutiérrez-Solana, F. (2013). Influence of the flame straightening process on microstructural, mechanical and fracture properties of S235 JR, S460 ML and S690 QL structural steels. *Experimental Mechanics*, *53*, 893-909.

2. Development of effective FE simulation methods for single-layered fillet welded joints

2.1 Introduction

In structural engineering, T-joint fillet welds are among the most commonly used connection types, particularly in sectors such as construction, bridges, shipbuilding, and offshore platforms. These joints connect two components at a 90-degree angle, forming a "T" shape, and are primarily joined using fillet welds. The simplicity in design and reduced preparation requirements make fillet welds a cost-effective choice in engineering applications [2.1-2.4].

In this chapter, T-joint components are selected as the research focus. Initially, single-layered welding experiments are conducted on these components. Subsequently, conventional numerical simulation methods are employed to model the welding process. Building upon this, an improved continuous heat input method and an element combination simulation approach are proposed. These novel methods are compared with traditional simulations to evaluate their effectiveness in enhancing computational efficiency.

2.2 Experiment

2.2.1 Specimen

To validate the welding process simulation accuracy in this chapter, a systematic verification was conducted through a comparative evaluation of experimental and numerical results. The experimental protocol is detailed as follows:

The T-joint specimens were fabricated using a double-pass single-layered fillet welding

process. Gas metal arc welding (GMAW) was employed to execute the welding operations. As illustrated in Figure 2-1, the assembly consists of a 250 mm square base plate with an 80 mm-high rib plate welded at its mid-span. Specimens with two thickness specifications (9 mm and 12 mm) were prepared, totaling four test units (two per thickness grade). The base material was SM400A general structural steel compliant with JIS G3106 standard, paired with YGW11 welding wire. Key mechanical properties encompassing yield strength, tensile strength, and elongation are tabulated in Table 2-1.

Table 2-1
Mechanical properties of materials for T-shaped fillet welded specimens

Material	Thickness (mm)	Yield strength (N/mm^2)	Tensile strength (N/mm^2)	Elongation (%)
SM400A	9	355	463	30
	12	353	471	28
YGW11	1.2 (diameter)	390	490-670	18

2.2.2 Experimental procedure

Prior to formal welding, the rib plate was preliminarily fixed to the base plate through tack welding at both weld line extremities. Stress relief annealing was performed in an electric furnace at 630 °C for approximately four hours to eliminate initial plate stresses and tack welding-induced residual stresses before fillet welding. As detailed in Table 2-2, the welding parameters were configured as follows: For 9 mm-thick specimens, 250 A current and 25 V voltage were applied with travel speeds of 6.6 mm/s (Pass 1) and 6.4 mm/s (Pass 2). The 12 mm-thick specimens required adjusted parameters of 260 A current and 26 V voltage, corresponding to 5.1 mm/s and 5 mm/s welding speeds, respectively.

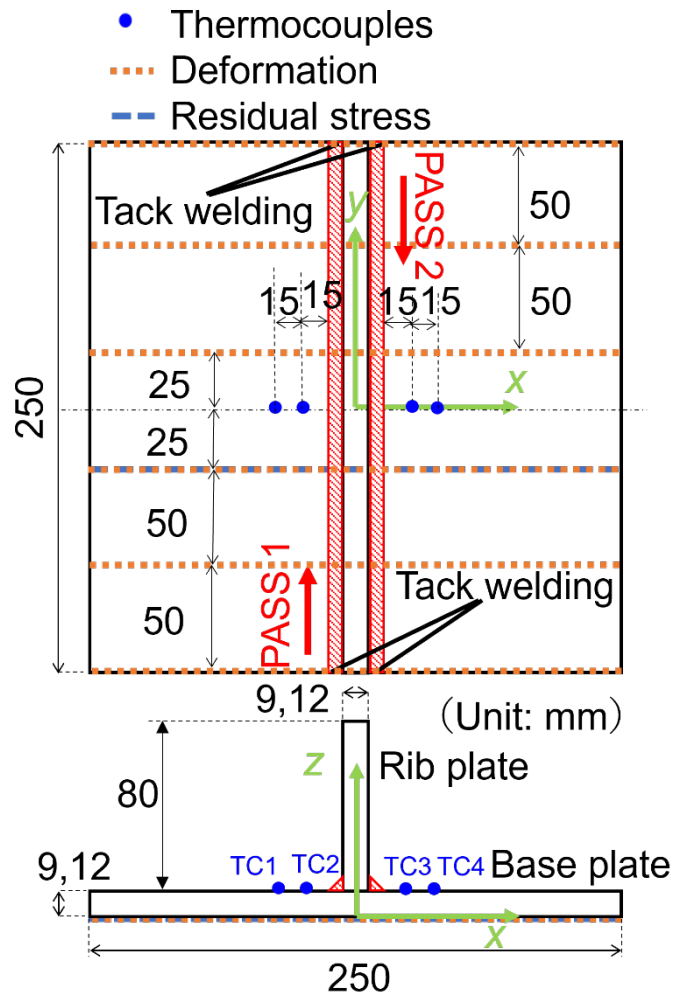

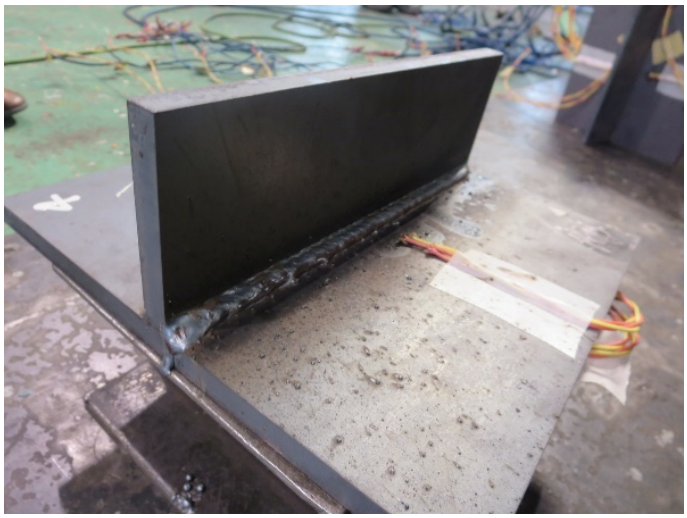

Figure 2-1 Geometry and dimensions of the T-joint fillet welded specimens

Temperature monitoring involved four thermocouples mounted on the base plate's upper surface (locations shown in Figure 2-1). Thermocouples were strategically positioned in a transverse gradient configuration relative to weld passes: TC1 and TC2 were placed at 30 mm and 15 mm normal distances from PASS 1 centerline, respectively, while TC3 and TC4 mirrored this arrangement at 15 mm and 30 mm offsets from PASS 2 centerline. Out-of-plane deformation measurement adopted a full-field grid protocol: Six cross-sections at y=±25, ±75, ±125 mm along the welding transverse direction (x-axis) were established (see orange markers in Figure 2-1). A 50 mm×50 mm grid pattern containing 36 nodal points was systematically measured using a dial indicator. Deformation values were quantified by calculating differential readings between pre- and post-welding states, with edge points serving as zero-reference baselines. Physical obstruction from the rib plate necessitated displacement data acquisition on the base plate's lower surface for continuous measurement continuity.

Residual stress characterization employed X-ray diffraction (Pulstec Industrial μ-X360s) at the base plate's lower surface midspan (y=-25 mm), aligned with the blue reference line in Figure 2-1. Biaxial stress components (welding and transverse directions) were quantitatively evaluated.

Table 2-2
Welding conditions for T-shaped fillet specimens

Thickness of Base/rib plate (mm)	Pass	Voltage (V)	Current (A)	Speed (mm/s)
9/9	1	25	250	6.6
	2			6.4
12/12	1	26	260	5.1
	2			5

2.3 Welding simulation by Continuous Distributed heat input method

2.3.1 The simulation model

The welding of T-joint fillet specimens was simulated using the finite element method (FEM) in ABAQUS. As illustrated in Figure 2-2, the temperature-dependent thermomechanical properties and physical constants of the materials were incorporated, with data sourced from references [2.5, 2.6]. It is noteworthy that the stress-strain curves presented in Figure 2-2b), c), and d) represent true stress and true strain values converted through post-processing. The boundary conditions were implemented as follows:

Thermal boundary: Heat transfer through convective heat exchange between model surfaces and ambient air.

Mechanical constraints: Mechanical constraints were implemented as annotated in Figure 2-3: The lower-left corner node received triaxial displacement constraints ($U_x=U_y=U_z=0$), the lower-right corner node had *y*/*z*-direction degrees of freedom restrictions ($U_y=U_z=0$), and the upper-left corner node was subjected to *z*-direction displacement fixation ($U_z=0$). The constraints achieved effective rigid-body displacement control without over-constraint while maintaining solution uniqueness.

Figure 2-3 displays the schematic configuration of the simulation model, where white zones depict deposited weld metal and green areas represent base/rib plates. Two distinct models were established based on specimen thickness:

9 mm-thick model containing 3,528 nodes.

12 mm-thick model with increased nodal density of 5,586 nodes.

Welding thermal input sequences were strictly synchronized with experimental chronographs.

Critical geometric modeling specifications include:

(1) Parametric weld leg dimensions:

9 mm specimens: 5 mm leg lengths in both rib and base plate orientations.

12 mm specimens: 5 mm leg length in rib orientation with extended 6.5 mm length in base plate direction.

(2) Assembly clearance simulation: Microscopic gaps observed between rib and base plates during actual welding were replicated by introducing a 0.1 mm process gap in the model (see annotated region in Figure 2-3).

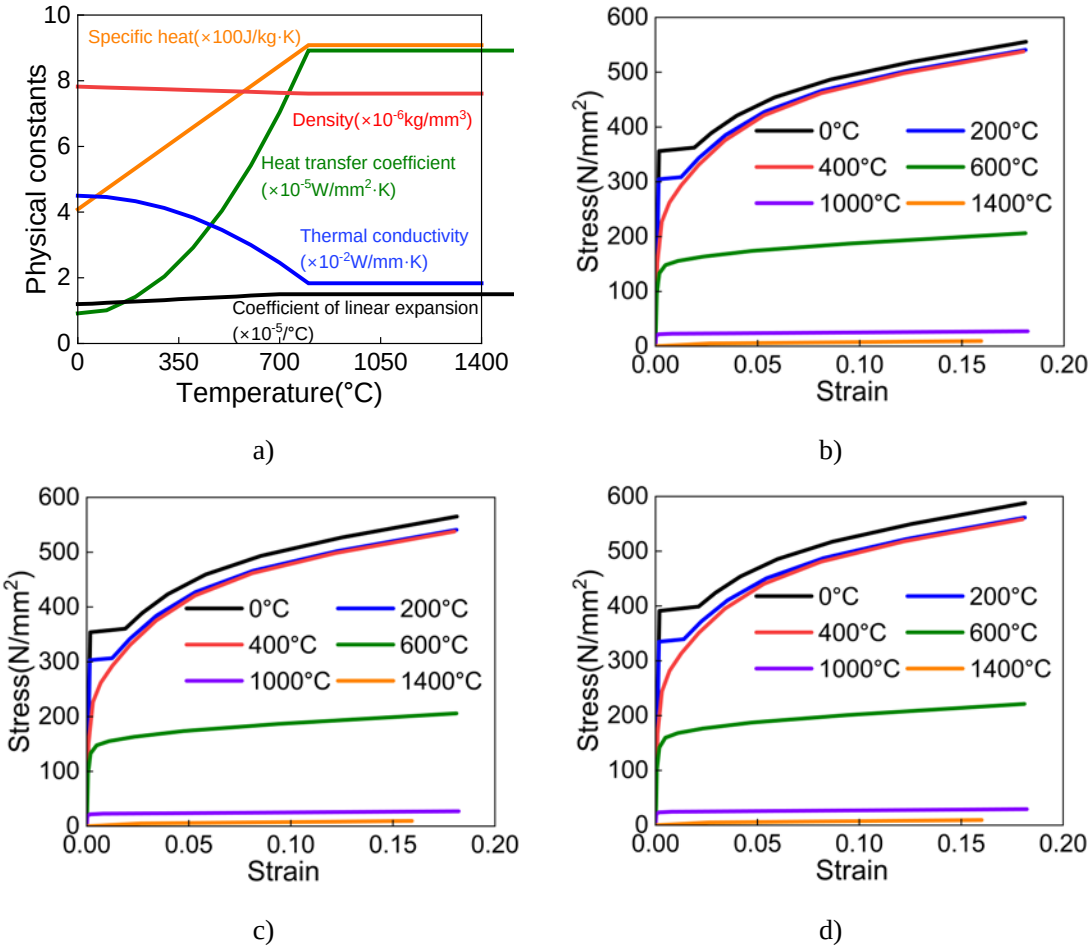

Figure 2-2 a) Temperature-dependent physical constants and stress-strain relationships of b) 9 mm-thick base metal c) 12 mm-thick base metal and d) weld metal

In thermal simulations, no fluid flow occurs during solidification and that heat conduction follows Fourier's law, the heat flux is linearly dependent on the temperature gradient [2.7, 2.8]—the heat transfer in any subdomain Ω_i adheres to the classical energy conservation law, as expressed in Equation (2.1):

$$\rho \frac{\partial \mathcal{H}}{\partial t} - \nabla \cdot (\kappa \nabla T) = q \quad \forall (\boldsymbol{x}, t) \in \Omega_i \tag{2.1}$$

Where:

- $\mathcal{H}$ represents the enthalpy per unit volume,
- T represents the temperature,
- $\kappa = \kappa(T)$ represents the temperature-dependent (isotropic) thermal conductivity
- $q = q(\boldsymbol{x}, t)$ represents the volume heat input from the welding process.

Initial thermal conditions are defined as:

$$T = T_0 \quad \forall \boldsymbol{x} \in \Omega_i, t = t_0 \tag{2.2}$$

At the boundary $\partial\Omega$, the conditions are expressed in Equations (2.3-2.5):

$$T = \bar{T} \quad at\ \partial\Omega_T \tag{2.3}$$

$$-\kappa \nabla T \cdot \boldsymbol{n} = \bar{q} \quad at\ \partial\Omega_q \tag{2.4}$$

$$-\kappa \nabla T \cdot \boldsymbol{n} = h_{env}(T - T_{env}) \quad at\ \partial\Omega_c \tag{2.5}$$

Where:

- $\partial\Omega_T$ represents the mutually exclusive region of the boundary $\partial\Omega$ with prescribed temperature,
- $\partial\Omega_q$ represents the mutually exclusive region of the boundary $\partial\Omega$ with conductive heat flux,
- $\partial\Omega_c$ represents the mutually exclusive region of the boundary $\partial\Omega$ with

convective heat flux,

- $\bar{T}$ represents imposed temperature,
- $\bar{q}$ represents heat flux fields,
- T_{env} represents ambient temperature,
- h_{env} represents heat transfer coefficient,
- $\boldsymbol{n}$ represents the outward unit normal vector on the boundary.

During the welding process, apart from elastic, plastic, and thermal strains, solid-state phase changes may also contribute to the strain field via transformation-induced effects. These include volumetric transformation strain and transformation plasticity. However, for mild steels, these effects can be neglected without significant loss of accuracy in residual stress predictions [2.7]. Thus, the strain rate $\dot{\varepsilon}$ is typically expressed in Equation (2.6):

$$\dot{\varepsilon} = \dot{\varepsilon}^e + \dot{\varepsilon}^p + \dot{\varepsilon}^{th} \tag{2.6}$$

Where superscripts e, p, and th represent elastic, plastic, and thermal components, respectively.

The elastic stress response is usually captured through a hypoelastic formulation. In particular, the objective stress rate $\hat{\sigma}_{GN}$ (the Green–Naghdi rate) is given in Equation (2.7):

$$\hat{\sigma}_{GN} = E^e \dot{\varepsilon}^e + \frac{dE^e}{dT} \dot{T} \varepsilon^e \tag{2.7}$$

Where:

- E^e represents the elastic stiffness matrix,
- $\dot{T}$ represents the rate of temperature change.

To quantify residual stresses and welding-induced deformations, the mechanical equilibrium must be satisfied [2.8]. The momentum balance equation in the spatial domain Ω takes the form:

$$\nabla \cdot \boldsymbol{\sigma} + \rho \boldsymbol{b} = 0 \quad in\ \Omega \tag{2.8}$$

with the following boundary conditions:

$$\boldsymbol{u} = \bar{\boldsymbol{u}} \quad at\ \partial\Omega_u \tag{2.9}$$

$$\boldsymbol{\sigma} \cdot \boldsymbol{n} = \bar{\boldsymbol{t}} \quad at\ \partial\Omega_t \tag{2.10}$$

In the context of solid mechanics under quasi-static conditions, the mixed formulation in terms of displacement $\boldsymbol{u}$ and mean stress p seeks solutions that fulfill the following variational equations over the domain Ω:

$$\int_\Omega \boldsymbol{s}\ \text{grad}\ \boldsymbol{w}\ dV + \int_\Omega p\ \text{div}\ \boldsymbol{w}\ dV = \int_\Omega \boldsymbol{\rho b} \cdot \boldsymbol{w}\ dV + \int_{\partial\Omega_t} \bar{\boldsymbol{t}} \cdot \boldsymbol{w}\ dS \tag{2.11}$$

$$\int_\Omega \left[tr\ (\varepsilon_M) - \frac{p}{\kappa}\right] q\ dV = 0 \tag{2.12}$$

Equation (2.11) is the weak form of the momentum balance equations. where:

- $\boldsymbol{w}$ represents arbitrary admissible test functions corresponding to the displacement,
- q represents arbitrary admissible test functions corresponding to the mean-stress fields,
- $\boldsymbol{s}$ represents the internal stress tensor,
- $\rho \boldsymbol{b}$ represents the body force,
- $\bar{\boldsymbol{t}}$ represents the external traction applied on the boundary $\partial\Omega_t$.

The finite element discretization introduces trial functions for the unknown fields. The displacement field $\boldsymbol{u}$ is approximated as:

$$\boldsymbol{u} = \sum_{i=1}^{n_u} N_i \, \boldsymbol{U}_i = \boldsymbol{N}\boldsymbol{U} \tag{2.13}$$

Similarly, the mean stress field p is interpolated as:

$$p = \sum_{j=1}^{n_p} N_{pj} \, P_j = \boldsymbol{N}_p \boldsymbol{P} \tag{2.14}$$

In these expressions, N_i and N_{pj} are the shape functions associated with the displacement and mean-stress degrees of freedom, respectively, while $\boldsymbol{U}_i$ and P_j represent the corresponding nodal values.

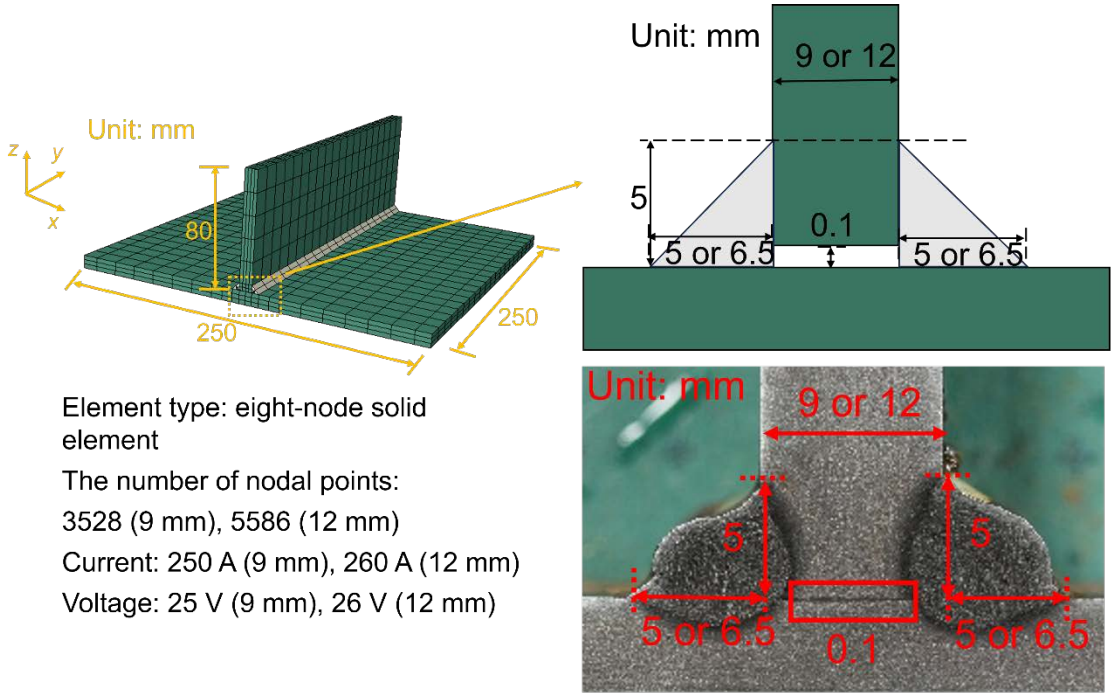

Figure 2-3 The simulation model using solid elements

2.3.2 Heat input methods

2.3.2.1 Discontinuous Uniform heat input method

This chapter conducted comparative analysis of two thermal input models for welding process optimization. The Discontinuous Uniform (DU) method discretized the welding

process into 42 computational steps (40 heating + 2 cooling phases), segmenting weld beads into 20 sections along the welding path. A sequential loading protocol was implemented: The Initial bead section underwent a 20-step incremental heating followed by a single cooling step, with the second section repeating identical thermal cycles before final global cooling. Heat application to triangular weld bead elements followed governing Equations (2.15) and (2.16), incorporating thermal efficiency coefficient η to account for equipment-to-workpiece energy loss (arc welding η =0.47-0.85 [2.9]). Optimal η values were determined through inverse analysis, iteratively matching simulated temperature histories with experimental measurements at sub-5% error tolerance.

$$Q = \eta \frac{EI}{v} \tag{2.15}$$

$$q_m = \frac{Q}{A}\frac{v}{L} \tag{2.16}$$

Where:

- Q represents the amount of heat introduced by welding per unit length (J/mm),
- E represents the welding voltage (V),
- I represents the welding current (A),
- η represents the thermal efficiency of the process,
- v represents the welding speed (mm/s),
- A represents the cross-sectional size of the heat input zone (mm^2),
- L represents the length of the heat input zone (mm),
- q_m represents the welding energy supplied per unit time and unit volume ($J/s/mm^3$).

2.3.2.2 Continuous Distributed heat input method

In order to reduce modeling complexity and improve simulation performance, this study introduces a new heat input approach, referred to as the Continuous Distributed (CD) method. By developing ABAQUS user subroutines to simulate moving heat sources based on Friedman's Gaussian distribution formula [2.10], the CD method replaces the uniform heat input approach used in prior models. The implementation protocol consolidates the process into four computational steps (2 heating + 2 cooling): First, continuous heating of the initial weld bead is completed in a single step through subroutine-controlled heat source movement, then comes a dedicated cooling step; afterward, the second bead is heated in one step implemented by the same subroutine, concluding with global model cooling. This approach reduces the 42-step procedure (40 heating + 2 cooling phases) of traditional DU methods to merely 4 steps, significantly decreasing modeling complexity while maintaining the Gaussian heat flux distribution (see Equation (2.17)). The subroutine dynamically calculates spatial thermal gradients, ensuring thermomechanical consistency between moving heat source behavior and physical processes.

The T-joint configuration employed the heat input expression provided in Equation (2.17).

$$q(r) = \frac{3\eta EI}{\pi R^2} e^{-\frac{3r^2}{R^2}} \tag{2.17}$$

Where:

- $q(r)$ represents the distribution of heat energy in the weld (J/s/mm^2),
- E represents the welding voltage (V),
- I represents the welding current (A),
- η represents the thermal efficiency of the process,
- R represents the radius over which heat is effectively delivered (mm),
- r represents the radial distance from the heat source center (mm).

Figure 2-4 illustrates the fundamental divergence in heat flux distributions between the DU and CD methods. The DU method employs discrete segmented loading, dividing weld beads into 20 equidistant sections along the welding direction, with uniform thermal flux applied per section during discrete computational steps. In contrast, the CD method implements a moving Gaussian heat source model governed by Equation (2.17), where thermal flux follows spatial gradient distribution. Numerically, the DU method requires 42 explicit steps (40 heating + 2 cooling) with manual inter-step thermal zone definitions, whereas the CD method reduces total steps to 4 (2 heating + 2 cooling) through automated coupling of heat source velocity field and time increments, simultaneously eliminating numerical oscillations induced by artificial segmentation.

The continuous heat source trajectory in the CD method enables precise characterization of molten pool dynamics, as evidenced by Figure 2-5. Figure 2-5 compares the experimental and numerical simulation results of the molten pool when the specimen thickness is 9 mm. The comparison results indicate that the simulated molten pool contour is basically consistent with the morphology of the experimental results, which verifies the reliability of the CD method in predicting the transient molten pool behavior in the established model.

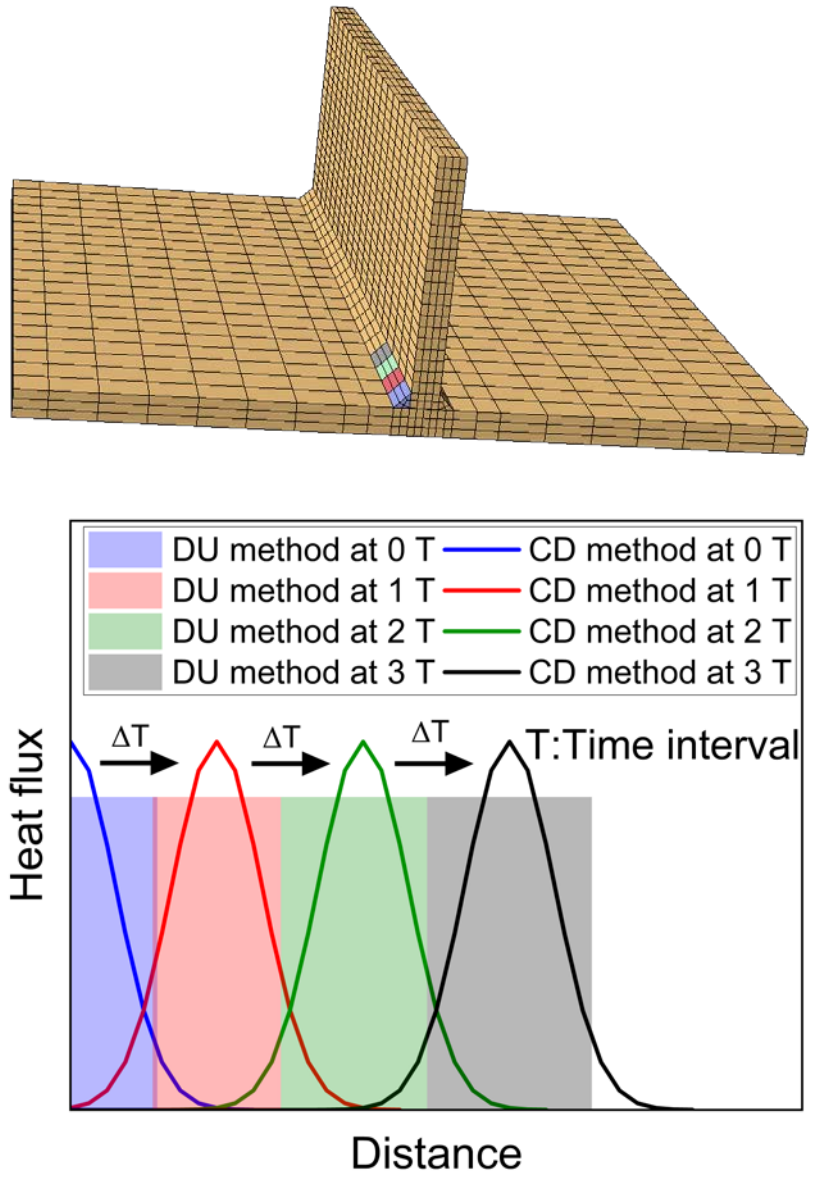

Figure 2-4 Distributions of heat flux by the DU and CD method

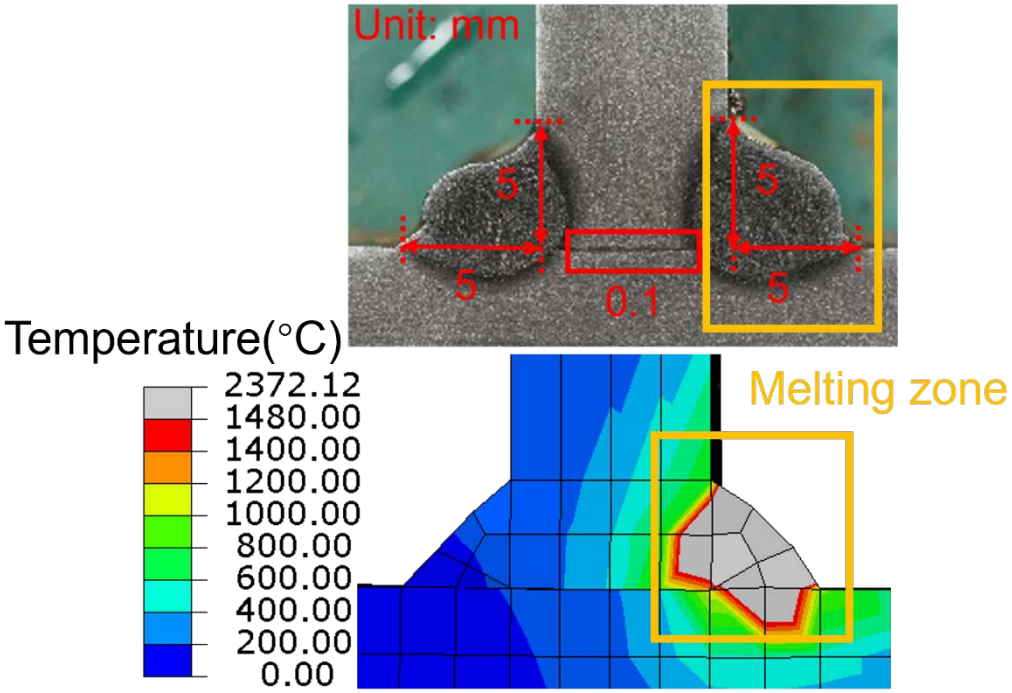

Figure 2-5 Melting zone in experiment and simulation

2.3.3 Experimental and analytical results

2.3.3.1 Temperature history

To investigate the simulation accuracy of two thermal input methods, this study numerically reproduced temperature histories at four thermocouples (TC1-TC4) as shown in Figure 2-6. Given measurement consistency across triplicate specimens, representative specimens were selected for each thickness. All four models demonstrated precise temperature field replication: Thermal efficiencies were 0.65 (9 mm) and 0.60 (12 mm) for the DU method, versus 0.80 and 0.75 for the CD method, respectively. Although intra-thickness efficiency variations existed, all values fell within typical arc welding ranges.

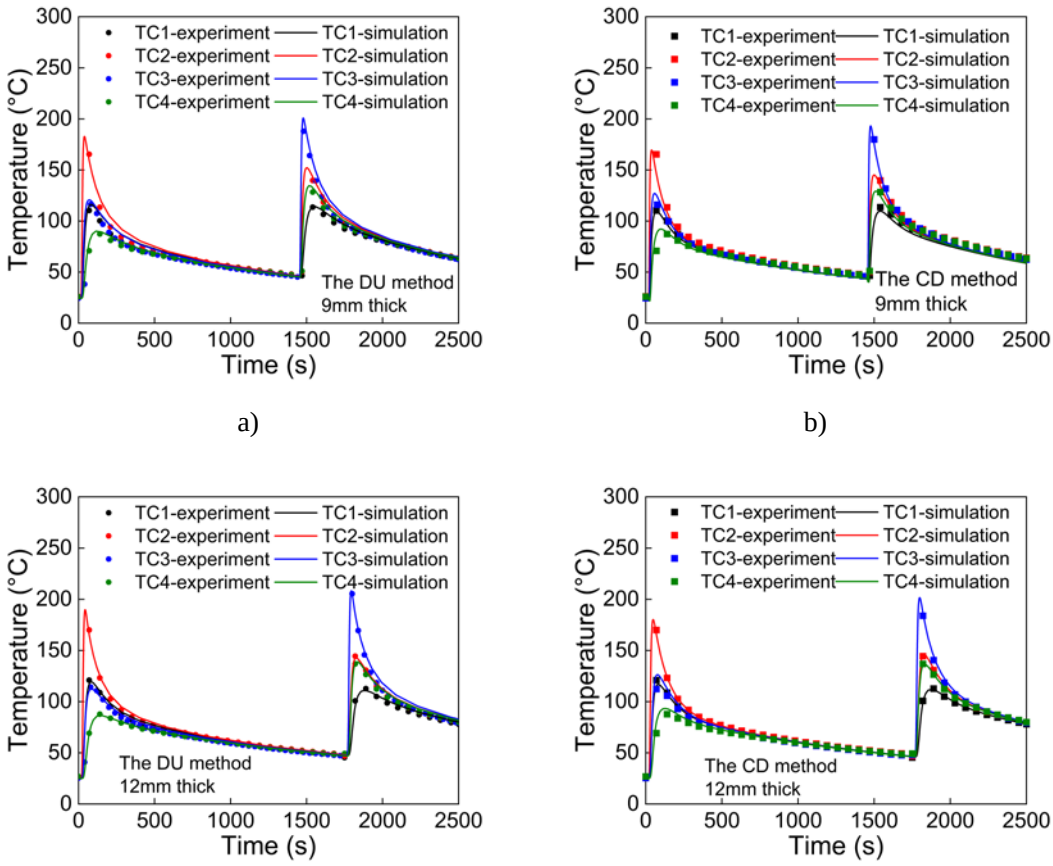

Figure 2-6 Temperature histories of models with a) 9 mm thickness using DU method b) 9 mm thickness using CD method c) 12 mm thickness using DU method d) 12 mm thickness using CD method

2.3.3.2 Out-of-plane deformation

Out-of-plane deformation comparisons (Figure 2-7) revealed computational results within experimental mean±range bands, where z-direction displacements were extracted at Figure 2-1 orange-line nodes. Specifically, 9 mm specimens showed negligible deformation differences between methods, whereas 12 mm specimens exhibited larger deformations with the CD method, the mechanism of which will be analyzed subsequently. Although both methods met engineering accuracy thresholds, the CD method's predictive capability can be further enhanced through heat source optimization (e.g., dynamic flux

modulation, molten pool convection enhancement), with improvement strategies detailed in forthcoming research.

2.3.3.3 Residual stress

Figures 2-8 and 2-9 systematically present the residual stress distributions along the welding (*y*) and transverse (*x*) directions. Stress characterization was conducted along the blue reference line in Figure 2-1, with specimens subjected to 630 °C/4 h stress relief annealing prior to welding to eliminate initial stresses. Residual stress components were quantitatively characterized via X-ray diffraction (XRD), where experimental data represent mean±SD of triplicate measurements per specimen, while simulated values were extracted from nodal stresses along the referenced line. Owing to transient thermal cycling and material anisotropy, significant inter-specimen variability was observed, necessitating a focus on distribution trend congruence. Numerical simulations successfully replicated macroscopic gradient patterns: High tensile stresses at the weld center transitioning to compressive zones with increased distance. Although discrepancies were present between analytical and experimental results, the analytical results successfully predicted the overall experimental trend.

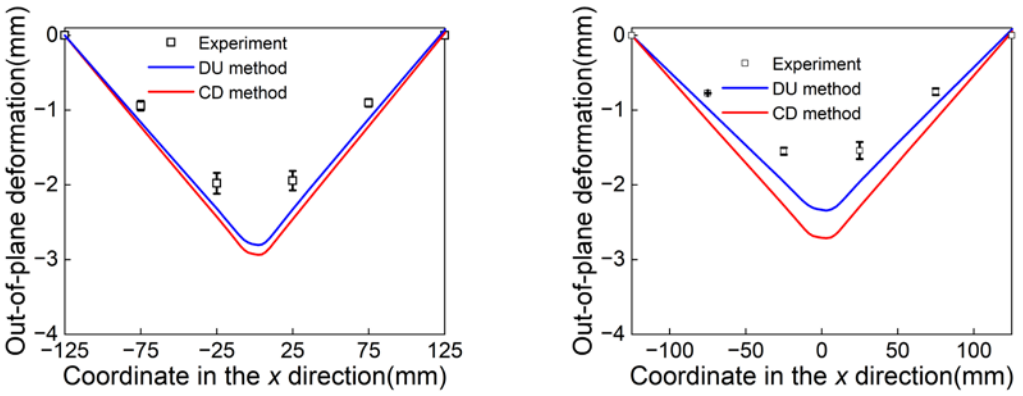

a) b)

Figure 2-7 Out-of-plane deformation of thicknesses of a) 9 mm and b) 12 mm

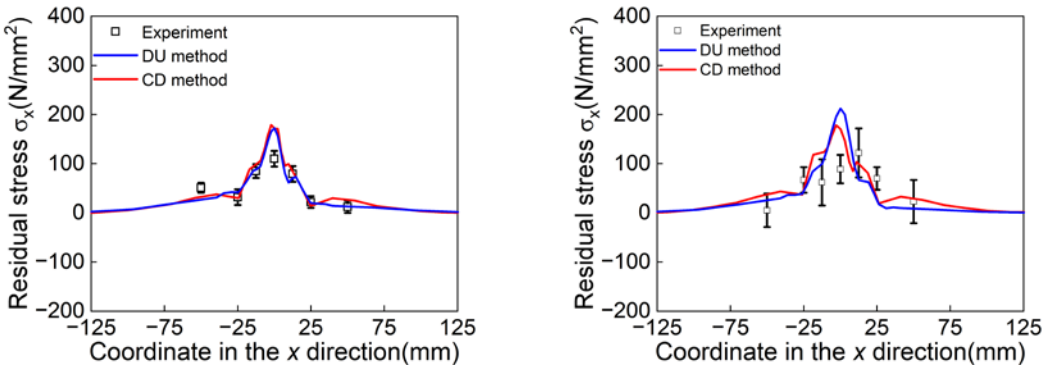

a) b)

Figure 2-8 Residual stress in the *x* direction of thicknesses of a) 9 mm and b) 12 mm

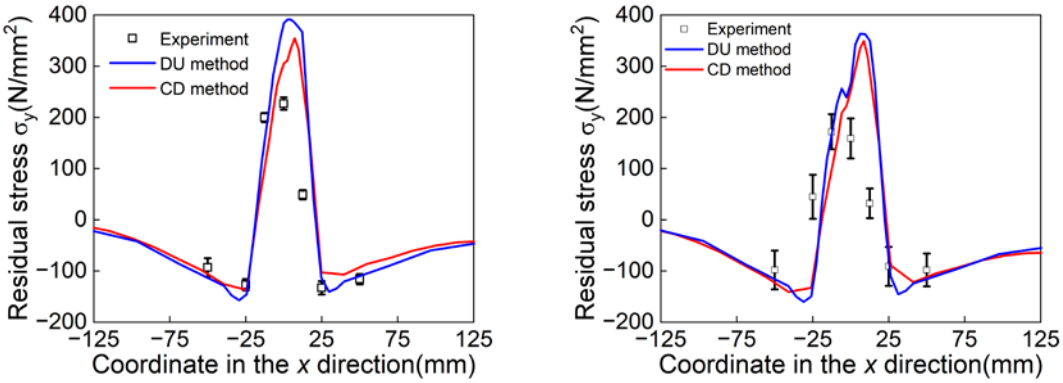

a) b)

Figure 2-9 Residual stress in the *y* direction of thicknesses of a) 9 mm and b) 12 mm

2.3.3.4 Computational time

To quantitatively evaluate the computational efficiency of thermal input methodologies, numerical experiments were conducted on an 8-core computing platform with 2.50 GHz processors. As summarized in Table 2-3, the simulation durations for 9 mm models were 77 min 32 s (the DU method) versus 64 min 39 s (the CD method), while 12 mm models required 80 min 5 s (the DU method) and 68 min 28 s (the CD method), respectively. The CD method demonstrated 17.4% and 14.6% computational efficiency improvements for 9 mm and 12 mm models compared to the DU method. Despite increased computational scale, the CD method's continuous heat source loading strategy reduced manual intervention steps and decreased iteration convergence counts, achieving optimal resource allocation. The findings demonstrate that CD heat input models achieve computational efficiency while maintaining precision relative to DU heat input models. This observation highlights the effectiveness of the CD method, making it advantageous for scenarios requiring resource optimization without compromising accuracy.

Table 2-3
Computational time for the models with different heat input methods

Thickness of Base/rib plate (mm)	Heat input method	Computational time
9/9	DU method	77 min 32 s
	CD method	64 min 39 s
12/12	DU method	80 min 5 s
	CD method	68 min 28 s

2.4 Welding simulation by combining solid and shell elements

2.4.1 Numerical simulation model

As shown in Table 2-3, while the Continuous Distributed (CD) method reduces computational time by 16.7% and 14.5% against the Discontinuous Uniform (DU) method in 9 mm and 12 mm models, its efficiency gains remain constrained. To solve this issue, a multi-scale modeling strategy combining solid-shell elements is proposed. To systematically validate the efficacy of hybrid element modeling methodology, this chapter conducts a comparative analysis between conventional solid-element models and shell-solid hybrid element models.

Although solid elements provide superior accuracy compared to shell elements, they require increased computational resources. Nevertheless, given the triangular cross-sectional geometry of weld beads, shell elements cannot adequately represent this geometric complexity. Conversely, solid elements accurately capture weld bead geometry, which is critical since these regions receive direct heat application. The geometric characteristics of weld beads significantly influence welding mechanical behavior [2.11, 2.12].

The shell-solid hybrid methodology capitalizes on individual element advantages: solid elements excel in heat input simulation for weld beads, while shell elements reduce computational demands for rib and base plates without compromising accuracy.

Previous research by Ma et al. [2.20] also explored solid-shell hybrid modeling strategies. As shown in Figure 2-10 a), a typical hybrid model adopts solid elements for both the base plate and rib plate near the weld zone. While this method offers modeling convenience, it introduces a high density of solid elements. Moreover, due to the 0.1 mm gap between plates, mesh generation for weld beads becomes challenging. Very fine

meshes are required to prevent element distortion or misalignment at the weld interface, which may otherwise lead to convergence issues or inaccurate results. On the other hand, if both the base and rib plates are directly replaced by shell elements—as illustrated in Figure 2-10 b)—the rib plate tends to induce excessive stress on the mid-plane of the base plate during simulation. Additionally, the mesh alignment issue near the weld zone due to the 0.1 mm gap remains unresolved. To address these problems, this chapter proposes an improved hybrid shell-solid modeling approach, as illustrated in Figure 2-11.

Figure 2-11 illustrates the detailed layout of the shell-solid hybrid model. Within this configuration, white regions denote weld beads, while green and blue areas represent rib and base plates. The improved hybrid shell-solid method employs solid elements for weld bead simulation and shell elements for rib and base plate modeling. For steel plates, where thickness dimensions are substantially smaller than other directional lengths, thin plate assumptions apply, making shell elements suitable for simulation. Shell element integration employs Simpson's rule with five integration points. The hybrid models contain only 1155 and 1092 nodal points for 9 mm and 12 mm thicknesses, respectively, whereas pure solid element models require 3528 and 5586 nodal points for corresponding thicknesses.

In this configuration, the rib plate is divided into two separate parts, allowing the placement of shell elements between weld beads. This modification not only mitigates the excessive stress observed in the shell-only model of Figure 2-10 b) but also resolves mesh compatibility issues seen in both prior approaches in Figure 2-10.

Connection configurations include: base plate attachment to weld bead bottom surfaces, rib plate I connection to rib plate II, and rib plate II connection to weld bead sides. Shell element nodal points couple with corresponding solid element nodes, as detailed in Figure

2-11. For rib plates I and II, shell element edges contact solid element surfaces, while base plate shell surfaces interface with solid element surfaces. Shell and solid element nodal points share identical displacement, temperature, and other parameters.

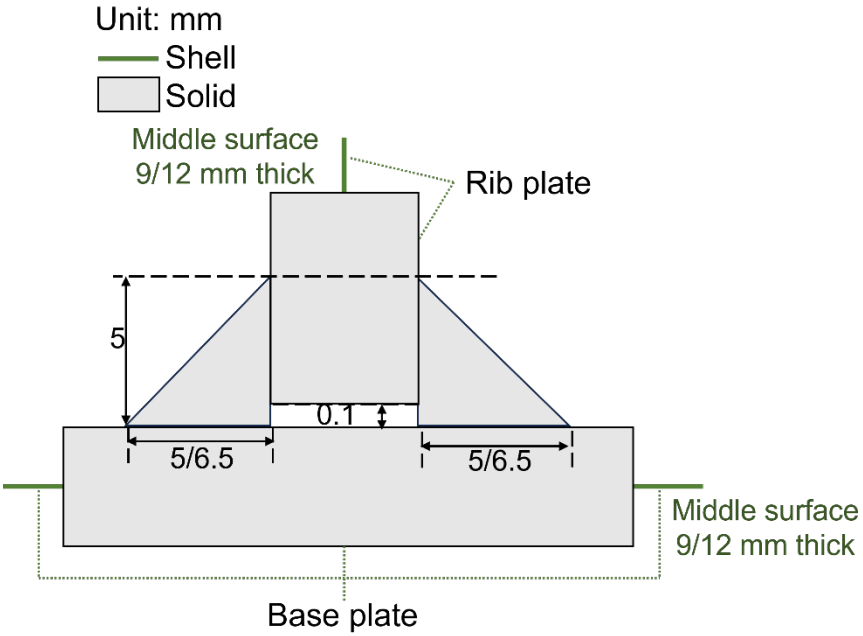

a)

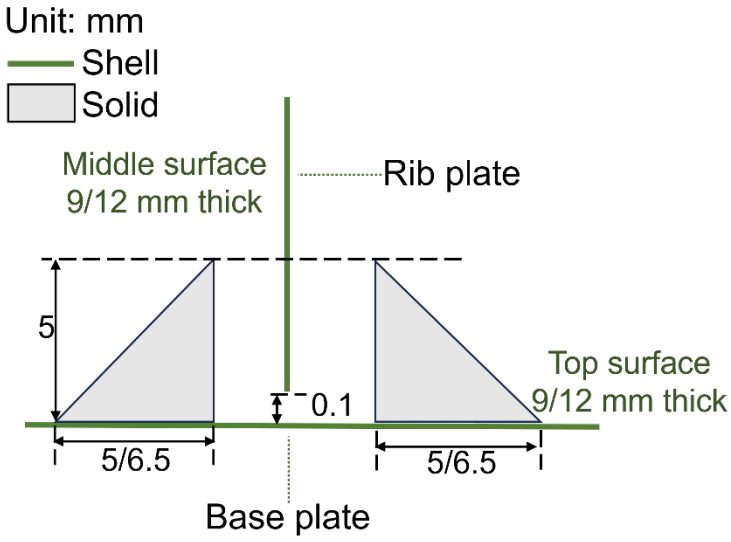

b)

Figure 2-10 General modeling methods for the shell-solid hybrid model

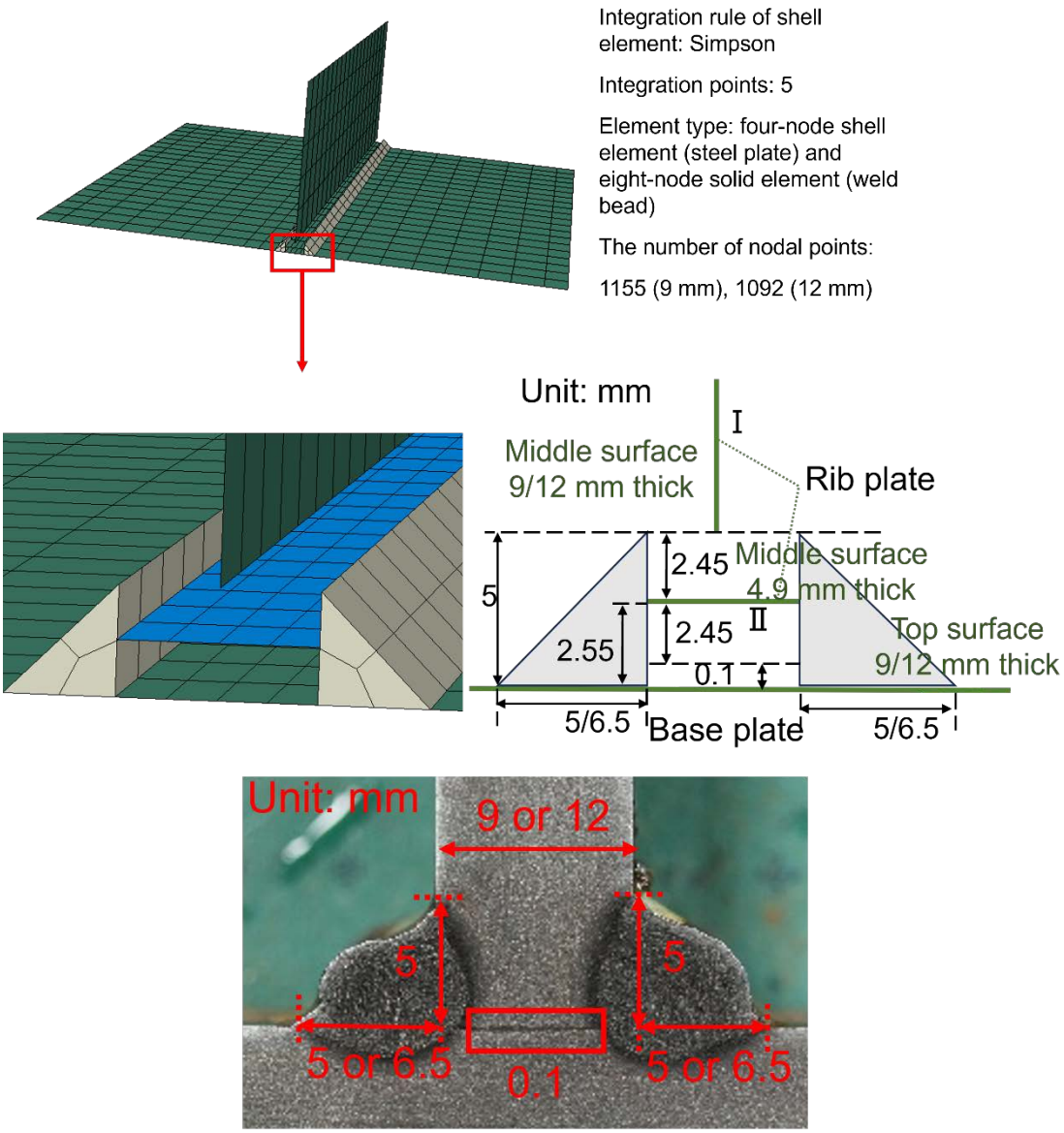

Figure 2-11 Detailed layout of the improved shell-solid hybrid model

2.4.2 Experimental and analytical results

2.4.2.1 Temperature histories

Thermal efficiencies remained constant at 0.8 and 0.75 for 9 mm and 12 mm shell-solid T-joint models, respectively, maintaining parametric equivalence with solid-element models to ensure comparable thermal input conditions. As demonstrated in Figure 2-12, temperature histories from 9 mm and 12 mm thick models exhibited high-fidelity alignment with experimental data at critical characteristics. The preserved thermal efficiency parameters validated that the hybrid strategy achieved equivalent energy transfer modeling through advanced interface coupling algorithms, with confirming negligible thermodynamic simplification errors from shell elements in thin-plate regions.

2.4.2.2 Out-of-plane deformation

As illustrated in Figure 2-13, this chapter validates the superiority of shell elements in thin-plate welding deformation simulation through comparative analysis of hybrid shell-solid versus pure solid models. The hybrid shell-solid model demonstrated superior alignment with experimental trends relative to the solid-type model. According to Kirchhoff-Love plate theory [2.13], shell elements with 5-point Simpson integration precisely resolve through-thickness stress gradients, and out-of-plane deformation from shell-solid hybrid models is more consistent with experimental data. This is attributable to shell elements' superior bending effect resolution, which proves shell-based modeling effectively mitigates solid element shear locking, establishing a theoretically rigorous and computationally efficient framework for high-precision welding deformation prediction.

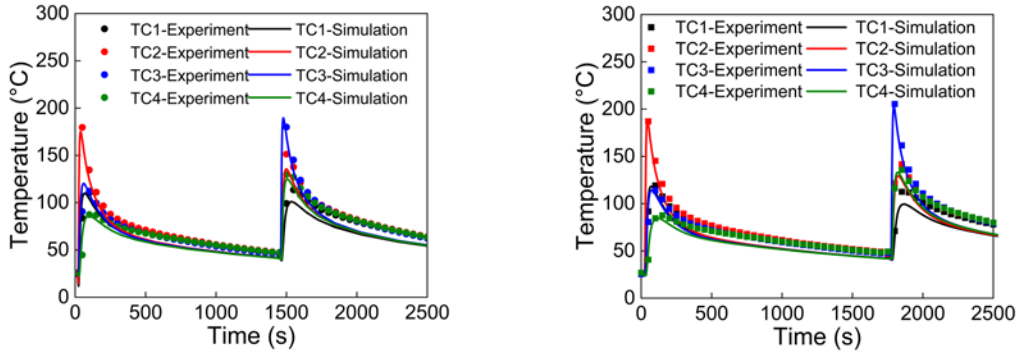

a) b)

Figure 2-12 Temperature histories of shell-solid type with the thickness of a) 9 mm and b) 12 mm

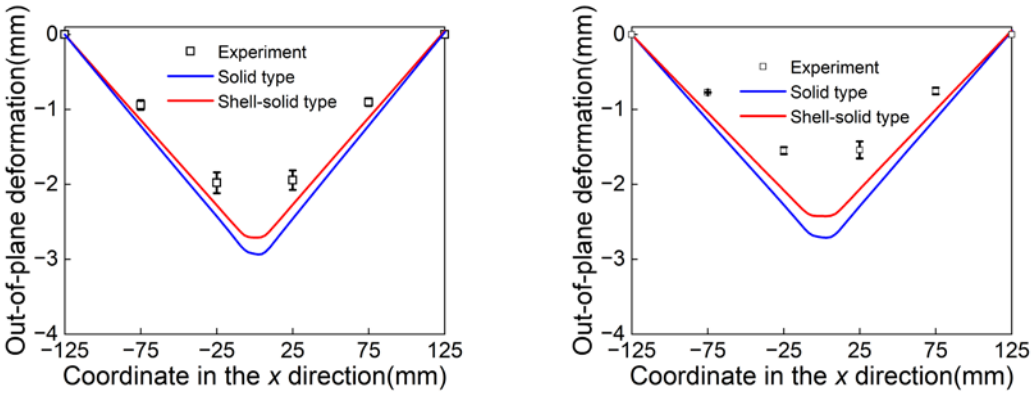

a) b)

Figure 2-13 Out-of-plane deformations for a) 9 mm and b) 12 mm thick T-joint models

2.4.2.3 Residual stress

Figures 2-14 and 2-15 characterize the residual stress distributed in the *x* and *y* directions, respectively. Both solid and shell-solid hybrid models effectively capture the global experimental trends despite localized deviations, with consistent performance across different thicknesses. Stress predictions at shell-solid interfaces align closely with experimental measurements, confirming the validity of interfacial coupling algorithms.

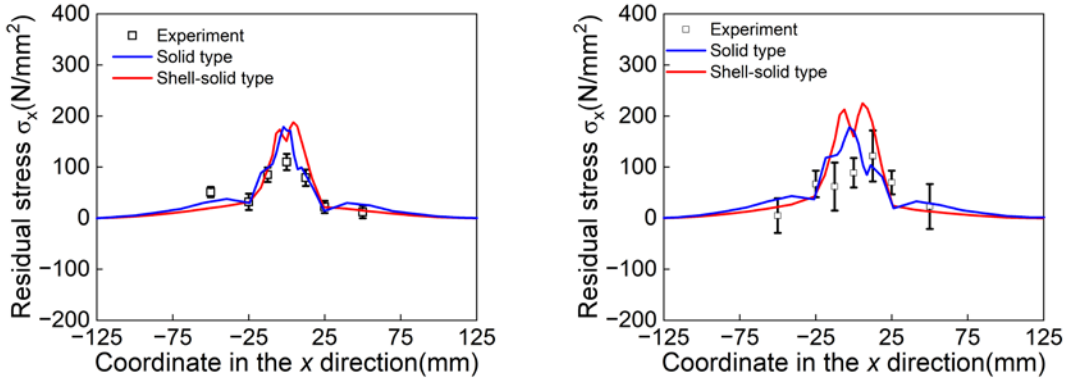

a) b)

Figure 2-14 Residual stress in the *x* direction of thicknesses of a) 9 mm and b) 12 mm

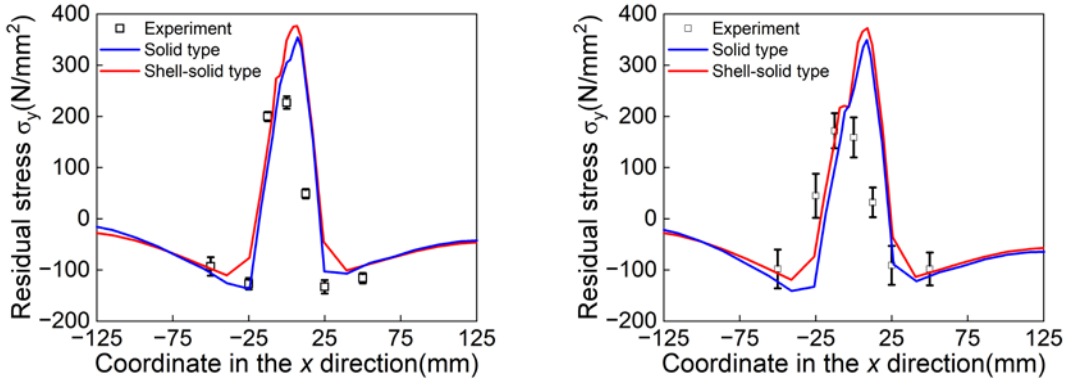

a) b)

Figure 2-15 Residual stress in the *y* direction of thicknesses of a) 9 mm and b) 12 mm

2.4.2.4 Computational time

Table 2-4 compares computational durations across different element types and thermal input methods. Results demonstrate that both the CD method and shell-solid hybrid models reduce computational costs regardless of plate thickness. While the standalone CD method provides limited time reduction, it significantly simplifies modeling procedures. The shell-solid hybrid approach demonstrates exceptional computational efficiency, requiring merely 27% and 38% of the computation time needed by solid-element models for 9 mm and 12 mm specimens, respectively, while maintaining high fidelity to experimental data. This optimization stems from differentiated discretization:

Solid elements precisely resolve 3D thermo-mechanical effects in weld zones, while shell elements reduce dimensional redundancy in base/rib plates, cutting total nodes by 67%-80%. This methodology successfully balances computational efficiency with precision requirements, delivering an industrial-grade solution for welding simulations.

Table 2-4
Computational time for all the models

Thickness of Base/rib plate (mm)	Heat input method	Element type	Computational time
9/9	DU method	Solid	77 min 32 s
	CD method	Solid	64 min 39 s
	CD method	Combined shell-solid	17 min 33 s
12/12	DU method	Solid	80 min 5 s
	CD method	Solid	68 min 28 s
	CD method	Combined shell-solid	26 min

2.5 Summary

Through combined experimental testing and numerical simulation, this chapter establishes efficient finite element methodologies for modeling T-joint fillet welding processes. The key findings are summarized below.

(1) To optimize modeling procedures and decrease computational time, the CD method was developed, which considers continuous movement and Gaussian energy distribution for heat input simulation. The proposed method reduces the complexity of the model modeling process and also reduces the need for function calls, improving the model's efficiency.

(2) Compared with the conventional Discontinuous Uniform (DU) heat input method, models employing the Continuous Distributed (CD) heat input method demonstrate reduced computational time. However, using the CD method alone does not yield

substantial time savings. To achieve significant computational efficiency improvements, an improved hybrid modeling strategy combining solid and shell elements that accounts for assembly gaps between base plates and ribs was proposed in this chapter. This shell-solid coupled simulation model accurately reproduces experimental temperature histories, out-of-plane deformations, and residual stress distributions. For 9 mm and 12 mm thick plate models, the hybrid method requires only 27% and 38% of the computation time compared to full solid-element models, respectively. This methodology maintains modeling accuracy while achieving remarkable computational efficiency gains.

References

2.1 Chandramohan, D. L., Roy, K., Taheri, H., Karpenko, M., Fang, Z., & Lim, J. B. (2022). A state of the art review of fillet welded joints. *Materials, 15*(24), 8743.

2.2 Sugun, B. S., & Sandeep, D. N. (2016). Development of single-layer 3D ‘T’profile with fillet for composite ‘T’joints. *Journal of Industrial Textiles, 46*(3), 887-900.

2.3 Abbasi, S., Ladani, R. B., Wang, C. H., & Mouritz, A. P. (2021). Improving the structural properties of composite T-joints by z-weaving of continuous metallic filaments. *Composite Structures, 260,* 113509.

2.4 Li, Y., Xue, J., Qi, L., Wang, X., Yuan, Z., & Xue, G. (2024). Residual stress model of welded steel L-shaped and T-shaped sections. *Journal of Constructional Steel Research, 218,* 108724.

2.5 Hanji, T., Tateishi, K., Kano, S., Shimizu, M., Tsuyama, T., & Takebuchi, T. (2020). Fatigue strength of transverse attachment steel joints with single-sided arc weld using low transformation temperature welding consumable. *Welding in the World, 64*, 1293-1301.

2.6 Aung, M. P., Katsuda, H., & Hirohata, M. (2019). Fatigue-performance improvement of patch-plate welding via PWHT with induction heating. *Journal of Constructional Steel Research*, *160*, 280-288.

2.7 Deng, D., Murakawa, H., & Liang, W. (2007). Numerical simulation of welding distortion in large structures. *Computer methods in applied mechanics and engineering*, *196*(45-48), 4613-4627.

2.8 Anca, A., Cardona, A., Risso, J., & Fachinotti, V. D. (2011). Finite element modeling of welding processes. *Applied Mathematical Modelling*, *35*(2), 688-707.

2.9 Dupont, J. N., & Marder, A. R. (1995). Thermal efficiency of arc welding processes. *Welding Journal-Including Welding Research Supplement*, *74*(12), 406s.

2.10 Friedman, E. (1975). Thermomechanical analysis of the welding process using the finite element method. *Transactions of the ASME, Journal of Pressure Vessel Technology, 97*(3), 206–213.

2.11 Zhang, Y. M., Kovacevic, R., & Li, L. (1996). Characterization and real-time measurement of geometrical appearance of the weld pool. *International Journal of Machine Tools and Manufacture*, *36*(7), 799-816.

2.12 Wang, X., & Li, R. (2014). Intelligent modelling of back-side weld bead geometry using weld pool surface characteristic parameters. *Journal of Intelligent Manufacturing*, *25*, 1301-1313.

2.13 Kiendl, J., Bletzinger, K. U., Linhard, J., & Wüchner, R. (2009). Isogeometric shell analysis with Kirchhoff–Love elements. *Computer methods in applied mechanics and engineering*, *198*(49-52), 3902-3914.

3. Application of effective FE simulation methods to multi-pass butt-welded joints

3.1 Introduction

In Chapter 2, a simulation approach integrating the Continuous Distributed heat input method with both solid and shell elements was developed for the single-layer fillet welding process. Besides single-pass fillet welding, butt welding is another widely employed joining method. For thick plates, multi-pass welding—where numerous weld layers are deposited—is typically necessary to achieve full penetration, optimal microstructure, and desired mechanical properties. Beyond its critical role in structural joints, multi-pass butt-welding finds extensive application across a wide spectrum of components—ranging from pressure vessels, pipelines, ship hulls, heavy-machinery frames, automotive chassis, to aerospace structures [3.1-3.6].

In this chapter, butt-welded joint components are selected as the research focus. Initially, three-pass butt-welding experiments are conducted on these components. Subsequently, finite element simulation methods are utilized for welding process simulation. In the previous chapter, the proposed method only utilized the Continuous Distributed heat input method (CD method) didn't significantly improve computational efficiency compared to the Discontinuous Uniform heat input method (DU method). Given the CD method's marginal improvement in computational efficiency over the DU method, this chapter proposes enhancements to the CD method. A comparative analysis of computational performance between the model applying the enhanced CD method and the model applying the DU method was conducted to assess the efficacy and applicability of the proposed modifications.

3.2 Experiment

3.2.1 Specimen

For assessing the computational precision of welding simulation in this investigation, extensive experiments and comparative analyses were performed. The experimental methodology is detailed below [3.7].

A 500 mm-wide, 12 mm-thick steel plate incorporating a central V-groove was employed to fabricate a three-pass butt-welded joint via gas metal arc welding, as illustrated in Figure 3-1. The specimen's two end sections were each 300 mm long, while the central region measured 380 mm in length and 50 mm in width. The central V-groove extended 340 mm in length, featured a 1 mm root face, and exhibited a 50° opening angle. Two identical specimens were prepared. The base metal conformed to JIS G3106 SM400A structural steel, while the filler material was YGW11 welding wire in accordance with JIS Z3312. The steels' chemical compositions and mechanical properties are summarized in Table 3-1.

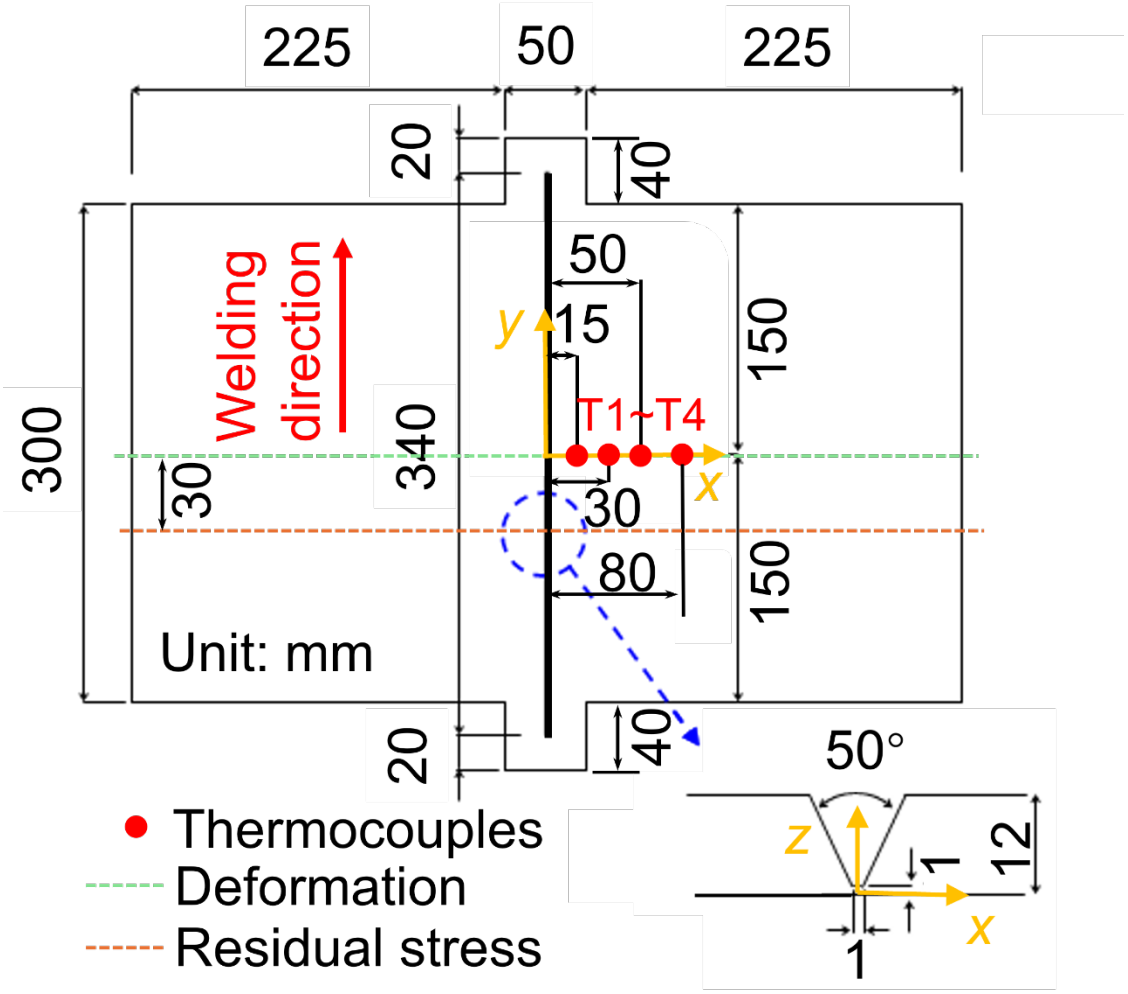

Figure 3-1 Shape and dimension of the specimen

Table 3-1

Mechanical properties and chemical compositions of materials

	Mechanical properties			Chemical compositions				
	Yield stress	Ultimate strength	Elongation	C	Si	Mn	P	S
	N/mm^2	N/mm^2	%	wt%				
Base metal	304	455	30	0.16	0.20	0.53	0.026	0.005
Welding wire (Catalogue value)	490	570	31	0.08	0.51	1.10	0.010	0.010

3.2.2 Experimental procedure

The internal stresses in the plates were first relieved by annealing prior to butt-welding. Welding was performed using the parameters listed in Table 3-2. To record thermal history, four K-type thermocouples were mounted on the plate's top surface at the positions indicated in Figure 3-1. Out-of-plane deformations measurements were obtained along the midspan (y = 0 mm) in the x direction at x = ±30, ±65, ±105, ±155, ±235, and ±250 mm (green line in Figure 3-1) utilizing dial gauge instrumentation. The plate edges served as reference points, and deformation at each location was determined as the difference between readings recorded before and subsequent to welding.

Residual stresses in the x-direction (y = –30 mm) were characterized via X-ray diffraction (XRD; μ-X360s, Pulstec Industrial Co., Ltd.) at the positions indicated by the orange line in Figure 3-1. Both x and y directional residual stresses were measured. In proximity to the weld bead, stresses were sampled at x = ±9, ±12, ±15, ±18, and ±21 mm with 3 mm increments. Further from the bead, measurements were taken at x = ±26, ±31, ±36, ±41, ±46, ±51, and ±56 mm with 5 mm increments. These two zones were chosen to characterize the residual stress gradient from immediately adjacent to the weld toward the plate ends.

Table 3-2 Welding conditions of each pass

	Current	Voltage	Speed
Pass	A	V	mm/s
1	120	20	5.2
2	115	20	2.8
3	105	20	2.1

3.3 Numerical simulation

3.3.1 Numerical simulation model

A coupled thermal-mechanical finite element model was implemented for butt-welding process simulation in this section. The pertinent thermal and elastic-plastic analyses were presented in Chapter 2.

Finite element analysis was implemented via ABAQUS to simulate welding procedures on butt-joint specimens. Temperature-dependent elastic and plastic material properties, as plotted in Figure 3-2, were sourced from references [3.8, 3.9]. The true stress–strain relationships of base metal and weld metal are shown in Figures 3-2 b) and c), respectively. Convective heat loss from all exposed surfaces to the ambient air was imposed as the thermal boundary condition. Exploiting the geometric symmetry of the specimen, only one half of the specimen was meshed; symmetric constraints were then applied to the cut plane. Figure 3-3 shows a schematic representation of the finite-element model.

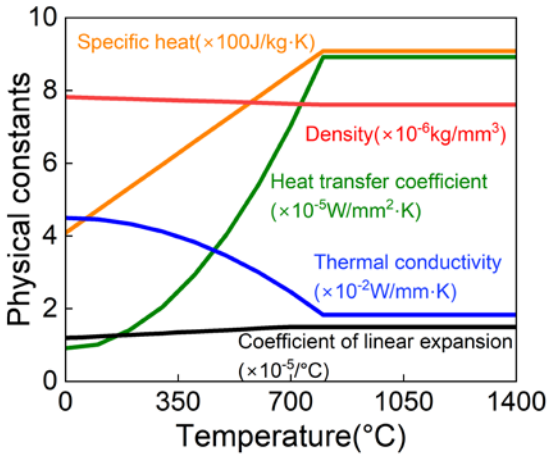

a)

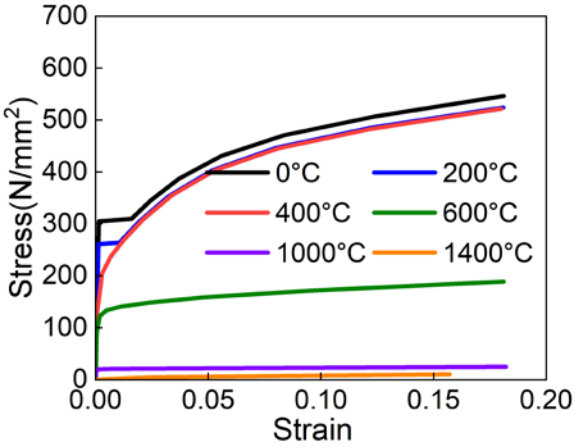

b)

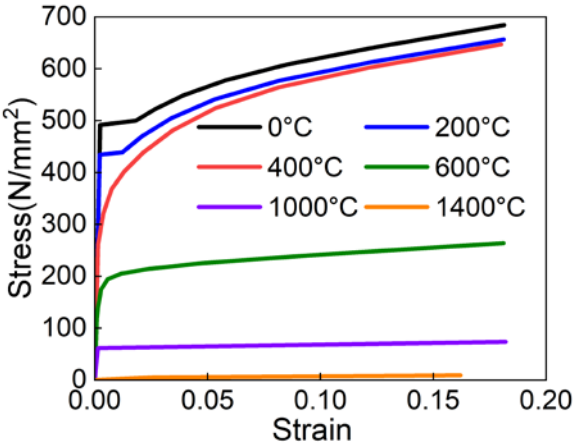

c)

Figure 3-2 a) Temperature-dependent physical constants and stress-strain relationships of b) base metal c) weld metal

Traditional thermal modeling approaches typically employ solid elements in computational simulations. Alternatively, shell element implementation offers enhanced computational efficiency through reduced nodal density [3.10, 3.11]. Chapter 2 presented an integrated modeling methodology that merges shell and solid element characteristics to optimize the relationship between computational simplification and precision maintenance. This combined thermal modeling approach—detailed in Chapter 2—continues to be employed in this chapter to balance computational efficiency and accuracy. In this approach, shell elements are assigned to the specimen's peripheral regions to reduce node count and thus shorten run times, while solid elements occupy the central zone to preserve fidelity (see Figure 3-3). For the shell regions, through-thickness integration is performed applying five-point Simpson integration technique.

Figure 3-3 illustrates the integration approach for connecting shell and solid elements. Regarding mechanical connectivity, nodal displacement and rotational values must maintain consistency at corresponding locations. To that end, each shell element was tied to the mid-surface of its adjacent solid elements via a shell–solid coupling constraint. Under this constraint, the rotational degrees of freedom of the shell elements are driven by the overall displacements of the solid-element nodes along their shared interface, ensuring seamless mechanical coupling between the two mesh types.

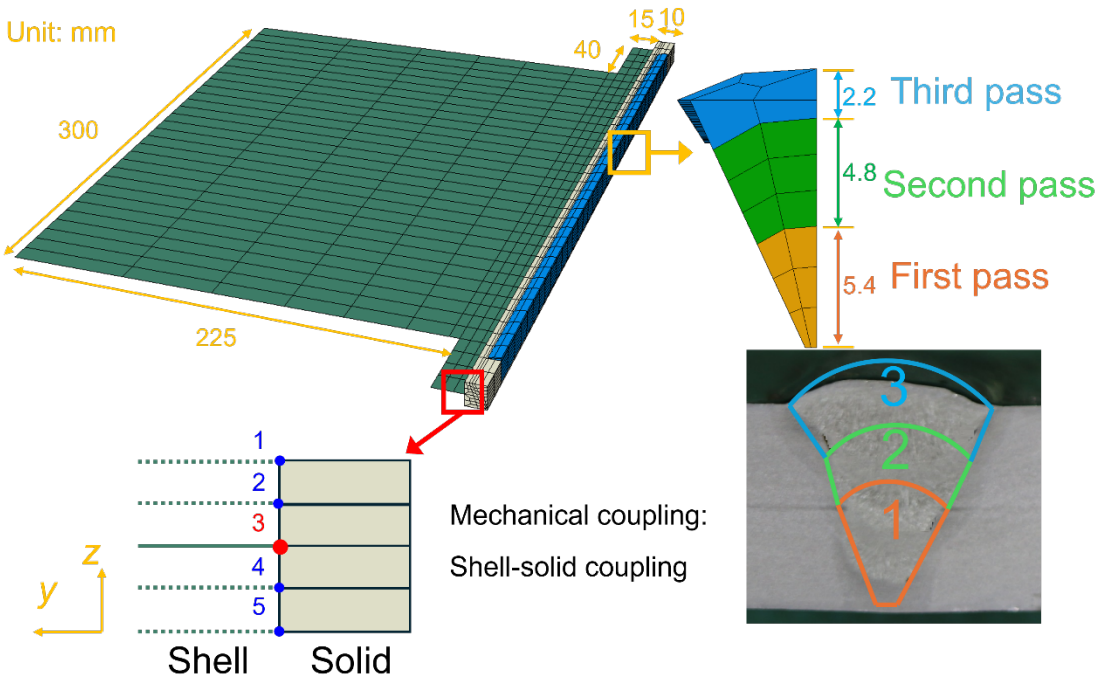

Figure 3-3 Finite element model of a three-pass welded joint (symmetry model)

Thermal coupling between shell and solid regions was established by matching each of the shell element's five through-thickness integration points with the nodes of the adjoining solid elements. Within ABAQUS, the temperature degrees of freedom (DOFs) for these shell-element integration points—numbered 1 through 5 from the uppermost layer down to the underside—are coupled directly to the corresponding temperature DOFs of the neighboring solid-element nodes. This nodal coupling enforces a continuous thermal field across the interface, ensuring that heat transfer is represented accurately throughout the combined mesh. By evaluating temperature at five discrete depths within the shell elements, the model is capable of resolving detailed through-thickness temperature gradients, thereby significantly improving the fidelity and precision of the overall thermal analysis.

3.3.2 Heat input methods

3.3.2.1 Discontinuous Uniform heat input method

Traditional thermal input modeling approaches generally implement heat application progressively following the welding path, corresponding to the mesh dimensions and segmentation count of the weld bead [3.12]. This technique ensures uniform thermal distribution throughout the heated zone of the weld bead. In Chapter 2, this approach was termed the “Discontinuous Uniform (DU) heat input method,” and that designation is preserved in the present chapter. From an accuracy perspective, this methodology fails to capture realistic thermal flow patterns by presuming homogeneous heat distribution across the heated zone. In terms of computational performance, the requirement to apply thermal loads to various regions and invoke functions repeatedly for each thermal input stage reduces model efficiency. The DU technique employed in this simulation partitions the weld into 34 sections along the welding trajectory. This simulation encompasses three welds totaling 105 phases: 102 thermal application phases and 3 cooling phases. Thermal energy delivered to the weld bead elements during the welding process was controlled through Equations (3.1) and (3.2). Heat transfer efficiency, accounting for energy dissipation between the welding apparatus and base materials, was established through iterative calibration to match experimental temperature profile data [3.13].

$$Q = \eta \frac{UI}{v} \tag{3.1}$$

$$q_m = \frac{Q}{A}\frac{v}{L} \tag{3.2}$$

Where:

- Q represents the amount of heat introduced by welding per unit length (J/mm),
- E represents the welding voltage (V),

- I represents the welding current (A),
- η represents the thermal efficiency of the process,
- v represents the welding speed (mm/s),
- A represents the cross-sectional size of the heat input zone (mm^2),
- L represents the length of the heat input zone (mm),
- q_m represents the welding energy supplied per unit time and unit volume ($J/s/mm^3$).

3.3.2.2 Continuous Distributed heat input method

To obtain more accurate thermal flux modeling and improve the computational performance of welding simulations, this study adopts and refines the novel heat-input approach introduced in Chapter 2, hereafter referred to as Continuous Distributed (CD) heat input method. In the present simulations, the CD method employs the double-ellipsoidal heat-source model to accurately replicate the actual characteristics of the heat flux. The heat input model, first introduced by Goldak [3.14], is mathematically described in Equations (3.3), (3.4), and (3.5).

The CD method's novel methodology employs simultaneous thermal loading of the complete weld bead while managing heat source movement through subroutine control. This approach reduces the requirement for iterative function execution, consequently enhancing the model's computational performance substantially. The simulation procedure was simplified to six phases: three for thermal phases and three for cooling phases. Through subroutine-based control implementation, the CD approach provided a more advanced and efficient framework for welding analysis.

$$P = \eta UI \tag{3.3}$$

$$Q_f(x,y,z) = 6\sqrt{3}\frac{f_f P}{abc_f\pi\sqrt{\pi}} exp\left(-3(\frac{x^2}{a^2}+\frac{y^2}{{c_f}^2}+\frac{z^2}{b^2})\right) \tag{3.4}$$

$$Q_r(x,y,z) = 6\sqrt{3}\frac{f_r P}{abc_r\pi\sqrt{\pi}} exp\left(-3(\frac{x^2}{a^2}+\frac{y^2}{{c_r}^2}+\frac{z^2}{b^2})\right) \tag{3.5}$$

Where:

- P represents the total introduced power (J/s),
- U represents the welding voltage (V),
- I represents the welding current (A),
- η represents the thermal efficiency of the process,
- Q_f and Q_r represent the volumetric heat flux density in front and rear model sections, respectively (J/s/mm^3),
- a, b, c_f, and c_r the width, depth, and length of the front and rear sections of the predicted molten pool (mm),
- x, y, and z represent point coordinates,as depicted in Figure 3-4.

Parametric investigations were performed systematically. Given the extensive parameter count, certain parameters required approximation. The heat input proportion coefficient f satisfies the condition ($f_f + f_r = 2$). Practical experience indicates that the relationship between f_f and f_r typically follows a 1:2 ratio. To ensure power continuity, the relationship $c_f : c_r = f_f : f_r$ must be maintained. The estimated molten pool depth approximately equals the front section length ($b = c_f$) [3.14].

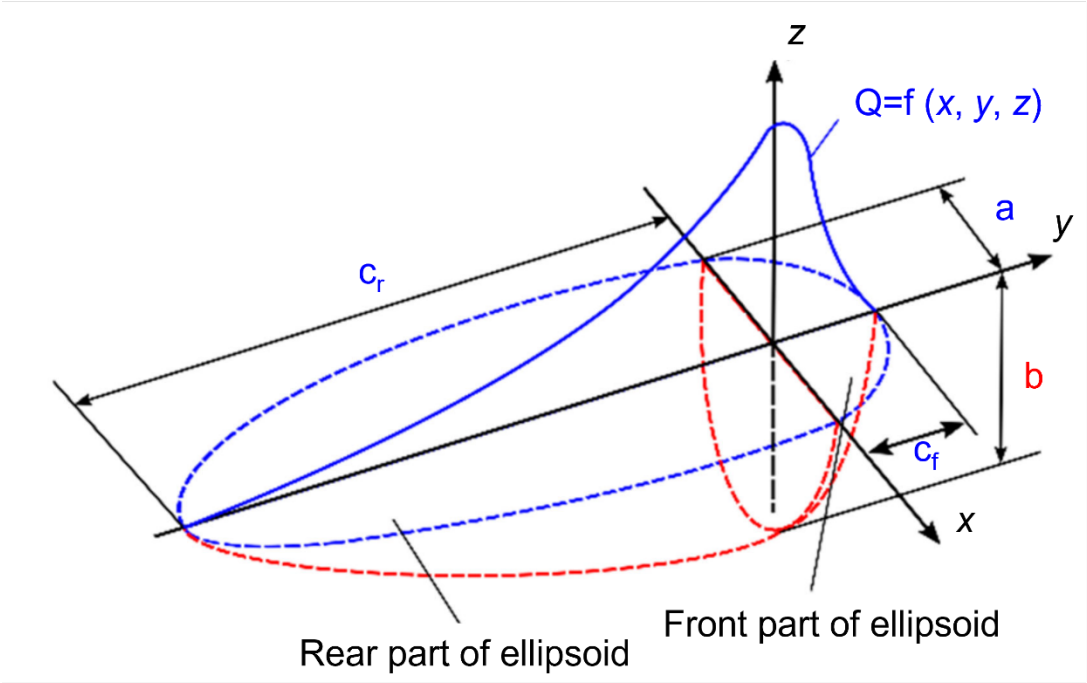

Figure 3-4 Double ellipsoidal heat source model for welding simulation

To identify optimal values for the double-ellipsoidal heat-source model, the projected half-width (a) and half-depth (b) of the weld pool were first estimated. These values were varied parametrically and compared against the experimentally measured half-width (W) and half-depth (D) listed in Table 3-3. The simulations revealed that ratios of $a{:}W$ or $b:D$ exceeding unity led to marked deviations from the physical data. Among the configurations tested, Model A2—characterized by $a{:}W$ and $b{:}D$ both equal to 0.9—demonstrated the closest match to the actual pool dimensions. Figure 3-5 illustrates overlayed fusion-zone cross-sections from both the experiments and the A2 simulation for all three weld passes.

a)

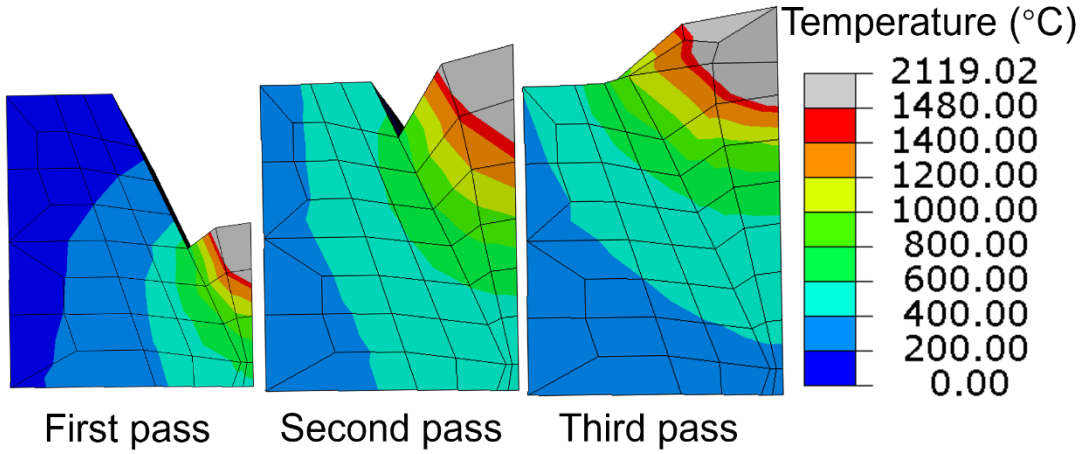

b)

Figure 3-5 Fusion zone profiles in butt welding: a) Experiment b) Simulation

Table 3-3 Different parameters of the double ellipsoidal heat source model

Model	A1	A2	A3	A4	B1	B2	B3
a:W	0.8	0.9	1.0	1.1	0.9	0.9	0.9
b:D	0.9	0.9	0.9	0.9	0.8	1.0	1.1

3.4 Experimental and analytical results

3.4.1 Temperature history

To evaluate the precision of the two heat input methods, temperature histories at four thermocouple locations were compared between experimental data and both simulation models, as depicted in Figures 3-6 and 3-7. The thermocouples were designated T1 through T4 in ascending order of their distance from the weld bead. Since both weld samples showed nearly identical thermal trends, only one set of measurements was used for detailed comparison. Each model faithfully reproduced the observed temperature cycles at all four sensors. The thermal efficiencies calculated for the Discontinuous Uniform (DU) heat input method and Continuous Distributed (CD) heat input method were 0.45 and 0.80, respectively—values typical for arc-welding processes. The relatively low efficiency of the model with the DU method (0.45) arises from its assumption of a uniform heat flux across the weld cross-section, which overestimates input near the bead edges [3.15]. To align the simulated temperature curves with actual weld thermograms, a reduced efficiency factor was imposed. This disparity highlights the necessity of refining heat-input representations, a central objective of the present work.

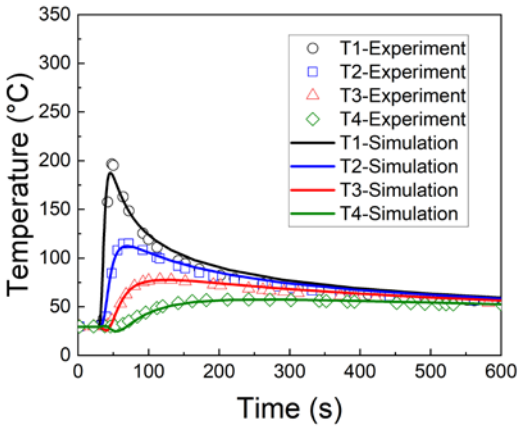

a)

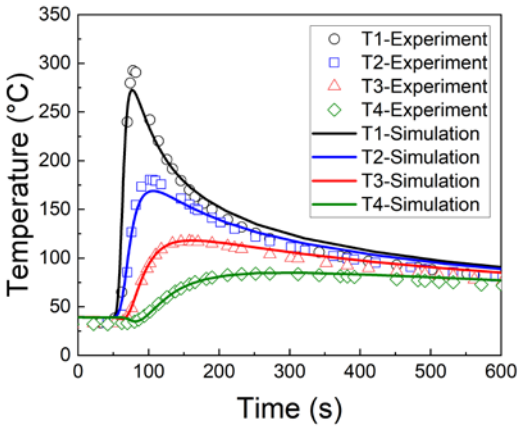

b)

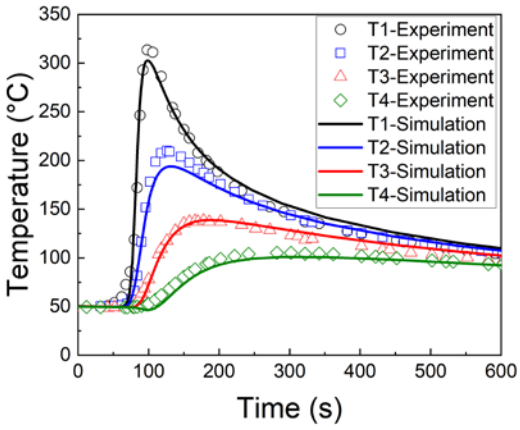

c)

Figure 3-6 Temperature histories for the a) first, b) second, and c) third welding passes using the DU method

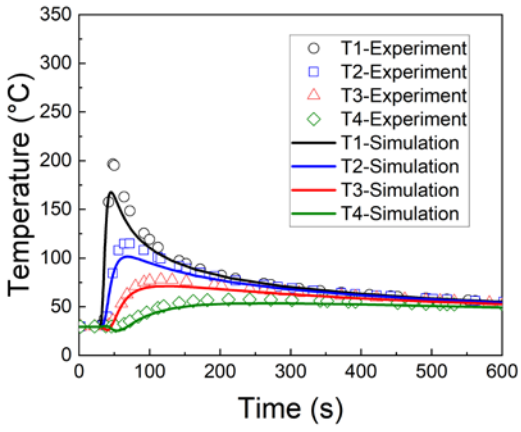

a)

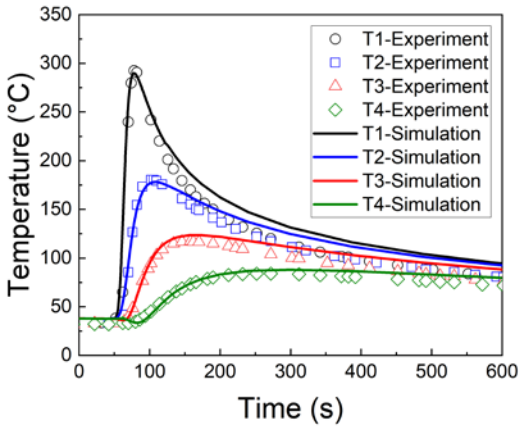

b)

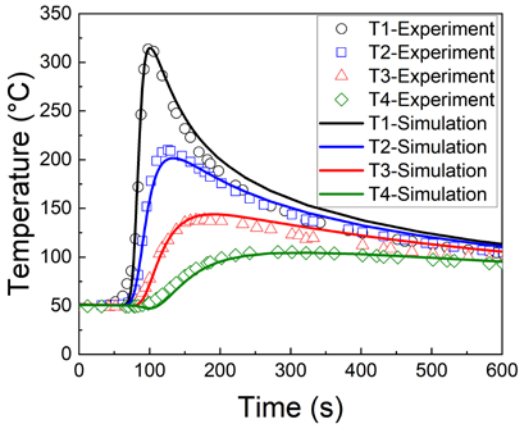

c)

Figure 3-7 T Temperature histories for the a) first, b) second, and c) third welding passes using the CD method

3.4.2 Out-of-plane deformation

Figure 3-8 compares the simulated out-of-plane displacements against the experimental measurements, which include both mean values and standard deviations. In the numerical model, out-of-plane nodal displacements were extracted along the green line indicated in Figure 3-1 to quantify vertical deflection. Results show that both heat-input schemes yield virtually identical deformation profiles, each matching the experimental data closely. This close correspondence confirms that both modeling approaches accurately capture the plate's out-of-plane deformation behavior under welding conditions, thereby demonstrating the reliability and effectiveness of the different heat input methods.

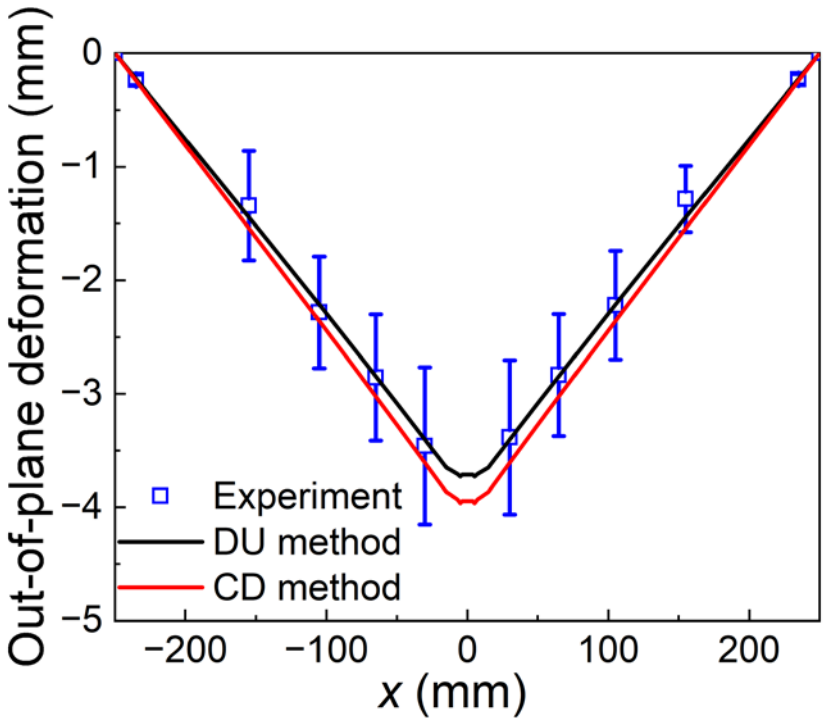

Figure 3-8 Deformation comparison between experiments and simulations using the DU and CD methods

3.4.3 Residual stress

Figure 3-9 depicts the distribution of residual stresses measured longitudinally (*y* direction) and transversely (*x* direction) along the orange reference line shown in Figure 3-1. The plotted experimental results incorporate both mean stress values and their associated standard deviations, offering a detailed portrayal of the residual-stress field. In the finite-element simulations, nodal stress data were likewise extracted along the same orange line and directly compared with the laboratory measurements. Overall, both heat-input formulations reproduce the broad trends of the experimental residual-stress profiles in the parent metal adjacent to the weld, confirming the models' ability to predict stress distributions with high fidelity.

The results show that the two modeling approaches diverge in their predicted peak stress magnitudes within the weld fusion zone. Because X-ray diffraction (XRD) techniques struggle to yield accurate residual-stress readings inside the weld—owing to its heterogeneous microstructure—the experimental validation in that region remains uncertain. Consequently, this investigation emphasizes the stress-gradient patterns in the base metal rather than the weld itself. Future efforts will target enhanced measurement and modeling strategies to resolve and validate the residual-stress state within the weld zone more precisely.

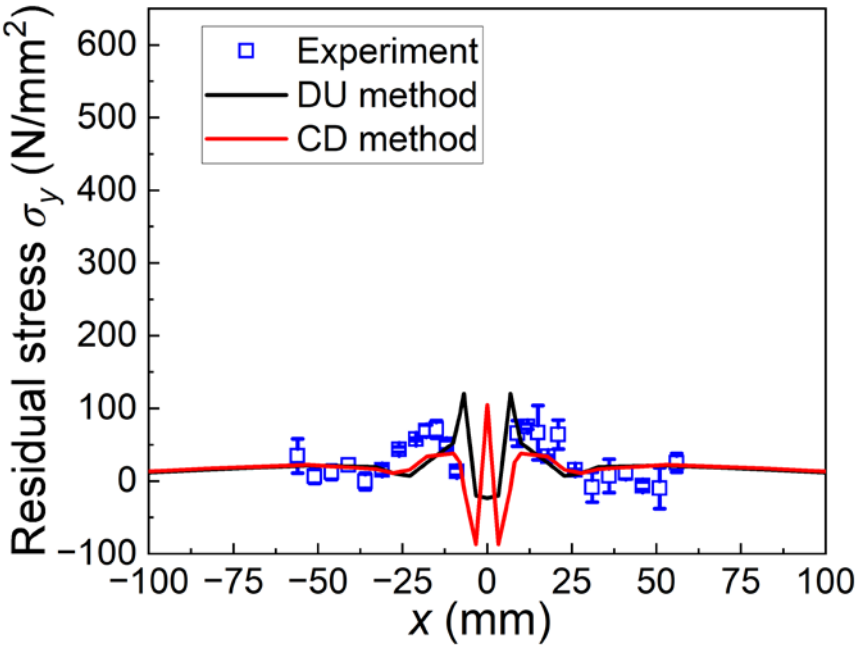

a)

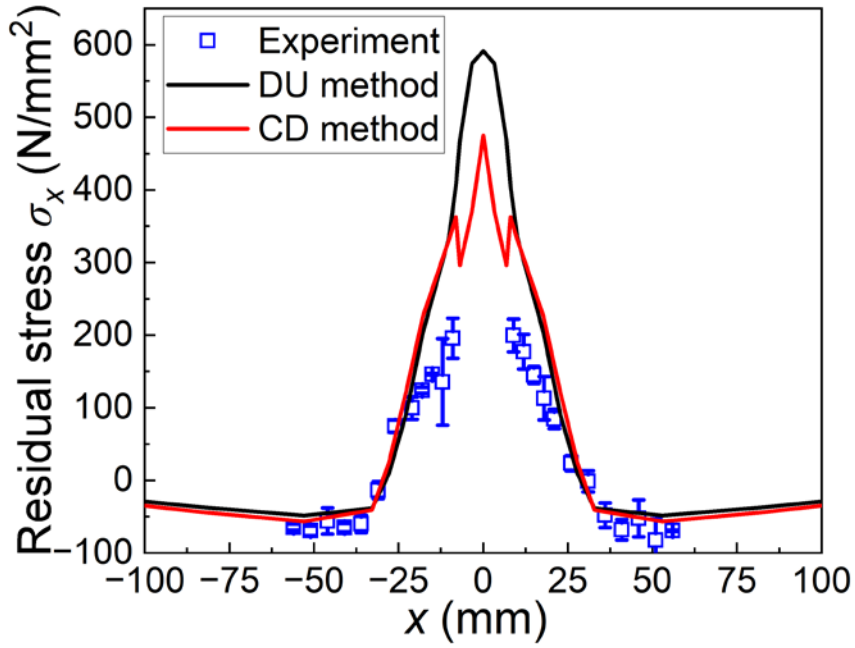

b)

Figure 9 Residual stresses comparison in the a) *x* direction and b) *y* direction between experiments and simulations using the DU and CD methods

3.4.4 Computational time

To enable a fair comparison of computational performance between the two heat-input strategies, both simulations were carried out on the same workstation, equipped with a 2.50 GHz CPU and eight cores, under identical software and hardware settings. Table 3-4 summarizes the execution times: the DU model completed in 57 min 34 s, whereas the CD model required only 26 min 30 s, representing a reduction of over 50 % in runtime. This significant time saving, achieved without sacrificing predictive accuracy, underscores the superiority of the CD method. Although the relatively small specimen size in this study kept overall runtimes modest, the dual benefits of reduced computational cost and maintained fidelity suggest that the CD method will offer even greater advantages when applied to larger or more geometrically complex components. Future work will explore scalability by extending the simulations to plates and structures of increased dimensions, assessing how performance gains evolve with specimen size.

Table 3-4
Computational time of models with different heat input methods

Heat input method	DU method	CD method
Computational time	57 min 34 s	26 min 30 s

3.5 Summary

This chapter employed a comprehensive approach that integrated experimental verification with computational modeling to establish and evaluate an enhanced FEM framework for three-pass butt-joint welding procedures. The key findings are outlined below:

(1) The hybrid modeling strategy combining solid and shell elements introduced in

Chapter 2—originally validated for single-layer fillet welds—was demonstrated to be equally applicable to multi-pass butt-welding configurations. Comparative analyses of thermal cycles, deformation patterns, and residual-stress distributions confirmed that the same modeling assumptions and material laws accurately capture both simple and complex welding sequences, thereby validating the method's broad utility.

(2) By substituting the Discontinuous Uniform (DU) heat input method with the Continuous Distributed (CD) heat input method, simulation runtimes were reduced by more than 50 % (from 57 min 34 s to 26 min 30 s) while maintaining predictive accuracy. This significant acceleration underscores that the choice of heat-source model is a critical determinant of overall computational performance. Accordingly, selecting or tailoring an appropriate heat-input scheme is essential for achieving high-fidelity results with efficient use of computational resources.

References

3.1 Serindağ, H. T., & Çam, G. (2022). Multi-pass butt welding of thick AISI 316L plates by gas tungsten arc welding: Microstructural and mechanical characterization. *International Journal of Pressure Vessels and Piping*, *200*, 104842.

3.2 Park, J. U., An, G., & Woo, W. (2018). The effect of initial stress induced during the steel manufacturing process on the welding residual stress in multi-pass butt welding. *International Journal of Naval Architecture and Ocean Engineering*, *10*(2), 129-140.

3.3 Brickstad, B., & Josefson, B. L. (1998). A parametric study of residual stresses in multi-pass butt-welded stainless steel pipes. *International Journal of pressure Vessels and piping*, *75*(1), 11-25.

3.4 Deng, D., Zhang, C., Pu, X., & Liang, W. (2017). Influence of material model on prediction accuracy of welding residual stress in an austenitic stainless steel multi-pass butt-welded joint. *Journal of Materials Engineering and Performance*, *26*,

1494-1505.

3.5 Dovzhenko, N. N., Demchenko, A. I., Bezrukikh, A. A., Dovzhenko, I. N., Baranov, V. N., Orelkina, T. A., ... & Lopatina, E. S. (2021). Mechanical properties and microstructure of multi-pass butt weld of plates made of Al-Mg-Zr alloy sparingly doped with scandium. *The International Journal of Advanced Manufacturing Technology*, *113*, 785-805.

3.6 Trupiano, S., Belardi, V. G., Fanelli, P., Gaetani, L., & Vivio, E. F. (2021). A novel modeling approach for multi-passes butt-welded plates. *Journal of Thermal Stresses*, *44*(7), 829-849.

3.7 Guan, X., Hirohata, M., & Chang, K. H. (2025). A streamlined FE method for deformation and residual stress prediction in butt welding using continuous heat input. *Welding in the World*, 1-11.

3.8 Hanji, T., Tateishi, K., Kano, S., Shimizu, M., Tsuyama, T., & Takebuchi, T. (2020). Fatigue strength of transverse attachment steel joints with single-sided arc weld using low transformation temperature welding consumable. *Welding in the World*, *64*, 1293-1301.

3.9 Aung, M. P., Katsuda, H., & Hirohata, M. (2019). Fatigue-performance improvement of patch-plate welding via PWHT with induction heating. *Journal of Constructional Steel Research*, *160*, 280-288.

3.10 Zhang, Y. M., Kovacevic, R., & Li, L. (1996). Characterization and real-time measurement of geometrical appearance of the weld pool. *International Journal of Machine Tools and Manufacture*, *36*(7), 799-816.

3.11 Wang, X., & Li, R. (2014). Intelligent modelling of back-side weld bead geometry using weld pool surface characteristic parameters. *Journal of Intelligent Manufacturing*, *25*, 1301-1313.

3.12 Jiang, W. C., Wang, B. Y., Gong, J. M., & Tu, S. T. (2011). Finite element analysis of the effect of welding heat input and layer number on residual stress in repair welds for a stainless steel clad plate. *Materials & Design*, *32*(5), 2851-2857.

3.13 Dupont, J. N., & Marder, A. R. (1995). Thermal efficiency of arc welding

processes. *Welding Journal-Including Welding Research Supplement*, *74*(12), 406s.

3.14 Goldak, J., Chakravarti, A., & Bibby, M. (1984). A new finite element model for welding heat sources. *Metallurgical transactions B*, *15*, 299-305.

3.15 Michaleris, P., & DeBiccari, A. (1997). Prediction of welding distortion. *Welding Journal-Including Welding Research Supplement*, *76*(4), 172s.

4. Simulation of heating correction on welding deformation

4.1 Introduction

In Chapter 2, single-layered fillet welding was performed on T-joint specimens, during which weld-induced distortions were observed. To mitigate these deformations, heating correction exploits the thermal gradient between the plate's upper and lower surfaces, generating controlled bending moments that counteract weld-induced distortion. Owing to its straightforward implementation, cost-effectiveness, and excellent adaptability to various geometries, heating correction has become a widely adopted distortion-control technique in industrial manufacturing. As a simple yet efficient method, it can be easily integrated into production workflows to ensure component dimensional accuracy [4.1-4.5].

This chapter begins with heating experiments on steel plate specimens, the observed phenomena of which are analyzed using thermo-elastic-plastic theory to elucidate the underlying deformation mechanisms. Subsequently, heating correction trials are conducted on welded T-joint components, and a finite element model simulating the correction process was developed. In the FEM, a simplified heat-source model, derived from the thermal elastic-plastic analysis, is employed to efficiently replicate the localized thermal inputs. Finally, a parametric study of the simulation is performed to establish a streamlined yet robust heating correction model.

4.2 Heating experiment

4.2.1 Specimen

To validate the modeling accuracy of the welding process within this investigation, experimental testing and analytical comparisons were carried out to verify the outcomes. The experimental approach is outlined here [4.6-4.8].

The experimental specimens were square steel plates, each measuring 200 mm per side. The plates had thicknesses of 9, 12, and 25 mm. Figure 4-1 presents the specimen dimensions and geometries. A total of two specimens per thickness were tested. The material used was general structural steel SM400A, by JIS G3106. Table 4-1 summarizes the mechanical properties of the material, based on the mill test reports. To eliminate residual stress introduced during the rolling process, all specimens underwent annealing prior to heating.

4.2.2 Experimental procedure

In accordance with the Specifications for Highway Bridges (II Steel Bridges/Steel Members Edition) [4.9], steel surface temperatures during heating correction must remain below 750 °C for tempered steel to prevent microstructural alterations. In this study, the target surface temperature of the steel plate heated by a gas burner was maintained between 500 °C and 600 °C. Propane was used as the fuel, with oxygen serving as the oxidizer. The flame had a length of 70 mm, and its temperature ranged from 1,500 °C to 1,800 °C. The heat input was delivered to the center of one side of the specimen, with a heating time of 20s. Gas flow velocity was adjusted accordingly while monitoring flame conditions. Following heating, the specimens were left to reach ambient temperature

naturally. To record temperature distributions, the central temperatures of both front and rear surfaces were monitored with an InfRec R450Pro infrared camera.

Figure 4-2 depicts the specimen setup and heating conditions. During heating, specimens were held in place using a magnet. After heating, they were removed from the burner setup and allowed to cool freely without constraints. Since the gas flame jet covered the specimen surface and thermocouples during heating, accurate temperature measurement of the front surface was not feasible using the infrared camera or thermocouples. Consequently, the temperature distribution on the back surface of the specimen was selected as the reference for analysis.

Following the heating and cooling process, out-of-plane deformation was assessed using a dial gauge at nine points along the centerline of the specimen in the horizontal direction, with measurements taken at 25 mm intervals. The deformation was also recorded before heating, and the difference between pre- and post-heating measurements was used to determine the heating-induced deformation, as illustrated in Figure 4-1 b). Additionally, residual stress was analyzed using X-ray diffraction (μ-X360s, Pulstec Industrial Co., Ltd.) at seven points along the centerline in the vertical direction, with measurements taken at 15 mm intervals (Figure 4-1 b)). The X-ray diffraction system utilized a chromium radiation source with a collimator diameter of 1.0 mm. The operating voltage and current of the X-ray tube were set to 30 kV and 0.5 mA, respectively.

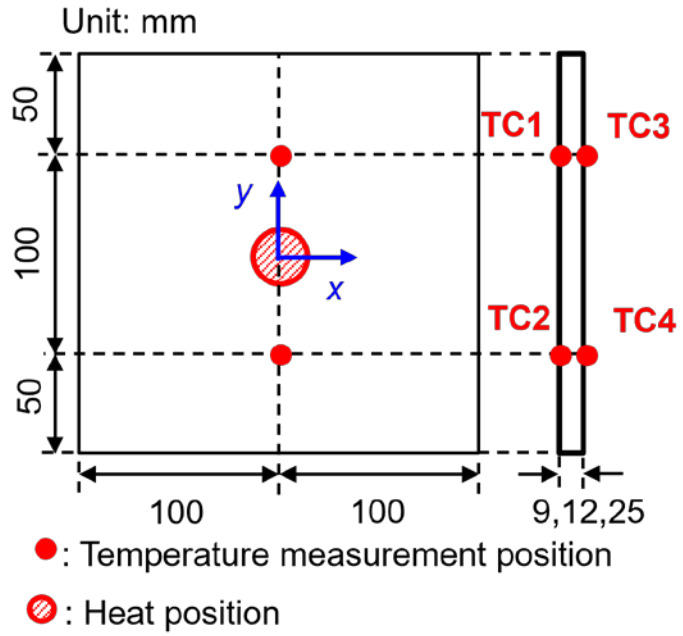

a)

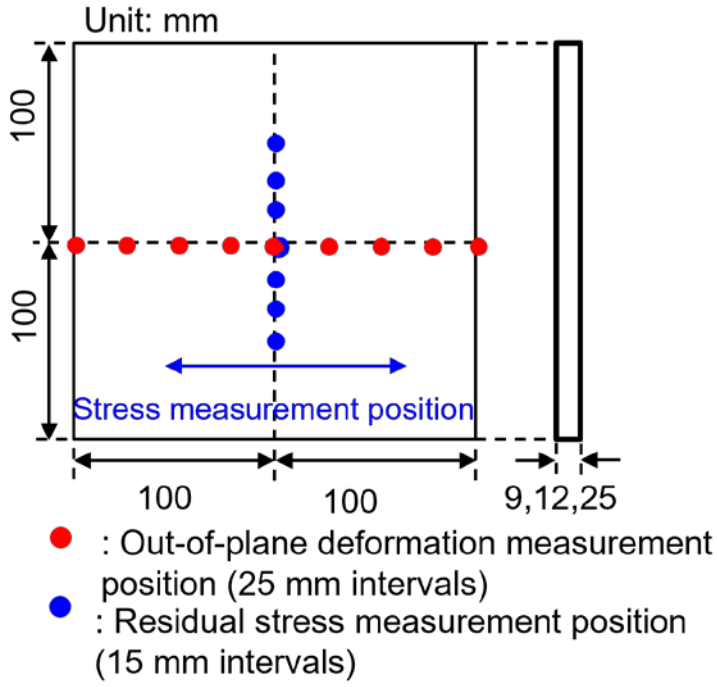

b)

Figure 4-1 Shapes and dimensions of steel plate specimens and measurement positions of a) temperature and b) out-of-plane deformation and residual stress on the steel plate specimens

Table 4-1

Mechanical properties of materials for steel plate specimens

Thickness (mm)	Yield strength (N/mm^2)	Tensile strength (N/mm^2)	Elongation (%)
9	333	442	30
12	294	422	34
25	301	442	33

Unit: mm

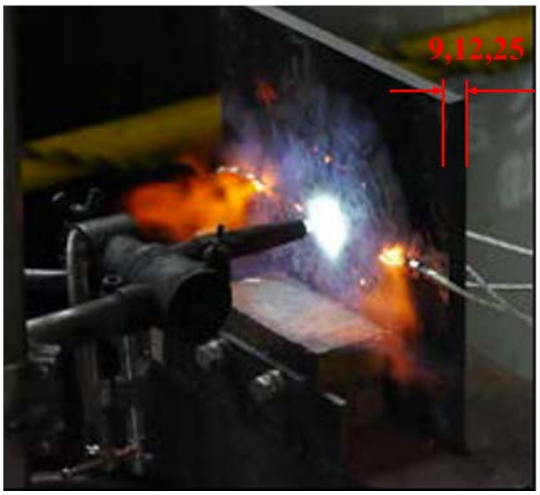

Figure 4-2 An image of a heating experiment on a steel plate specimen

4.2.3 Experimental results

Figure 4-3 presents the temperature histories of multi-point temperature measurements on steel plates during the heating process obtained using an infrared thermal imager, as well as the temperature variation during both the heating and cooling processes measured by thermocouples. When recording the temperature history of the front surface, the thermocouples are affected by the direct impingement of the gas flame, as illustrated in Figure 4-2, rendering accurate measurements infeasible. Therefore, only the temperature history of the rear surface is presented. For each specimen thickness, the variation between the two sets of measurements is minimal, and thus only one representative

dataset is shown for each case. The experimental results indicate that for specimens of different thicknesses, the heating rate at various locations generally follows the trend that the farther the location is from the center of the heated area on the steel plate, the lower the heating rate. However, at positions 10 mm and 24 mm away from the heating center, the heating rates are found to be approximately the same. The underlying reasons for this phenomenon will be discussed in Sections 4.2.4 and 4.2.5.

Figures 4-4 and 4-5 present the measured data of out-of-plane deformations and residual stress of the steel plates after the heating and cooling processes, respectively. It can be seen that the thinner the plate, the greater the out-of-plane deformation and the more pronounced the variation in residual stress.

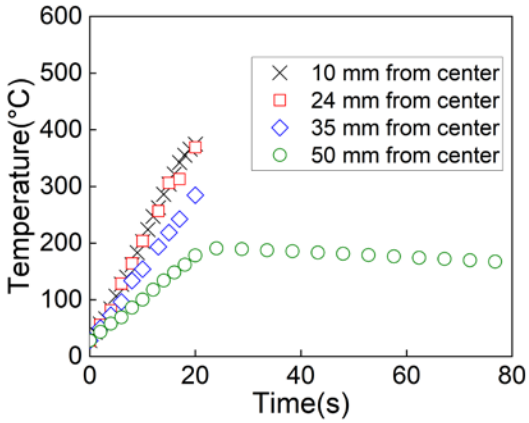

a) 9 mm

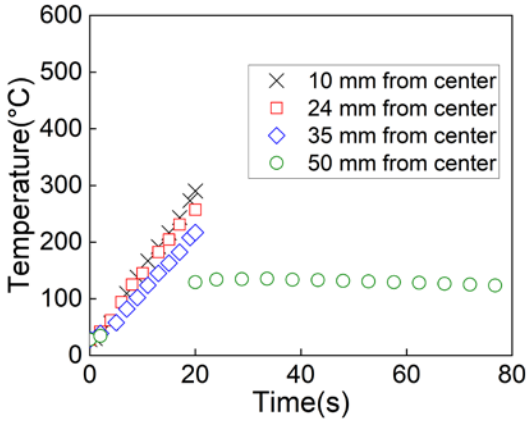

b) 12 mm

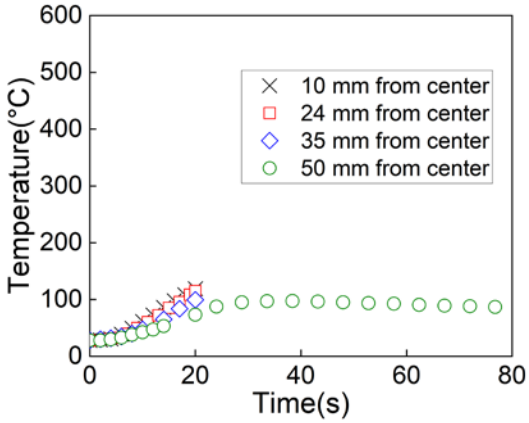

c) 25 mm

Figure 4-3 Temperature histories of a) 9 mm thick, b) 12 mm thick, and c) 25 mm thick steel plates

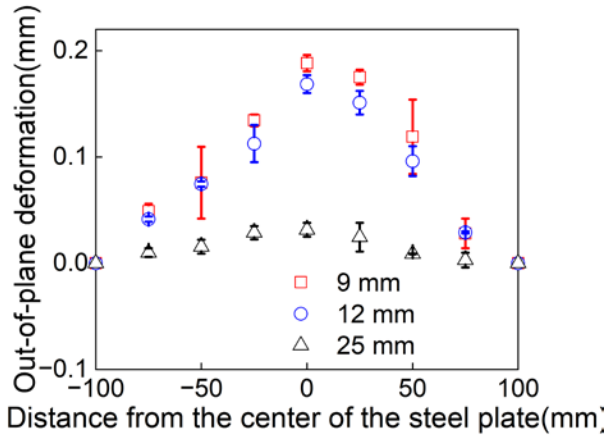

Figure 4-4 Out-of-plane deformations of the steel plates

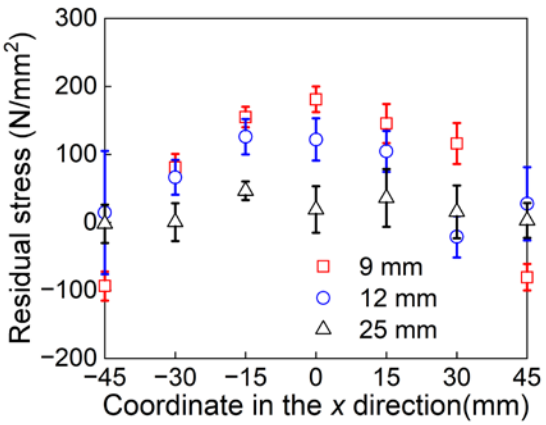

Figure 4-5 Residual stress of the steel plates

4.2.4 Features of temperature distribution

Figure 4-6 shows the temperature distributions measured at 1 s and 6 s after the start of heating, with the measurement taken on the back side of the 9 mm thick steel plate. The experimental investigation demonstrated that the peak temperature did not occur at the geometric center of the steel plate but rather at approximately 22 mm from the center. The observed deviation in the peak temperature location suggests that the heat transfer mechanism is influenced by the radial expansion of the flame and convective effects

rather than being dominated by direct stagnation-point heating.

Upon observing the heated surface of the steel plate, the thermal region can be preliminarily divided into three zones:

Direct flame impingement zone: This innermost region is characterized by direct contact with the flame jet, resulting in intense convective heat transfer and elevated local temperatures.

Flame edge impingement-diffusion zone: Situated adjacent to the direct impingement area, this intermediate zone experiences a combination of residual jet momentum and lateral heat diffusion, leading to complex thermal gradients.

Heat flux diffusion zone: The outermost region, where heat is primarily disseminated through conduction and ambient convection, resulting in comparatively lower temperature gradients.

The maximum temperature occurred in the flame edge impingement-diffusion zone, indicating that the interaction between the flame jet and the surrounding environment creates complex thermal-fluid behavior, as illustrated in Figure 4-7.

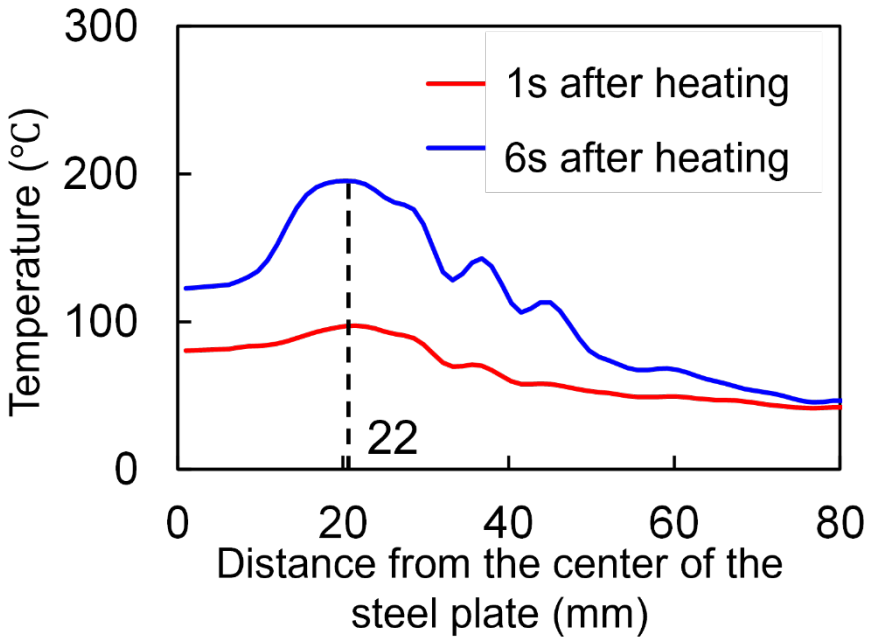

Figure 4-6 Temperature distributions obtained by the experiment from a 9 mm thick specimen

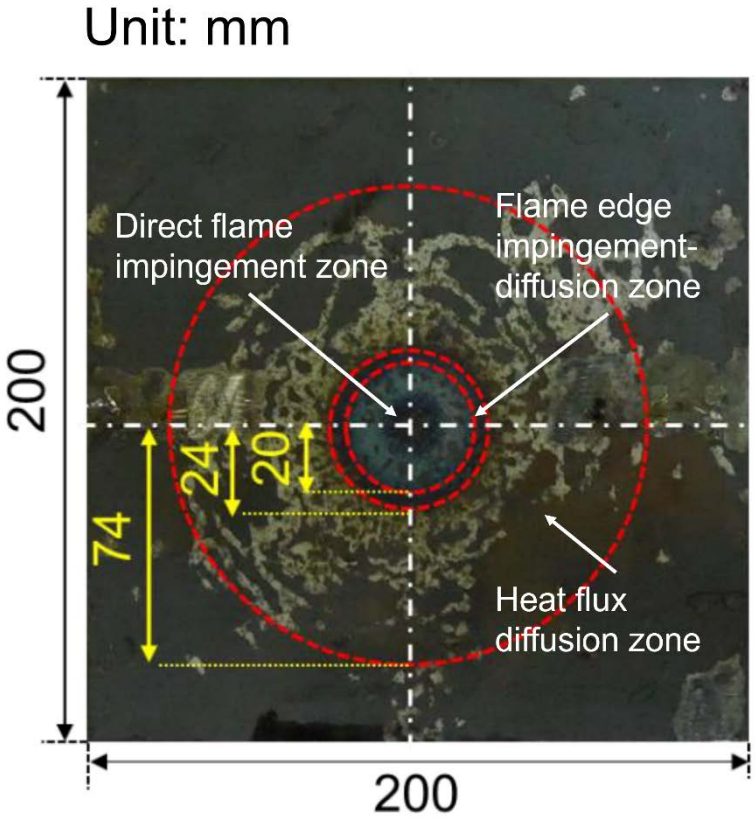

Figure 4-7 The surface of the 9 mm thick steel plate after heating

The deviation of the maximum temperature location from the center can be explained by considering the momentum and heat transfer characteristics of the impinging flame jet [4.10-4.13].

The centerline velocity v_{center} at the jet nozzle is determined by the mass flow rate $\dot{m}$ and the nozzle geometry [4.7-4.8], as shown in Equations (4.1-4.2):

$$v_{center} = \frac{\dot{m}}{\rho \cdot A} \tag{4.1}$$

$$A = \frac{\pi d^2}{4} \tag{4.2}$$

where:

- $\dot{m}$ is the mass flow rate (kg/s),
- ρ is the fluid density (kg/m³),
- A is the cross-sectional area of the nozzle (m²),
- d is the nozzle diameter (m).

At the boundary of the impingement zone ($r = r_c$), the velocity decreases due to radial momentum spreading but can be estimated using momentum conservation, as shown in Equation (4.3):

$$v_{boundary} = \frac{v_{center} \cdot r_c}{2h_r} \tag{4.3}$$

where:

- r_c is the radius of the jet impingement region (m),
- h_r is the effective thickness of the boundary layer (m).

The heat transfer coefficient (h) is a function of the local velocity and can be expressed using the Nusselt number (N_u), as shown in Equations (4.4-4.5):

$$N_u = C \cdot Re^p \cdot Pr^q \tag{4.4}$$

$$h = \frac{N_u \cdot \kappa}{L} \tag{4.5}$$

where:

- N_u is the Nusselt number,
- Re is the Reynolds number,
- Pr is the Prandtl number,
- C, m, n are empirical constants,
- κ is the thermal conductivity (W/m·K),
- L is the characteristic length (m).

For turbulent flow, p≈0.8; for laminar flow, p ranges from 0.33 to 0.5.

The local heat flux q_r at any radial position r is determined by the local heat transfer coefficient and the temperature difference, as shown in Equation (4.6):

$$q_r = h \cdot (T_s - T_\infty) \tag{4.6}$$

where:

- T_s is the surface temperature (K),
- T_∞ is the fluid temperature far from the surface (K).

For flame jet impingement, the heat transfer coefficient (h) varies radially and is often proportional to the velocity at the corresponding position, as shown in Equation (4.7):

$$h_r \propto \sqrt{v_r} \tag{4.7}$$

Combining this with the velocity relationship, as shown in Equation (4.8):

$$v_r = \frac{v_{center} \cdot {r_c}^2}{r^2} \tag{4.8}$$

the heat flux distribution can be expressed in Equation (4.9):

$$q_r = q_{r_c} \cdot \sqrt{\frac{{r_c}^2}{r^2}} \tag{4.9}$$

where q_{r_c} is the heat flux at the impingement zone boundary.

The observed shift of the maximum temperature away from the center can be attributed

to the non-uniform heat transfer characteristics of the impinging flame jet. While the highest heat flux typically occurs near the stagnation region, the redistribution of momentum and thermal energy significantly influences the temperature field. As the flame expands radially, the local velocity and convective heat transfer coefficient vary, leading to an enhanced heat flux near the boundary of the impingement zone rather than at the center. This effect is further intensified by the formation of secondary vortices and recirculation zones, which promote enhanced convective heat transfer near the flame's periphery.

Moreover, the thermal response of the steel plate plays a significant role in this deviation. Since the temperature measurements were conducted on the back side of the plate, the observed maximum temperature reflects not only the direct heat flux from the flame but also the heat conduction through the material. As a result, the interplay between convective heat transfer, radial momentum transport, and conduction effects determines the final temperature distribution, explaining why the peak temperature appears at approximately 22 mm from the center rather than at the geometric stagnation point.

4.3 Finite element analysis of heating

4.3.1 The simulation model

The heating experiments performed on steel plate specimens were computationally reproduced via finite element modeling, utilizing the commercial ABAQUS software for this investigation. To ensure that the temperature measurement positions of the thermocouples are consistent with the nodes of the model's mesh, the model was re-meshed, and the welding process was re-simulated. The thermal dependency of material mechanical attributes and physical parameters (Figure 4-8) was derived from previous

research findings [4.14, 4.15]. The stress and strain shown in Figure 4-8 were true stress and strain.

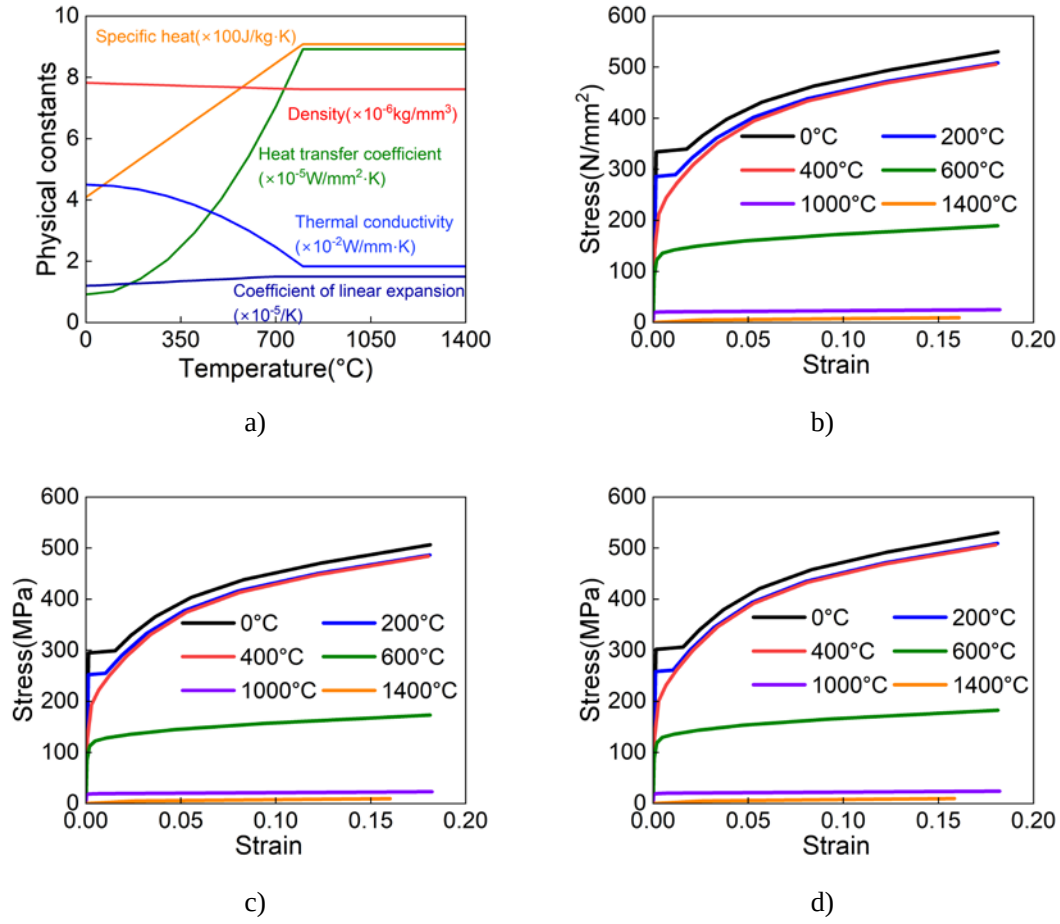

Figure 4-8 a) Temperature-dependent physical constants and stress-strain relationships of b) 9 mm-thick base metal c) 12 mm-thick base metal d) 25 mm-thick base metal

Heat dissipation from the model surfaces to the surrounding air was incorporated as the thermal boundary condition. The mechanical boundary condition involved constraining rigid body motion at the base plate corner locations, as illustrated in Figure 4-9.

The displacement of the blue point was constrained in the *x*, *y*, and *z* directions. The displacement of the red point was constrained in the *y* and *z* directions. The displacement of the orange point was constrained in the *z* direction. The heating time of the models is

based on experiments.

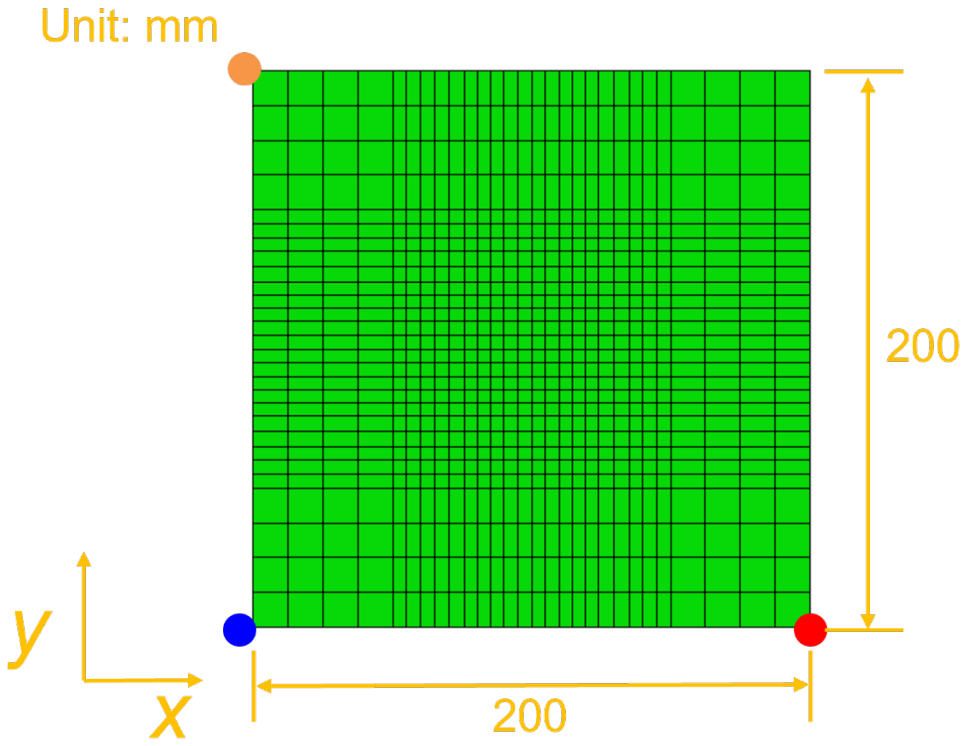

Figure 4-9 The simulation model for heating of the steel plates

4.3.2 Simplified heat input method

To simplify the simulation of thermal input while faithfully capturing the temperature peak within the flame-edge impingement–diffusion zone, a dual-Gaussian heat source model is employed, as shown in Equation (4.10). This model superposes two Gaussian distributions to represent the heat flux density in the direct impingement region and in the edge impingement–diffusion region, respectively. The distribution of the heat flux is schematically illustrated in Figure 4-10.

$$q(r) = A_1 e^{-r^2/{\sigma_1}^2} - A_2 e^{-r^2/{\sigma_2}^2} \quad (4.10)$$

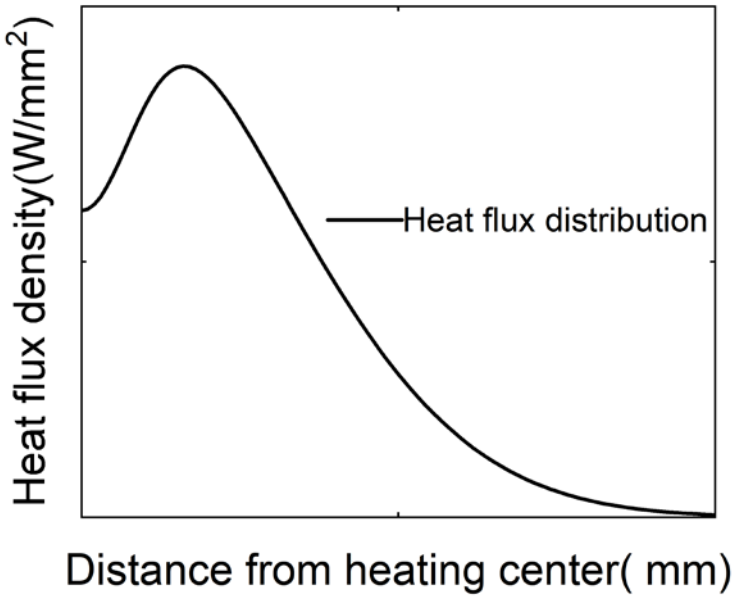

Figure 4-10 The schematic Illustration of the heat flux distribution

In the heating experiments, the measured radii of the direct impingement zone r_1, the edge impingement–diffusion zone r_2, and the heat-flux diffusion zone r_3 are 20,24,74 mm, respectively. Based on prior studies relating the Gaussian parameter σ to measurable radii—some advocating σ equal to the radius in the edge region, others suggesting heat flux decays to 5%–20% of its peak at the boundary [4.16-4.19]—the present work determines: σ_1 is set by r_3 and calibrated so that the heat flux density decays to 5% of its maximum at r_3; σ_2 is set by r_1 and calibrated so that the heat flux density decays to 5% of its maximum at r_1, thereby reflecting the highest temperature location in the edge-diffusion region; The amplitude coefficients A_1 and A_2 are obtained by fitting to the temperature history data shown in Figure 4-3.

This dual-Gaussian composite model offers a more physically realistic representation of the spatial decay characteristics of the flame heat source, particularly the

peak-temperature behavior at the diffusion edges. Moreover, the model's structure is straightforward, and its parameters are clearly defined, facilitating calibration based on experimental data.

4.3.3 Results and discussion

After calibrating the heat input model based on the observed phenomena and results of the steel plate heating correction experiments, the simulated temperature histories (Figure 4-11) closely reproduce the experimental results. Figure 4-12 compares the experimentally measured out-of-plane deformations with the corresponding simulation results. For each plate thickness, the experimental value is taken as the average deformation of two specimens. The simulation accurately reproduces the trend observed in the experiments: thinner plates exhibit larger out-of-plane deformation, and in all cases the front surface (directly heated by the gas flame) bulges outward. During heating, the front surface reaches a higher temperature than the back, producing greater thermal expansion; upon cooling, the temperature—and thus the shrinkage—variation between the front and back surfaces diminishes. Consequently, the dominant thermal expansion of the front surface leads to a convex deformation on that side.

Figure 4-13 presents the measured residual stresses alongside the simulation predictions. Residual stress was measured by X-ray diffraction on the non-heated (back) surface only, since the microstructural changes on the directly heated face can compromise measurement accuracy. For each thickness, the reported value is the average of two specimens. The simulation captures the experimental trend: as plate thickness increases, the back-surface temperature decreases and the residual stress correspondingly diminishes.

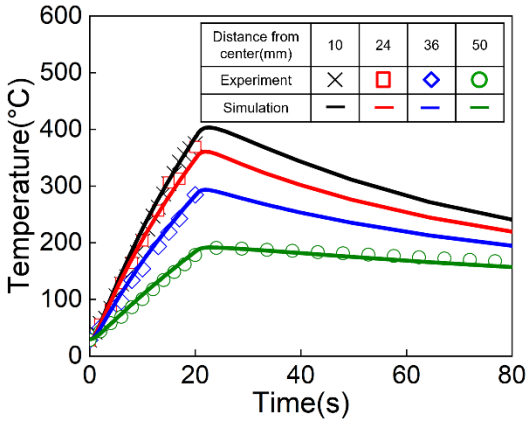

a) 9 mm

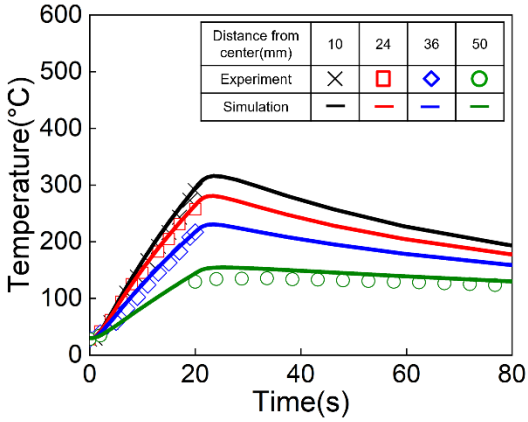

b) 12 mm

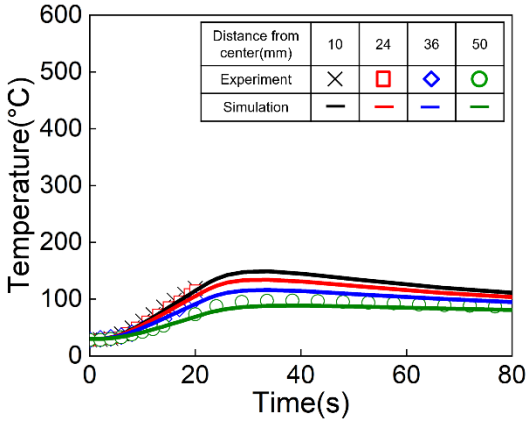

c) 25 mm

Figure 4-11 Temperature histories of a) 9 mm thick, b) 12 mm thick, and c) 25 mm thick steel plates

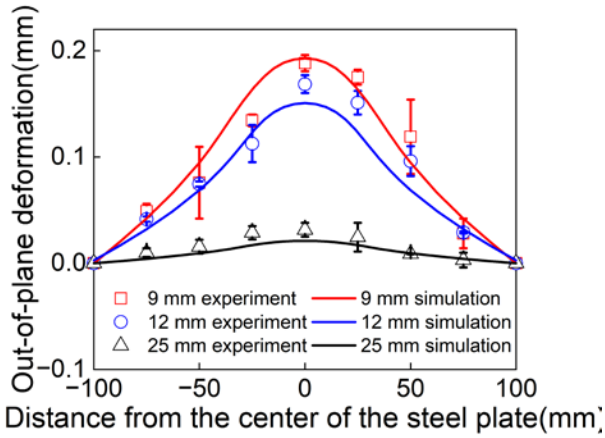

Figure 4-12 Out-of-plane deformations of the steel plates

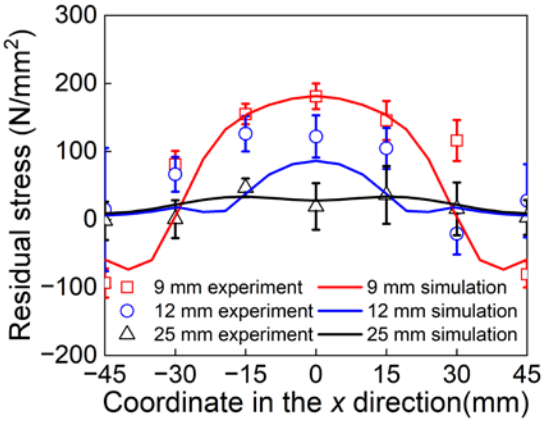

Figure 4-13 Residual stress of the steel plates

4.4 Heating correction experiment on T-joint

To further investigate the mechanism by which flame heating affects the deformation and residual stress of welded steel structures, a systematic experimental study was conducted on T-joint welded specimens. The study focuses on the characteristics of out-of-plane deformation and the evolution of residual stress in welded specimens of varying thicknesses, aiming to elucidate the role of flame heating in controlling welding-induced residual stress and deformation.

4.4.1 Specimen

The heating correction experiment was performed on T-joint specimens composed of a base plate and a rib plate.The base plate featured a square geometry, measuring 250 mm on each side, while the rib plate had a height of 80 mm. The plate thickness was 9 mm. One of the specimens used after welding in Chapter 2 was prepared. The material used for the base and rib plate was SM400A structural steel, as specified by JIS G3106. The material of the filler metal was YGW11. The details of the welding experiment have been thoroughly described in Chapter 2.

4.4.2 Experimental procedure

In the heating correction experiment, the center of the base plate was heated, as illustrated in Figure 4-14. The heating target temperature of the base plate surface was set within the range of 500–600 °C to prevent excessive microstructural changes. A propane–oxygen gas burner was used as the heating source. The flame temperature ranged from 1,500 to 1,800 °C, and the flame length was 60 mm. The heating distance between the burner port and the specimen was maintained at 30 mm, and the heating time was controlled between 7 and 8 s. After heating, the specimens underwent natural cooling to replicate real-world heating correction conditions.

To monitor the temperature histories of the specimens, symmetrical placement of thermocouples was implemented on either side of the weld toe. The thermocouples were arranged in pairs, with a 10 mm spacing between each pair, and the closest thermocouple was placed 10 mm from the weld toe (from TC1 to TC6), as illustrated in Figure 4-15. K-type thermocouples suitable for high-temperature applications were used. Figure 4-15 illustrates the specimen setup, thermocouple positions, and heating conditions. Given that

temperature measurement on the front surface was challenging due to direct flame exposure, the temperature distribution on the back surface of the specimens was used as the primary reference for analysis. The out-of-plane deformation caused by heating was measured before and after the experiment along the centerline of the specimen, as depicted in Figure 4-15.

Figure 4-14 Image of the heating experiment on the T-joint specimen

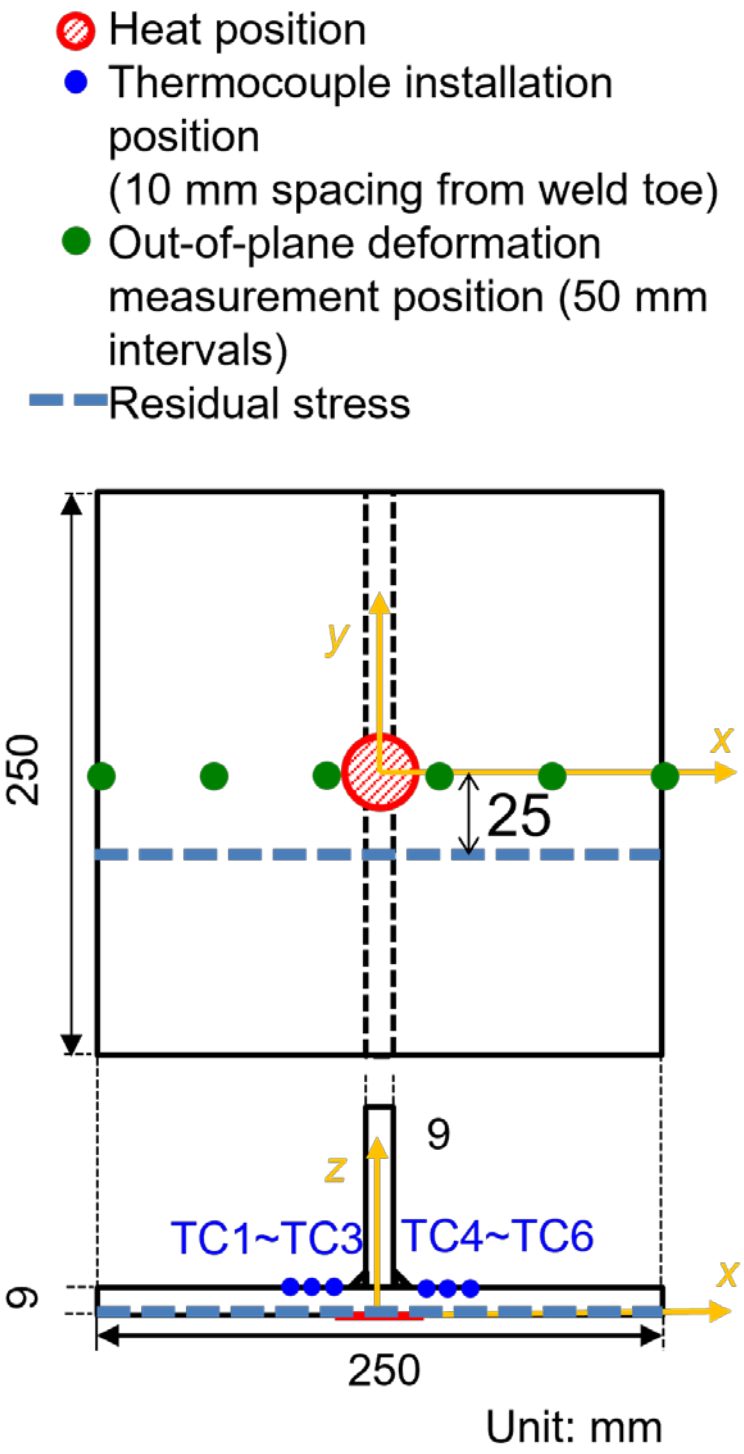

Figure 4-15 Shape and dimension of T-joint fillet-welded specimens

4.4.3 Experimental results

The temperature histories of the T-joints are shown in Figure 4-16. Given the high similarity between the results of TC1, TC2, TC3, and TC4, TC5, TC6, only the data from TC1, TC2, and TC3 are presented. The temperature measurement locations were positioned on the back surface of the steel plate. Within a few seconds after heating, heat was gradually conducted to the backside of the steel plate, causing the temperature recorded by the thermocouple to reach its maximum. The temperature histories served as a crucial reference for the heat source calibration in the numerical simulation presented in the next section.

The out-of-plane deformations of the T-joints are shown in Figure 4-17. The residual stresses in the *x* and *y* directions of the T-joints are illustrated in Figures 4-18 and 4-19, respectively. It can be observed that the heating correction process reduces the post-weld out-of-plane deformation of the specimen but increases the tensile stresses in both the *x* and *y* directions.

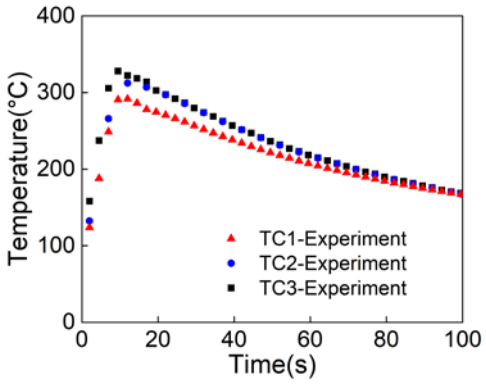

Figure 4-16 Temperature histories for the T-joint specimen

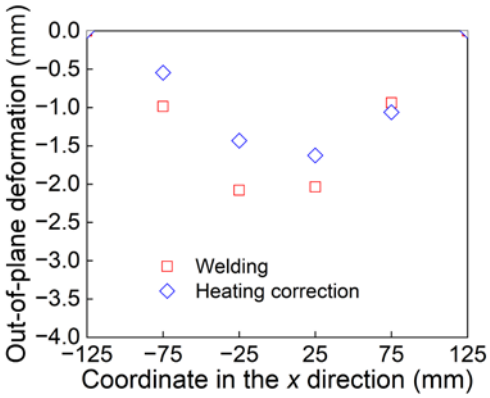

Figure 4-17 Out-of-plane deformations for the T-joint specimen

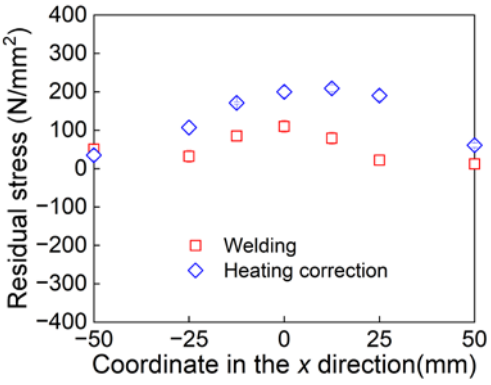

Figure 4-18 Residual stress in the *x* direction for the T-joint specimen

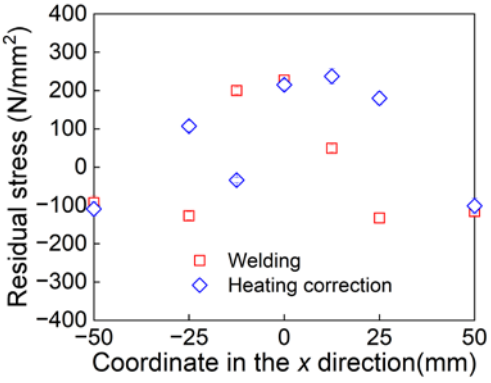

Figure 4-19 Residual stress in the *y* direction for the T-joint specimen

4.5 Finite element analysis of heating correction

4.5.1 The simulation model

The heating correction experiments performed on T-shaped fillet joint specimens were computationally reproduced via finite element modeling, utilizing the commercial ABAQUS software for this investigation. The out-of-plane deformation and residual stress induced by welding were represented by data obtained from the welding process simulations mentioned in Chapter 2. To ensure that the temperature measurement positions of the thermocouples are consistent with the nodes of the model's mesh, the model was re-meshed, and the welding process was re-simulated. The thermal dependency of material mechanical attributes and physical parameters was covered in Chapter 2. Heat dissipation from the model surfaces to the surrounding air was incorporated as the thermal boundary condition. The mechanical boundary condition involved constraining rigid body motion at the base plate corner locations, as illustrated in Figure 4-20. The displacement of the blue point was constrained in the *x*, *y*, and *z* directions. The displacement of the red point was constrained in the *y* and *z* directions. The displacement of the orange point was constrained in the *z* direction. The heating period of the models was determined through experimental observations. Remarkably, experimental measurements confirmed that the rib plate leg length was 5 mm, and the base plate leg length was 5 mm.

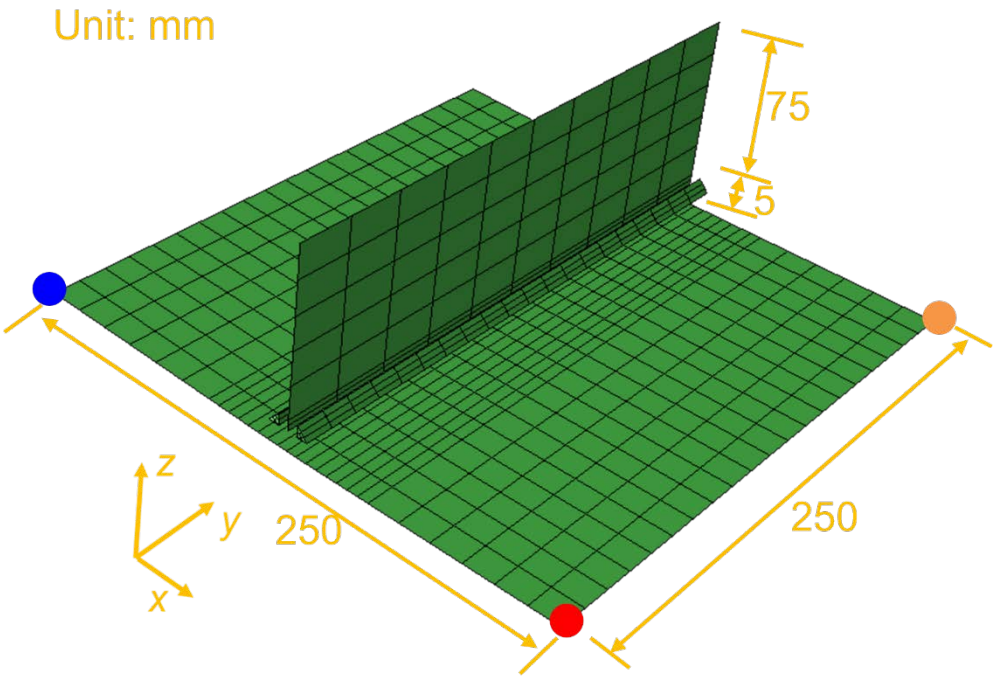

Figure 4-20 The simulation model for heating correction of the T-joint specimen

4.5.2 Simplified heat input method

In the heating correction experiments, the measured radii of the direct impingement zone r_1, the edge impingement–diffusion zone r_2, and the heat-flux diffusion zone r_3 are 12,16,74 mm, respectively. The present work determines: σ_1 is set by r_3 and calibrated so that the heat flux density decays to 20% of its maximum at r_3; σ_2 is set by r_1 and calibrated so that the heat flux density decays to 10% of its maximum at r_1, thereby reflecting the highest temperature location in the edge-diffusion region; The amplitude coefficients A_1 and A_2 are obtained by fitting to the temperature history data shown in Figure 4-16.

4.5.3 Results and discussion

After calibrating the heat input model based on the observed phenomena and results of the steel plate heating correction experiments, the simulated temperature histories (Figure 4-21) closely reproduce the experimental results. A comparison of the out-of-plane deformations from both the heating correction experiment and the simulation (Figure 4-22) reveals that the simulated magnitude of deformation recovery is slightly lower than that measured experimentally. The findings indicate that the proposed approach successfully reproduces the deformation correction behavior of the T-shaped fillet welded joint during flame heating correction. However, owing to the significantly shorter duration of the heating correction process compared to the sustained heating of steel plates mentioned in Section 4.2, the simulated correction effect on deformation is somewhat attenuated. This discrepancy likely arises because, under shorter heating periods, the fluid dynamic impact of the flame exerts a more pronounced influence on the deformation. The present study exclusively accounts for the thermal input aspects and does not incorporate the mechanical effects of flame fluid impact. Future work should therefore incorporate the fluid dynamic forces induced by the flame to enhance simulation fidelity and comprehensively capture the deformation mechanisms during flame heating straightening. The simulation results indicate in Figures 4-23 and 4-24 that the heating correction process generally increases the tensile stresses in the T-shaped fillet welded specimen along both the *x* and *y* directions. Still, the central welding zone appropriately mitigates the post-weld tensile stresses along the welding direction.

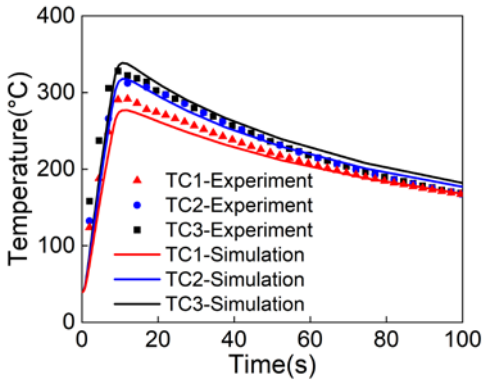

Figure 4-21 Temperature histories for the T-joint specimen

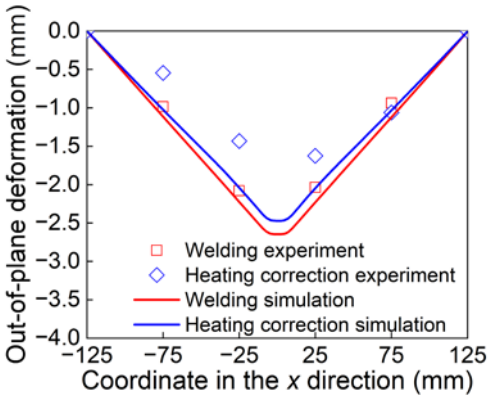

Figure 4-22 Out-of-plane deformations for the T-joint specimen

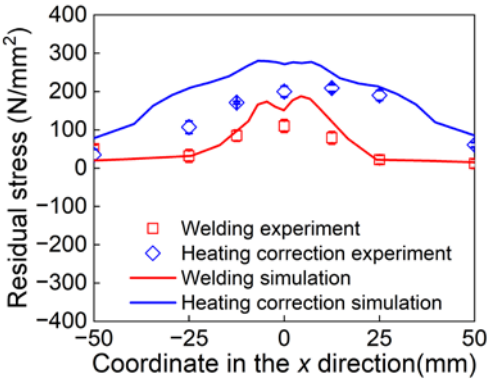

Figure 4-23 Residual stress in the *x* direction for the T-joint specimen

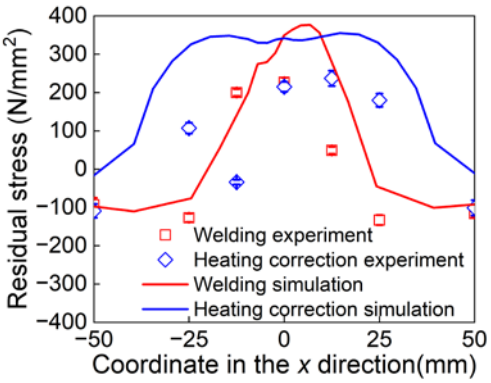

Figure 4-24 Residual stress in the *y* direction for the T-joint specimen

4.6 Parametric analysis for optimal heating correction condition

To determine the optimal heating time during the heating correction process, a parameterized analysis was performed on the heat source model introduced in Section 4.5. The heating time varied from 2.5 to 12.5 seconds, while ensuring that the steel temperature did not exceed 650 °C [4.20]. The deformation correction results are illustrated in Figure 4.25. As the heating time increases, the amount of deformation correction also increases. However, after 7.5 seconds, the rate of increase diminishes.

This behavior arises primarily from two key factors: the thermal expansion caused by heating, and more importantly, the temperature gradient between the heated surface and the back surface of the steel. When the heating time is too long, the temperature difference between the two surfaces decreases. As a result, although thermal expansion continues to occur, the additional deformation becomes less significant.

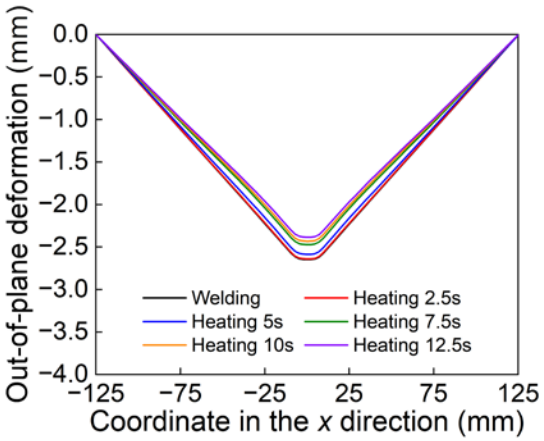

Figure 4.25 Out-of-plane in the middle

To identify the most energy-efficient heating strategy, the variation of deformation correction per unit heating time with respect to heating time was analyzed, as shown in Figure 4.26. The results indicate that a heating time of 7.5 seconds yields the highest correction efficiency per unit of energy input and thus represents the most economical heating time.

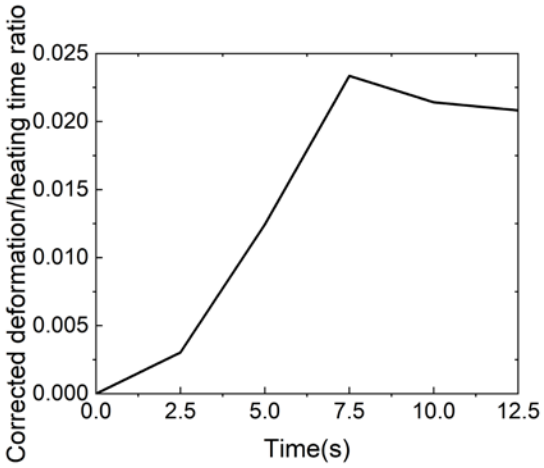

Figure 4.26 The ratio of corrected deformation to heating time

Subsequently, the model was subjected to line heating correction. The heat source moves along the *y* direction at the central position ($x = 0$) of the base plate region in the model. The heating path is shown in Figure 4.27. The heating speed was determined based on the previously obtained optimal heating time and the regions with the most significant

thermal influence—namely, the direct impingement zone and the edge impingement–diffusion zone. Specifically, the speed v was related to the boundary of the edge impingement–diffusion zone r_2 and was calculated in Equation (4.11):

$$v = \frac{2r_2}{t_{optimum}} \tag{4.11}$$

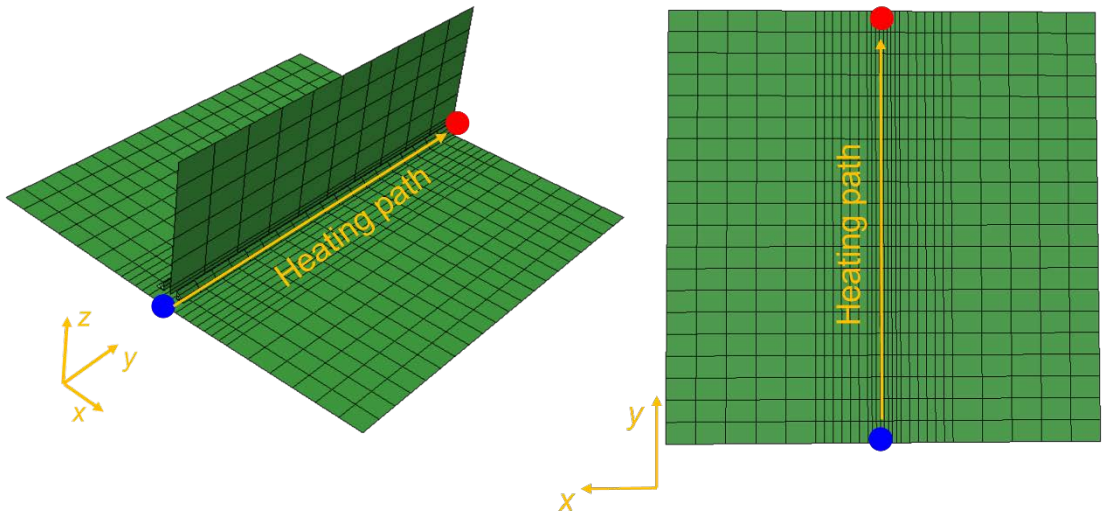

Figure 4.27 The heating path of the line heating simulation

Line heating correction was carried out at the prescribed travel speed, with the temperature maintained below 650 °C throughout the process. The intermediate deformation resulting from the line heating process is illustrated in Figure 4.28. The results demonstrate that line heating, by delivering a distributed and continuous thermal input along a defined path, induces more uniform and controlled thermal expansion and contraction over a wider area. This leads to a smoother and more effective deformation correction, especially in large-scale structural components. In contrast, spot heating involves a highly localized and concentrated heat source, which tends to raise the temperature sharply in a small region. This can result in localized thermal stress concentrations and even plastic deformation, making it more difficult to achieve

coordinated and predictable deformation across the structure.

Figures 4.29 and 4.30 show the residual stress distributions after welding, and after correction by spot heating and line heating, respectively. It is evident that in the central region of the weld, line heating is significantly more effective in reducing peak tensile residual stresses and smoothing stress gradients both in the x and y directions. This improvement is attributed to the uniform motion of the line heat source along the heating path, which facilitates gradual heat input and more homogeneous redistribution of residual stresses across the affected area. Conversely, spot heating delivers thermal energy in a highly concentrated manner, limiting its effect to a narrow zone and thus failing to address the residual stress field of the entire weld effectively.

In summary, line heating not only offers superior performance in deformation correction but also demonstrates clear advantages in residual stress management. These findings suggest that line heating holds greater potential for practical applications in the heating correction and stress relief of welded structures.

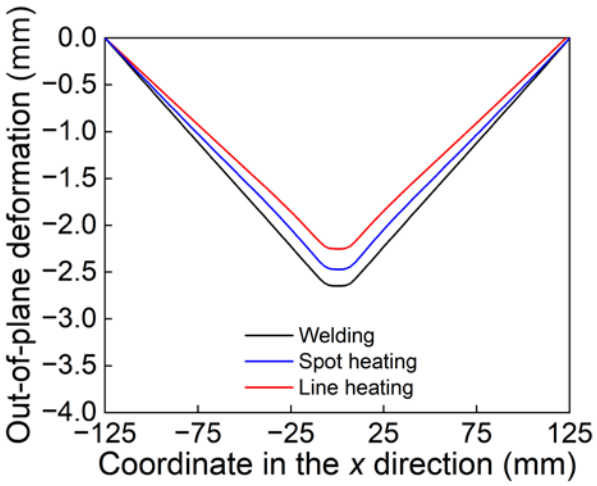

Figure 4.28 Comparison of out-of-plane deformation under different heating strategies

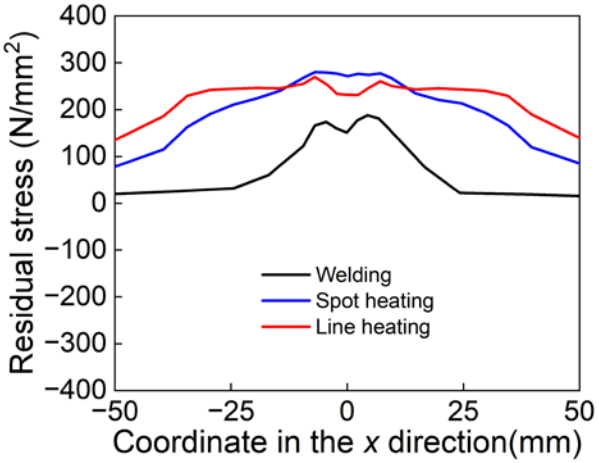

Figure 4.29 Comparison of residual stress in the *x* direction under different heating strategies

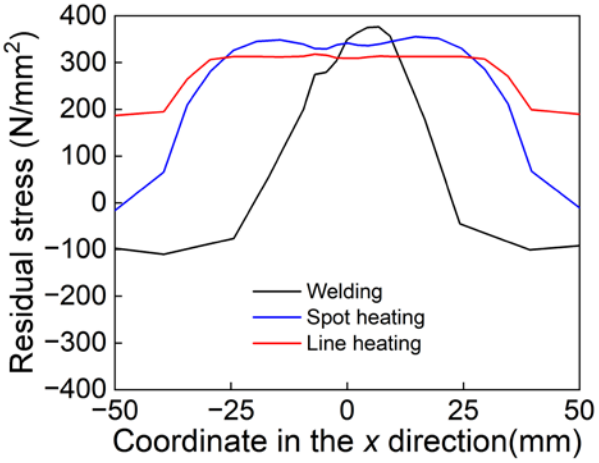

Figure 4.30 Comparison of residual stress in the *y* direction under different heating strategies

4.7 Summary

In this chapter, the flame heating phenomena of steel plates are systematically analyzed by dividing the heated region into three distinct zones, denoted as direct flame impingement zone, flame edge impingement-diffusion zone, and heat flux diffusion zone. The innermost direct flame impingement zone experiences strong convective heating from the flame jet and elevated temperatures; immediately surrounding it, the flame edge impingement–diffusion zone exhibits the highest peak temperatures due to combined jet momentum and lateral thermal spreading; and beyond that, the heat-flux diffusion zone relies chiefly on conduction and ambient convection, resulting in much gentler temperature changes.

The underlying mechanisms driving each phenomenon are elucidated in detail. Subsequently, a simplified heat input method is proposed to emulate the effects of flame heating; the parameters of this method can be calibrated directly from experimental observations and outcomes, thus offering a straightforward validation procedure. Thereafter, heating correction experiments are conducted on T-shaped specimens following single-pass fillet welding as described in Chapter 2. This heat input method is then applied to the numerical simulation of the heating correction process. The results show that the developed numerical simulation can, on the whole, reproduce the deformation correction behavior of the T-shaped fillet welded joint during flame heating correction. However, the simulated amount of deformation recovery is slightly lower than the experimentally measured value. This discrepancy likely arises because, in the actual heating–correction process, out-of-plane deformation is driven by both thermal gradients and the fluidic impulse of the flame, whereas the current simulation accounts only for the

former. Consequently, the influence of flame-induced fluid impact on out-of-plane deformation warrants further investigation.

A parametric study was conducted to determine the optimal heating time for spot heating in the correction. Heating times between 2.5 and 12.5 seconds were tested under a maximum temperature limit of 650 °C. Deformation increased with heating time, and efficiency analysis showed that a duration of 7.5 seconds provided the highest correction per unit heating time, identifying it as the most economical choice.

Using this optimal time, line heating was then applied with an equivalent heat input. Compared to spot heating, line heating produced larger and more uniform deformation correction, along with improved residual stress relief. These advantages are attributed to the continuous movement and wider thermal influence of the line heat source, which enables more effective stress redistribution across the heated region.

References

4.1 Seong, W. J., & Na, S. J. (2022). Systematization of heat straightening process of stiffened plate by surface flattening. *Journal of Materials Processing Technology*, *299*, 117333.

4.2 Kowalkowski, K., & Varma, A. H. (2007). Effects of multiple damage-heat straightening repairs on steel beams. *Transportation research record*, *2028*(1), 67-77.

4.3 Shin, J. G., & Woo, J. H. (2003). Analysis of heat transfer between the gas torch and the plate for the application of line heating. *J. Manuf. Sci. Eng.*, *125*(4), 794-800.

4.4 Ferreño, D., Carral, J. P., Calderón, R. L., Álvarez, J. A., & Gutiérrez-Solana, F. (2017). Development and experimental validation of a simplified finite element methodology to simulate the response of steel beams subjected to flame

straightening. *Construction and Building Materials, 137*, 535-547.

4.5 Gyura, L., Gáspár, M., & Balogh, A. (2021). The effect of flame straightening on the microstructure and mechanical properties of different strength steels. *Welding in the World*, *65*(3), 543-560.

4.6 Tokumaru, Y., Hirohata, M., Mukawa, S., Okada, S., & Azuma, K. (2020). Study on simulation method of heating correction in welding assembly [in Japanese]. *Proceedings of Constructional Steel, 28*, 731–738.

4.7 Tokumaru, Y., Hirohata, M., Mukawa, S., Okada, S., & Azuma, K. (2021,). A proposal of gas-heating simulation method for steel plates [in Japanese]. *Proceedings of Constructional Steel, 29*, 141–147.

4.8 Tokumaru, Y., Hirohata, M., Mukawa, S., Okada, S., & Azuma, K. (2021). An investigation on conditions for heating correction of welded I-section member. *Proceedings of the 11th International Symposium on Steel Structures.*

4.9 Japan Road Association. (2017). *Specifications for Highway Bridges (II): Steel Members Edition* [in Japanese]. Tokyo: Japan Road Association.

4.10 Zhen, H. S., Leung, C. W., & Cheung, C. S. (2012). Heat transfer characteristics of an impinging premixed annular flame jet. *Applied Thermal Engineering*, *36*, 386-392.

4.11 Hindasageri, V., Vedula, R. P., & Prabhu, S. V. (2014). Heat transfer distribution for impinging methane–air premixed flame jets. *Applied Thermal Engineering*, *73*(1), 461-473.

4.12 Viskanta, R. (1993). Heat transfer to impinging isothermal gas and flame jets. *Experimental thermal and fluid science*, *6*(2), 111-134.

4.13 Kuntikana, P., & Prabhu, S. V. (2018). Heat transfer investigations on methane-air

premixed flame jet exiting from a circular nozzle and impinging over semi-cylindrical surfaces. *International Journal of Thermal Sciences*, *128*, 105-123.

4.14 Kim, Y.-C., Lee, J.-Y., & Inose, K. (2005). The high accurate prediction of welding distortion generated by fillet welding. *Quarterly Journal of the Japan Welding Society*, *23*(3), 431–435.

4.15 Nakagawa, H., & Suzuki, H. (1999). Ultimate temperatures of steel beams subjected to fire. *Steel Construction Engineering*, *6*(22), 57–65.

4.16 Baukal Jr, C. E., & Gebhart, B. (1996). A review of empirical flame impingement heat transfer correlations. *International Journal of Heat and Fluid Flow*, *17*(4), 386-396.

4.17 Fairweather, M., Kilham, J. K., & Mohebi-Ashtiani, A. (1983). Stagnation point heat transfer from turbulent methane-air flames. *Combustion science and technology*, *35*(5-6), 225-238.

4.18 Virk, A. S. (2015). *Heat transfer characterization in jet flames impinging on flat plates* (Doctoral dissertation, Virginia Tech).

4.19 Sullivan, N., Branch, M. C., Strobel, M., Park, J., Ulsh, M., & Leys, B. (2000). The effects of an impingement surface and quenching on the structure of laminar premixed flames. *Combustion science and technology*, *158*(1), 115-134.

4.20 Wahyudi, M. T., Amri, M. S. A., Ari, M., Adam, M., Hamzah, F., & Novaldi, A. H. (2023). Analysis of quenching temperature variations in the heat straightening processFor multiple ripair FCAW welding HSLA SM490YA material. *Journal of Welding Technology*, *5*(2), 46-51.

5. Conclusions

This study systematically investigates the impact of the Continuous Distributed heat input method (the CD method) and the shell-solid element combination strategy on the simulation efficiency of T-shaped fillet joint single-layer fillet welding processes through a combination of experimental and numerical approaches. The applicability of these methods was further validated and refined in the context of three-pass butt-welding. Subsequently, to reduce out-of-plane deformations induced by welding, experimental and numerical studies on heating correction were conducted. By analyzing the thermal fluid distribution of the flame, simplified finite element models for steel plate heating and T-joint heating correction were developed to predict out-of-plane deformations and residual stresses. The chapter delineates the key findings, highlights the primary innovations, and outlines prospective directions for future work.

5.1 Key findings

(1) In Chapter 2, an efficient finite element modeling strategy was proposed to simulate the fillet welding process of T-shaped fillet joints by integrating experimental and numerical simulation methods. This strategy employs the Continuous Distributed (CD) heat input method and combines shell and solid elements to optimize the modeling process and significantly reduce computation time. Compared to the traditional Discontinuous Uniform (DU) heat input method, the CD method simulates the continuous movement of the heat source and Gaussian energy distribution, reducing model complexity and function call frequency, thereby improving computational efficiency. However, using the CD method alone did not result in substantial time savings. To further enhance computational efficiency, a hybrid modeling strategy combining shell and solid

elements was proposed, considering the assembly gaps between base plates and ribs. This shell-solid coupled simulation model accurately reproduced experimental temperature histories, out-of-plane deformations, and residual stress distributions. For 9 mm and 12 mm thick plate models, the hybrid method required only 27% and 38% of the computation time compared to solid-element models, respectively, achieving significant computational efficiency gains while maintaining modeling accuracy.

(2) In Chapter 3, an integrated methodology combining experimental validation and finite element simulations was implemented to develop and assess an optimized FEM framework for the three-pass butt-welding process. The study demonstrated that the hybrid modeling strategy combining solid and shell elements introduced in Chapter 2 is applicable not only to single-layer fillet welds but also to multi-pass butt-welding configurations. Comparative analyses of thermal cycles, deformation patterns, and residual stress distributions confirmed the broad applicability of this modeling approach across different welding scenarios. Furthermore, substituting the traditional Discontinuous Uniform (DU) heat input method with the Continuous Distributed (CD) heat input method reduced simulation runtimes by more than 50% (from 57 minutes 34 seconds to 26 minutes 30 seconds) while maintaining predictive accuracy, highlighting the critical impact of heat source model selection on computational performance. Therefore, selecting or tailoring an appropriate heat input scheme is essential for achieving high-fidelity results with efficient use of computational resources.

(3) In Chapter 4, the flame heating phenomena of steel plates were systematically analyzed by dividing the heated region into three distinct zones: the direct flame impingement zone, the flame edge impingement-diffusion zone, and the heat flux diffusion zone. The innermost direct flame impingement zone experiences strong

convective heating from the flame jet, leading to rapid temperature increases. Surrounding this is the flame edge impingement-diffusion zone, where combined jet momentum and lateral thermal spreading result in the highest peak temperatures. Beyond that, the heat flux diffusion zone relies primarily on conduction and ambient convection, causing more gradual temperature changes. Based on a detailed understanding of these phenomena, a simplified heat input method was proposed to emulate the effects of flame heating. The parameters of this method can be directly calibrated from experimental observations, simplifying the validation process. Subsequently, heating correction experiments were conducted on a T-shaped fillet welded joint following single-layer fillet welding as described in Chapter 2, and the proposed heat input method was applied to the numerical simulation of the heating correction process. The results demonstrate that the proposed method effectively reproduces the flame-induced corrective behavior of the T-shaped components. A parametric study was conducted to determine the optimal heating time for spot heating in the correction. Heating times between 2.5 and 12.5 seconds were tested under a maximum temperature limit of 650 °C. Deformation increased with heating time, and efficiency analysis showed that a duration of 7.5 seconds provided the highest correction per unit heating time, identifying it as the most economical choice.

5.2 Innovations and engineering significance

(1) This study proposed and optimized the Continuous Distributed (CD) heat input method, compared to the traditional Discontinuous Uniform (DU) method, the CD method significantly reduces model complexity and function call frequency, enhancing computational efficiency. By introducing the shell-solid hybrid modeling strategy, the computational efficiency of finite element simulations for welding processes is

significantly improved, reducing the consumption of computational resources and making it suitable for simulating large-scale structures. The CD heat input method and shell-solid hybrid modeling strategy balance accuracy with efficiency, equipping engineers with a reproducible approach for deploying high-fidelity welding simulations in commercial finite-element environments.

(2) The proposed modeling methods demonstrate good applicability and accuracy in different welding scenarios, accurately predicting temperature distributions, deformation patterns, and residual stress distributions during welding processes, meeting practical engineering requirements. The shell-solid coupling framework offers a scalable and efficient numerical platform for diverse welding applications.

(3) For flame heating correction processes, a simplified heat input model was proposed. Parameters of this model can be directly calibrated from experimental data, simplifying validation. This approach provides an efficient modeling method for numerical simulation of welding deformation control, contributing to the efficiency and automation of heating correction work. Using this optimal heating time, line heating was applied with equivalent heat input. Compared to spot heating, line heating produced larger and more uniform deformation correction, along with improved residual stress relief. These advantages stem from the continuous movement and wider thermal influence of the line heat source, enabling more effective stress redistribution across the heated region.

5.3 Limitations and future work

(1) While the present study concentrates on carbon-steel and straight-bead welds, future work should encompass stainless steels, aluminum alloys, and complex geometries to validate broader material and process applicability.

(2) The current finite element model for welding processes primarily focuses on the macroscopic distribution trends of residual stresses, achieving accurate predictions, particularly in the base metal regions. However, the study of residual stresses within the weld itself remains insufficient. To enhance the precision in predicting residual stress, future research should integrate microstructural evolution models with macroscopic thermo-mechanical simulations, establishing a multi-scale coupled analysis framework. Investigating adaptive mesh refinement and machine-learning-driven automation could pave the way for efficient parameter optimization and real-time process control in welding simulations.

(3) The current heating correction finite element model exhibits lower accuracy in predicting out-of-plane deformation compared to the heating models. This discrepancy may be attributed to the significantly shorter heating time in heat correction experiments relative to standard heating experiments, resulting in a more pronounced impact of flame fluid dynamics on material deformation—a factor not adequately accounted for in existing models. Consequently, future research should aim to incorporate the effects of flame fluid dynamics into finite element models to enhance the accuracy of out-of-plane deformation predictions.

Acknowledgment

First and foremost, I would like to express my deepest gratitude to my supervisor, Associate Professor Hirohata. When I first contemplated pursuing my studies in Japan, I was uncertain about the path ahead and the kind of researcher I aspired to become. Throughout the past three years, his unwavering guidance and support have been instrumental in shaping my academic journey. His rigorous approach to research and meticulous attention to detail set a standard that I continually strive to meet. Beyond academic mentorship, his humility and dedication to nurturing students have profoundly influenced me. I vividly recall numerous occasions when he patiently reviewed my work, providing constructive feedback that challenged me to think critically and strive for excellence. Under his influence, I have come to understand the kind of researcher I should strive to be, and I am sincerely grateful for his mentorship.

I am also sincerely grateful to Professor Ma, Professor Kamada, and Professor Inui for taking the time to review my thesis and provide invaluable feedback, which significantly enhanced the quality of my work.

My heartfelt thanks go to all the members in our lab, whose support and companionship have made these three years both meaningful and enjoyable. When I first arrived in Japan, I received warm support from many members. I am especially thankful to Mr. Hashiguchi and Mr. Murabayashi. Their enthusiasm and kindness helped me quickly adapt to the new environment. I still cherish our conversations about the cultural differences between our countries, which were both enlightening and enjoyable, leaving a lasting impression on me.

I would also like to express my sincere appreciation to Mr. Chen. He patiently guided me through unfamiliar procedures and even took me to explore many places in Japan, which

made the transition much smoother and more pleasant.

Over the past three years, I was fortunate to have the companionship of Mr. Tang, Mr. Mao, and Ms. Cheng. Whether in our studies or during our leisure time together, they were always supportive and encouraging. The memories we shared, working, playing, and laughing together, are ones I will always treasure. I am also grateful to Mr. Martin and Mr. Inoue, whose cheerful and open personalities brought joy and energy to our lab.

I am deeply grateful to Assistant Professor Jiang, who was the very first to offer me extensive help, not only in my research but also in my daily life. He gave me a great sense of reassurance throughout my time in Japan. His thoughtful advice and warm encouragement were an important part of my experience abroad and have left a lasting impression on me.

Finally, I wish to thank my family, my partner, and my close friends. Their unconditional love, patience, and support have been my greatest source of strength. Even from afar, they encouraged me through every challenge, believed in me when I doubted myself, and celebrated every small achievement along the way. This accomplishment is not mine alone. It belongs equally to all those who stood beside me with unwavering faith and understanding.

May 2025

GUAN XIAOYU

List of publications

Journal publications

[1] **Guan, X.**, & Hirohata, M. (2024). Effective FE simulation methods for fillet welding process by continuous distributed heat input and element combination. *Finite Elements in Analysis and Design*, *236*, 104181. https://doi.org/10.1016/j.finel.2024.104181

[2] **Guan, X.**, Tokumaru, Y., Hirohata, M., Mukawa, S., & Okada, S. (2024). A Proposal of a Heat Input Model, for Heating Correction, on Welded Steel Structural Members. *Acta Polytechnica Hungarica*, *21*(5), pp.35-52. https://doi.org/10.12700/APH.21.5.2024.5.4

[3] **Guan, X.**, Hirohata, M., & Chang, K. H. (2025). A streamlined FE method for deformation and residual stress prediction in butt welding using continuous heat input. *Welding in the World*, 1-11. https://doi.org/10.1007/s40194-025-01971-1

Conferences

[1] **Guan, X.**, & Hirohata, M. (2023). Influence of heat input method and element combination on effectiveness of FE simulation for fillet welded joints. *Preprints of the National Meeting of JWS*, Vol. 2023f, pp. 260–261.

[2] **Guan, X.**, & Hirohata, M. (2023). A proposal of heat input method and element combination for effective simulation of fillet welding process. *Proceedings of the Welded Structure Symposium 2023*, pp. 500-503.

[3] **Guan, X.**, & Hirohata, M. (2023). A simulation model for heating correction on I-shaped welded steel bridge members. *Proceedings of the 13th German-Japanese*

Bridge Symposium, pp. 517-522.

[4] **Guan, X.**, & Hirohata, M. (2024). An effective FE simulation method for butt-welding process by continuous distributed heat input. *Preprints of the National Meeting of JWS*, Vol. 2024f, pp. 248–249.